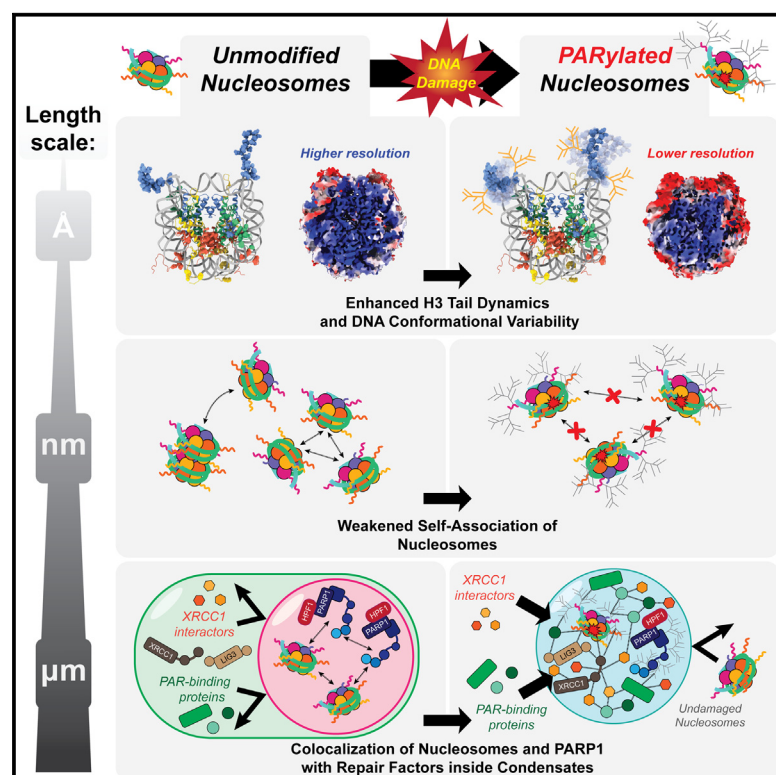


Poly(ADP-ribosyl)ation enhances nucleosome dynamics and organizes DNA damage repair components within biomolecular condensates

Graphical abstract



Authors

Michael L. Nosella, Tae Hun Kim, Shuya Kate Huang, ..., Hyun O. Lee, Julie D. Forman-Kay, Lewis E. Kay

Correspondence

forman@sickkids.ca (J.D.F.-K.), lewiskay@utoronto.ca (L.E.K.)

In brief

Nosella et al. establish that poly(ADP-ribosyl)ation of nucleosomes dramatically increases histone H3 tail dynamics and DNA conformational variability while leaving the core structure intact. These changes correlated with enhanced ligation of nucleosome single-strand nicks, disruption of nucleosome oligomers, and colocalization of nucleosomes with DNA repair factors inside biomolecular condensates.

Highlights

- Nucleosome PARylation enhances H3 tail dynamics without perturbing the histone core
- PARylation dramatically enhances ligation of single-strand nicks in nucleosomes
- Stacking and self-association of mononucleosomes is inhibited by PARylation
- PARylation reorganizes condensates containing nucleosomes and DNA repair factors

Article

Poly(ADP-ribosyl)ation enhances nucleosome dynamics and organizes DNA damage repair components within biomolecular condensates

Michael L. Nosella,^{1,2,7} Tae Hun Kim,^{1,2,3,4,7,8} Shuya Kate Huang,^{1,2,3,4} Robert W. Harkness,^{1,2,3,4} Monica Goncalves,⁵ Alisia Pan,¹ Maria Tereshchenko,² Siavash Vahidi,⁵ John L. Rubinstein,^{1,2,6} Hyun O. Lee,² Julie D. Forman-Kay,^{1,2,*} and Lewis E. Kay^{1,2,3,4,9,*}

¹Molecular Medicine Program, The Hospital for Sick Children, Toronto, ON M5G 0A4, Canada

²Department of Biochemistry, University of Toronto, Toronto, ON M5S 1A8, Canada

³Department of Molecular Genetics, University of Toronto, Toronto, ON M5S 1A8, Canada

⁴Department of Chemistry, University of Toronto, Toronto, ON M5S 1A8, Canada

⁵Department of Molecular and Cellular Biology, University of Guelph, Guelph, ON N1G 2W1, Canada

⁶Department of Medical Biophysics, University of Toronto, Toronto, ON M5S 1A8, Canada

⁷These authors contributed equally

⁸Present address: Department of Biochemistry, School of Medicine, Case Western Reserve University, Cleveland, OH 44106, USA

⁹Lead contact

*Correspondence: forman@sickkids.ca (J.D.F.-K.), lewiskay@utoronto.ca (L.E.K.)

<https://doi.org/10.1016/j.molcel.2023.12.019>

SUMMARY

Nucleosomes, the basic structural units of chromatin, hinder recruitment and activity of various DNA repair proteins, necessitating modifications that enhance DNA accessibility. Poly(ADP-ribosyl)ation (PARylation) of proteins near damage sites is an essential initiation step in several DNA-repair pathways; however, its effects on nucleosome structural dynamics and organization are unclear. Using NMR, cryoelectron microscopy (cryo-EM), and biochemical assays, we show that PARylation enhances motions of the histone H3 tail and DNA, leaving the configuration of the core intact while also stimulating nuclease digestion and ligation of nicked nucleosomal DNA by LIG3. PARylation disrupted interactions between nucleosomes, preventing self-association. Addition of LIG3 and XRCC1 to PARylated nucleosomes generated condensates that selectively partition DNA repair-associated proteins in a PAR- and phosphorylation-dependent manner *in vitro*. Our results establish that PARylation influences nucleosomes across different length scales, extending from the atom-level motions of histone tails to the mesoscale formation of condensates with selective compositions.

INTRODUCTION

Eukaryotic cellular processes involving DNA are controlled by chromatin structure, preventing accessibility of various protein factors in the absence of structural rearrangement. At its most fundamental level, chromatin is organized into nucleosomes comprising a histone protein octamer encircled by ~ 1.6 turns of double-stranded DNA. The nucleosome structure is stabilized by extensive contacts between DNA and the four core histones, H2A, H2B, H3, and H4, of which there are two copies each per octamer.^{1,2} High-resolution crystallographic and cryoelectron microscopy (cryo-EM) structures have provided a wealth of information on the canonical nucleosome structure and many of its variants, including those containing histone isoforms and binding proteins.^{3,4} However, these static structures do not capture the intrinsic dynamics of the nucleosome.^{1,5–7} For example, nucleosomal DNA undergoes spontaneous partial unwrapping and rewinding (i.e., “breathing” motions) even in the absence

of energy-expending factors.⁸ Recent studies have shown that mutations and post-translational modifications (PTMs) can induce conformational fluctuations within the histone core on the microsecond (μ s)–millisecond (ms) time scale, highlighting that even the most ordered segments of the nucleosome can exhibit structural plasticity.^{9–12} Outside of the core, histones possess intrinsically disordered “tails” that are almost always invisible in crystal and cryo-EM density maps due to their conformational heterogeneity and rapid motions, although they are crucial regulators of nucleosome stability,^{13–18} chromatin compaction,^{19–22} chromatin phase separation,^{23–25} and recruitment of DNA-binding factors.²⁶ Furthermore, the tails serve as the primary sites of PTMs or “epigenetic” modifications, which significantly influence nucleosome function and dynamics.^{27,28}

Chromatin is vulnerable to genotoxic agents that damage the chemical structure of DNA. Various pathways exist to remediate sites of DNA damage, which, if left unrepaired, can induce genomic instability. Single-strand breaks (SSBs)—one

of the most common types of DNA damage²⁹—are detected by poly(ADP-ribose) (PAR) polymerases (PARPs), principally PARP1.^{30–32} Upon binding to SSBs, PARP1 rapidly modifies itself and proteins in its vicinity with PAR, an anionic, nucleic acid-like biopolymer that is highly branched and lengthy (potentially spanning up to hundreds of units, although likely shorter *in vivo*).^{33,34} Histones H2B and H3 are notable targets of poly(ADP-ribose)ylation (PARylation) along with many other factors.^{35,36} Damage-induced PARylation facilitates DNA repair by recruiting SSB repair (SSBR) factors to DNA lesions,³⁷ although some proteins' activities are directly enhanced by their interactions with PAR, suggesting that PAR has additional functionality beyond recruitment.^{38,39} In many cases, the mechanisms linking PARylation with the upregulation of DNA repair reactions are unclear.

PARP1 and PARylation affect the superstructural organization of chromatin. Seminal electron microscopy studies found that PARylation diminishes chromatin compaction by disrupting the characteristic “zigzag” arrangement of polynucleosomal arrays.⁴⁰ Later investigation by Strickfaden et al. found that micro-irradiation-induced DNA damage causes local and reversible PARylation-dependent chromatin expansion in human cell nuclei.⁴¹ In *Drosophila* salivary gland polytene chromosomes, PARylation decondenses chromatin surrounding genomic loci undergoing high levels of transcription during heat shock, suggesting that PAR-dependent regulation of chromatin structure modulates transcriptional activity.⁴² PARP1 itself binds to nucleosomes and occupies transcriptionally repressed chromatin domains.^{43–45} More recently, it was shown that PARylation is involved in forming biomolecular condensates at DNA damage sites.^{46–49} Biomolecular condensates are increasingly appreciated for their ability to regulate various aspects of biological function, including enzymatic reaction kinetics and the subcellular localization of biomolecules.^{50–52} In the context of DNA repair, condensation has been implicated in the subnuclear organization of important DNA repair factors such as 53BP1, MRNIP, and Rad52 at damage sites.^{53–56} Whether PARylation can impart similar regulatory effects on DNA repair via condensate formation is only beginning to be explored.⁵⁷

These and other examples^{58–62} highlight how PARylation regulates chromatin organization on a broad scale. However, it is less clear how PARylation impacts the structure of individual nucleosomes. PARylation may destabilize histone-DNA interactions, compromising the integrity of the nucleosome and causing it to disassemble.⁶³ Alternatively, PARylation may induce subtler changes, such as increasing DNA unwrapping rates to enhance DNA accessibility while leaving the overall structure of the nucleosome intact. Another possibility is that PAR has no direct impact on nucleosome structure or dynamics and instead acts solely as a recruitment signal for other chromatin remodeling factors, such as ALC1.⁶⁴ Obtaining detailed structural evidence to support or reject any of these potentially overlapping scenarios has been hindered by the inherent size and structural heterogeneity of PAR, which complicates its analysis by most structural determination techniques.

In this study, we investigated the structural and functional outcomes of PARylating nucleosome core particles (NCPs) using a combination of biochemical assays, microscopy, and biophys-

ical tools. Our data illustrate that PARylation has multiple impacts on nucleosome structural dynamics and organization across different length scales—at the atomic scale of histone tail backbone and DNA fluctuations, at an intermediate scale of nucleosome-nucleosome interactions, and the “mesoscale” of biomolecular condensates formed by PARylated nucleosomes and select DNA repair-related proteins.

RESULTS

Preparation of a PARylated nucleosome core particle containing nicked DNA

Histone octamers consisting of the four canonical histones (H2A, H2B, H3, and H4 from *Drosophila melanogaster*) were wrapped with the 153 bp Widom “601”-DNA sequence⁶⁵ to produce NCPs lacking linker DNA. We used PARP1—the most prevalent PARP active during DNA damage repair in human cells^{66,67}—to enzymatically modify these NCPs with PAR. PARP1 activity is stimulated by binding of its N-terminal zinc-binding domains to a variety of DNA structures containing exposed termini, including the blunt ends of 601-DNA.^{68,69} To better mimic the activation that occurs during SSB recognition and repair, we introduced a single-strand nick 31 nucleotides (nt) away from the 3' end of the 601-DNA using the nicking endonuclease Nt.BsmAI⁷⁰ (Figure S1A). Treating 601-DNA with Nt.BsmAI resulted in nicked 601-DNA (n601), which resolves as three fragments on a denaturing polyacrylamide gel (Figure S1B) and one species on a native gel (Figure S1C). The 5' end of the resulting 31 nt fragment was left phosphorylated at the nick site to facilitate LIG3 activity in subsequent ligation assays (see below), whereas the terminal blunt ends were dephosphorylated with alkaline phosphatase to prevent ligation of DNA molecules across separate nucleosomes (Figure S1D). We refer to n601-containing NCPs as nNCPs. For certain experiments, an Alexa Fluor 647 (AF647) dye was covalently adjoined to the 3' end of the 31 nt fragment to allow specific detection of this segment in electrophoretic gel-based assays. AF647-labeled nNCPs migrated as a single species on a native polyacrylamide gel, suggesting that these modifications did not compromise the structural integrity or homogeneity of the nNCP (Figure S1E). In some cases, nNCPs were reconstituted with a histone H3 (Q125C) mutant labeled with Alexa Fluor 488 (AF488) to enable fluorescence-based detection of H3 following sodium dodecyl sulfate-polyacrylamide gel electrophoresis (SDS-PAGE).

We PARylated AF488-H3-containing nNCPs with recombinant, mCherry-tagged PARP1 (mChPARP1) and the adaptor protein histone PARylation factor 1 (HPF1), which is necessary for histone PARylation.^{35,71} After incubating nNCPs with mChPARP1, HPF1, and nicotinamide adenine dinucleotide (NAD⁺), the substrate for PARylation, we detected a shift in the mobility of AF488-labeled histone H3 (Q125C) by SDS-PAGE (Figure S1F). PARylation caused AF488-H3 to migrate as a smear, consistent with the attachment of PAR chains of variable length.⁷² This shift only occurred in the presence of HPF1 (Figure S1F). A similar shift was observed for mChPARP1, which is known to modify itself without requiring HPF1, although inclusion of HPF1 did change the smearing pattern exhibited by automodified mChPARP1, perhaps because it modulates chain length

and site specificity of PARylation on PARP1.^{35,73} The electrophoretic mobilities of histones H2A, H2B, and H4 were unchanged in the presence of mChPARP1, HPF1, and NAD⁺, demonstrating that they were not PARylated under the same conditions (Figure S1G).

Histone PARylation enhances the ligation of nucleosome-associated nicked DNA

Ligation reactions are a key step in several DNA-repair pathways, including in SSBR.⁷⁴ All human DNA ligases possess an evolutionarily conserved, tripartite catalytic domain that must encircle DNA to catalyze adenylation of phosphorylated 5' ends preceding ligation.⁷⁵ Histone-DNA contacts obstruct the accessibility of nucleosomal DNA to ligases, causing single-strand nicks near the structurally ordered histone core to be ligated more slowly than those in the relatively exposed linker DNA, or in “free” DNA unassociated with nucleosomes.^{76,77} Given its prominent role in DNA-repair pathways, we asked whether PARylation might stimulate ligation of single-strand nicks in nucleosomes by disrupting histone tail-DNA interactions and increasing DNA accessibility.

We performed ligation assays on nNCPs using the SSBR-relevant DNA ligase complex comprising XRCC1 and LIG3 (Figure 1A). Although XRCC1 lacks catalytic activity, it is thought to be a constitutive binding partner of LIG3 *in vivo* with some evidence suggesting that it modulates ligase activity.^{76,78} In the presence of magnesium adenosine 5'-triphosphate (MgATP), the XRCC1/LIG3 complex (hereafter termed XRCC1/LIG3) ligates n601-DNA (unassociated with histones, i.e., free DNA) very rapidly, with almost complete conversion of the AF647-labeled 31 nt segment into the 153 nt product (Figure S2A). When the same DNA was incorporated into nNCPs under identical reaction conditions, the amount of ligation was significantly diminished (Figure S2A), consistent with previous reports,⁷⁶ and could only be observed at very high LIG3 concentrations (2 μ M). Although it has been found that some ligases can overcome steric barriers presented by nucleosomes to catalyze ligation, either by disrupting nucleosome structure or capitalizing on intrinsic unwrapping events,^{76,77,79} we observed that XRCC1/LIG3-mediated ligation rates were strongly inhibited in nNCPs.

Next, we introduced mChPARP1/HPF1 and NAD⁺ to PARylate the nNCPs immediately prior to addition of XRCC1/LIG3 (Figure 1A). Under these conditions, the amount of ligated product increased drastically compared with similar samples in which NAD⁺ was excluded (Figures 1B–1E). In the absence of NAD⁺, varying the mChPARP1/HPF1 concentration did not affect nNCP ligation (Figure S2B). Adding NAD⁺ to nNCP samples lacking mChPARP1/HPF1 also had no effect on ligation (Figure S2C). Ligation of free n601-DNA was not accelerated by PARylation (Figures S2D–S2G); in fact, the presence of automodified mChPARP1 slightly hampered ligation of free DNA under these conditions. This suggests that PARylation-dependent increases in ligation are specific to the NCP and not a result of PAR chains directly enhancing ligase activity. When PARylation is initiated in nNCP samples excluding HPF1, modification occurs on mChPARP1 but not on histones (Figure S1F); in this scenario, the amount of ligation was intermediate between the unPARylated and histone-PARylated conditions (Figures 1B and 1E).

These results suggest that although direct PARylation of nNCPs causes the greatest acceleration in ligation, merely being in proximity to PAR chains is sufficient to induce structural and/or dynamical changes in the nNCP that accelerate ligation.

Next, we assessed whether nNCP ligation correlates with PAR chain length. PAR glycohydrolase (PARG) rapidly degrades PAR, leaving only a single ADP-ribosyl moiety attached to the modified serine.⁸⁰ We titrated PARG into PARylated nNCP ligation reactions to partially hydrolyze PAR prior to the addition of XRCC1/LIG3. Ligation diminished as the PARG concentration increased, becoming almost undetectable at the highest tested PARG concentration, 100 nM (Figures 1F and 1H). The electrophoretic mobilities of PARylated mChPARP1 and H3 tended more toward their unmodified positions as the PARG concentration increased, suggesting that PAR chains became shorter on average (Figure 1G). Thus, the extent of nNCP ligation is proportional to PAR chain length, with longer PAR chains yielding higher amounts of ligation. Furthermore, these data suggest that PARylation reversibly enhances ligation, as removing PAR returns the nNCP to its initial ligation-resistant state.

Nuclease digestion assays have previously been used to probe DNA accessibility in nucleosomes.^{81,82} Thus, we measured how rapidly and extensively nNCP DNA is degraded by micrococcal nuclease (MNase), a non-specific double-stranded DNA endo- and exonuclease, in relation to PARylation status. DNA cleavage occurred more rapidly in samples containing PARylated nNCPs versus those containing unmodified nNCPs (Figure 1I). These results, which are consistent with previous reports,⁸¹ demonstrate that PARylation increases the accessibility of nucleosomal DNA to MNase digestion under the prescribed reaction conditions, correlating with the enhancements seen in the ligation assays.

PARylation increases H3 tail dynamics and induces site-specific chemical shift perturbations across all histone tails

The dramatic increase in ligation rates associated with PARylation could result from alterations to nucleosome structure and/or dynamics, particularly in the histone tails, which form extensive DNA contacts while exhibiting a high degree of conformational flexibility.⁸³ Thus, we performed NMR experiments to probe how PARylation impacts the dynamics of the histone tails at atomic resolution. We prepared nNCP samples in which each histone was isotopically labeled, in turn, with ²H and ¹⁵N, whereas the rest were enriched only in ²H. Using this labeling scheme, only resonances corresponding to amide groups in the highly flexible tail(s) of the ¹⁵N-labeled histone are visible in ¹H-¹⁵N-based heteronuclear single quantum coherence (HSQC) experiments. Perdeuteration mitigates signal losses resulting from ¹H-¹H relaxation mechanisms, especially for tail amide groups that are close to the histone core. We compared nNCPs with each discrete histone-labeling pattern in the unmodified and PARylated states. PARylated nNCPs were semi-purified away from PARylated mChPARP1, although a significant fraction of the latter remained in NMR samples (Figures S1J and S1K). As PARylation is known to disrupt the interaction between PARP1 and DNA,⁸⁴ the contaminating automodified

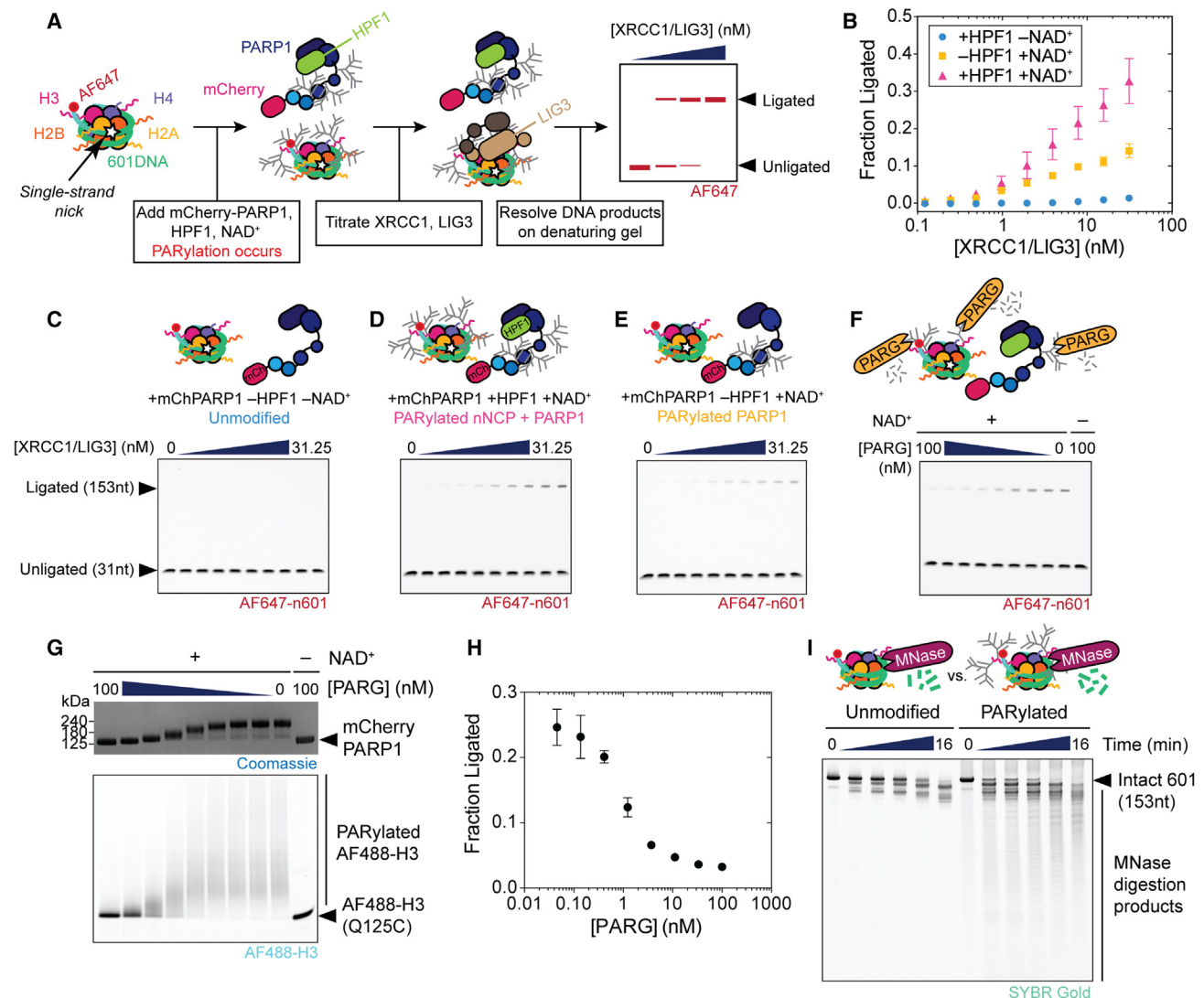


Figure 1. Poly(ADP-ribosylation) enhances ligation of single-strand nicks in nucleosomal DNA

(A) Schematic overview of ligation assays. NCPs containing 601-DNA with a single-strand nick and a 3'-AF647 dye are incubated with combinations of mCh- PARP1 ($1 \mu\text{M}$), HPF1 ($1.5 \mu\text{M}$), and NAD^+ (1 mM). Following PARylation (20 min, 37°C), XRCC1 and LIG3 (XRCC1/LIG3) are titrated into the reaction mixture, which is incubated another 20 min at 37°C . DNA products are resolved by denaturing PAGE.

(B) Plot of ligation assay results in (C)–(E). Error bars represent standard deviation, $n = 3$.

(C–E) Denaturing PAGE analysis of ligation assays (C) in which NAD^+ is excluded and PARylation does not occur on either the nNCP or mCh- PARP1 , or (D) where PARylation of nNCPs and mCh- PARP1 is induced by addition of HPF1 and NAD^+ , or (E) where PARylation of mCh- PARP1 but not the nNCP is initiated by addition of NAD^+ without HPF1.

(F) PARG is titrated into ligation assays during PARylation and before incubation with XRCC1/LIG3 (15 nM across all PARG titration points). Products are resolved by denaturing PAGE.

(G) SDS-PAGE analysis of reactions in (F), detecting Alexa Fluor 488 (AF488) fluorescence signal (bottom) or Coomassie staining (top) to assess PARylation of AF488-H3-labeled nNCPs or mCh- PARP1 , respectively.

(H) Plot of ligation assay results shown in (F). Error bars represent standard deviation, $n = 3$.

(I) Denaturing PAGE analysis of MNase sensitivity assays conducted on either unmodified or PARylated nNCPs. Time-dependent accumulation of MNase digestion products was detected by SYBR Gold staining.

See also Figures S1, S2, and S4.

mCh- PARP1 is not expected to influence the results of the NMR study. Indeed, we confirmed that autoPARylation decreases the affinity of mCh- PARP1 to interact with the nNCP in an electrophoretic mobility shift assay (Figures S1H and S1I).

The H3 N-terminal tail exhibited the greatest chemical shift perturbations (CSPs) following PARylation (Figure 2A). CSPs from PARylation were observed for almost every residue across this tail, with local maxima at the reported sites of modification

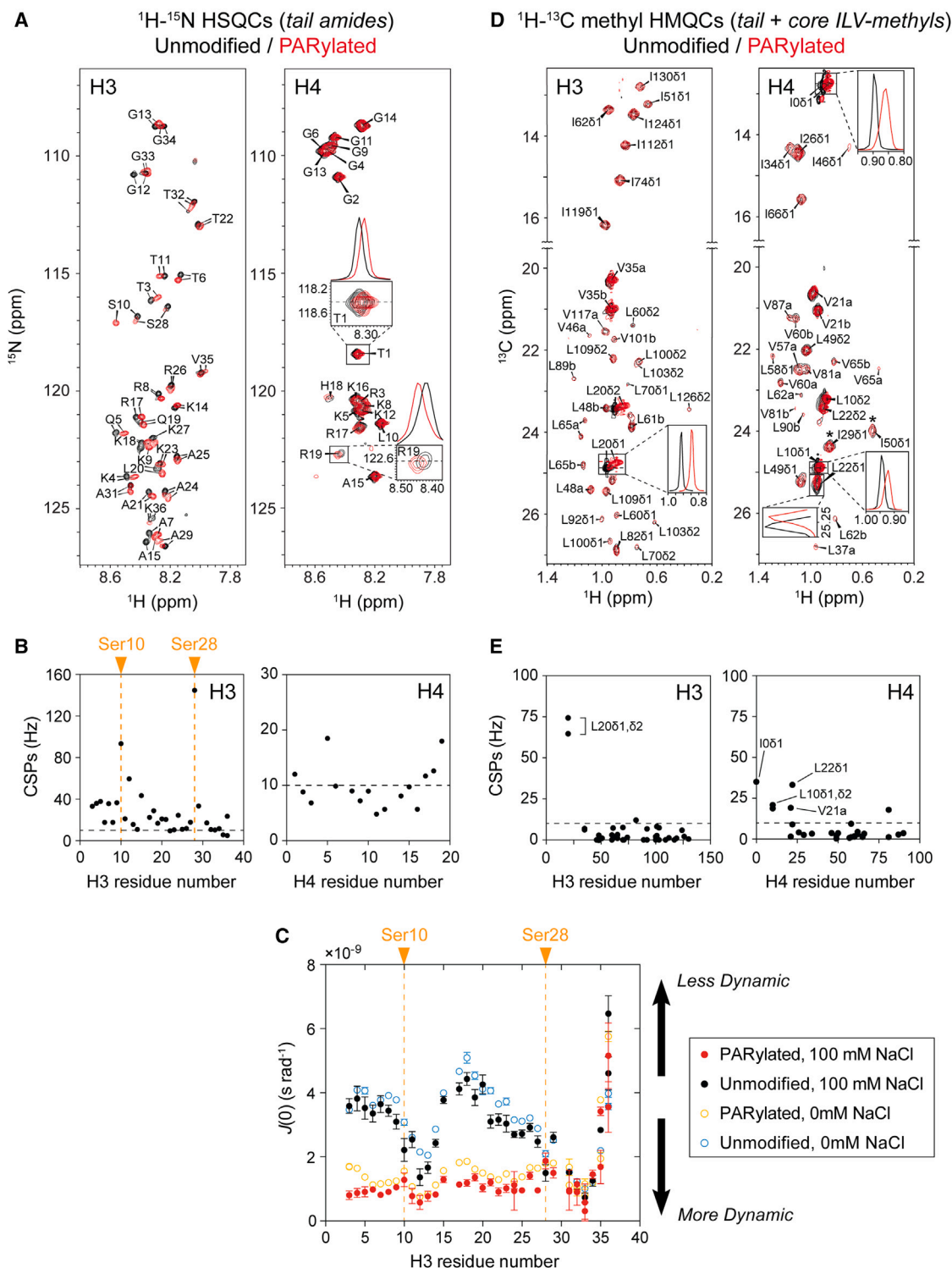


Figure 2. Poly(ADP-ribosylation) induces chemical shift perturbations in histone tail resonances and enhances H3 N-terminal tail dynamics
(A) Overlay ^1H - ^{15}N HSQC spectra of histone H3 and H4, with (red) and without (black) PARylation, in 20 mM sodium phosphate, 100 mM NaCl, 1 mM EDTA, pH 6.0, 37°C, 18.8 T for H4, 23.5 T for H3. Insets: notable peak shifts are highlighted.
(B) NMR CSPs calculated from spectra in (A). Note that vertical axes (CSPs in Hz) have been differently scaled for each histone to accommodate all datapoints. Horizontal dashed lines denote CSP = 10 Hz. Vertical dashed lines indicate the positions of PARylated series in H3.
(C) $J(0)$ (s rad^{-1}) vs. H3 residue number. Vertical dashed lines indicate Ser10 and Ser28. Legend: PARylated, 100 mM NaCl (red filled circles); Unmodified, 100 mM NaCl (black filled circles); PARylated, 0 mM NaCl (yellow open circles); Unmodified, 0 mM NaCl (blue open circles). Arrows indicate 'Less Dynamic' (up) and 'More Dynamic' (down).
(D) ^1H - ^{13}C methyl HMQCs (tail + core ILV-methyls) Unmodified / PARylated.
(E) NMR CSPs (Hz) vs. H3/H4 residue number. Vertical dashed lines indicate Ser10 and Ser28. Horizontal dashed lines indicate CSP = 10 Hz.

(legend continued on next page)

(Ser 10 and Ser 28) (Figure 2B). In contrast, CSPs in the other histone tails were much smaller in magnitude. The H4 N-terminal tail has a well-established role in forging interactions between nucleosomes via binding to the acidic patch on the surfaces of H2A and H2B. Thus, CSPs in this tail can report on the modulation of inter-nucleosomal interactions. Following PARylation, we measured only very modest CSPs across the H4 tail (Figures 2A and 2B). Similarly, small CSPs were recorded for specific regions of the H2A and H2B N-terminal tails, whereas the H2A C-terminal tail displayed negligible CSPs despite being relatively close to the H3 tail (Figures S3A and S3B).

Previous reports in human cells identified Ser10 and Ser28 in H3 and Ser6 in H2B as the primary sites of HPF1-dependent histone PARylation.^{35,85,86} However, under the conditions we have employed here, we only detected PARylation of Ser10 and Ser28 in H3 based on NMR CSPs (Figure 2A). We also note that although PARylation of H3 Ser10 was uniformly complete, some fraction of Ser28 remained unmodified under the same PARylation conditions based on the persistence of signal intensity for the unmodified Ser28 resonance (Figure 2A). To estimate the amount of PAR attached to nNCPs in NMR samples, we extracted and purified (under denaturing conditions) the PARylated H3 out of modified, intact nNCPs in which H3 was uniformly ¹⁵N-, ¹³C-labeled (see STAR Methods). NMR signals derived from adenosine ring protons in ADP-ribose and H3 methyl and methylene ¹³C-¹H groups were integrated and compared against standards of known concentration. Based on this analysis, there were, on average, 73.6 ± 4.2 ADP-ribose moieties attached to each H3 molecule in PARylated nNCP NMR samples (note that there are two H3 subunits per NCP).

We used a suite of ¹⁵N and ¹H N spin-relaxation experiments, separating fast, nanosecond (ns) to picosecond (ps) dynamics of the amide bond vector from slower μ s-ms motions, to measure the effects of PARylation on histone tail dynamics. As the tails are intrinsically disordered, it is difficult to separate amplitudes and time scales of motions; hence, we have chosen to report so-called $J(0)$ values that are proportional to the product $S^2\tau_c$, where S is an order parameter quantifying the amplitude of N-H bond vector motions, and τ_c is an effective correlation time for the motion of the bond vector. Per-residue $J(0)$ values increase as the motion of the bond vector becomes more constrained and moves more slowly, so that, qualitatively, increasing $J(0)$ values correlate with enhanced rigidity. As was observed in the CSP analysis, the H3 N-terminal tail exhibited the most dramatic changes in $J(0)$ following PARylation (Figure 2C). Almost all H3 tail residues tended toward lower $J(0)$ values in the presence of PARylation, consistent with greater mobility across the full extent of the tail. Notably, relatively low $J(0)$ values were observed for two regions spanning Ser10-Gly13 and Ala31-Lys36 compared with surrounding residues in

the unmodified state, showing that some regions of the H3 tail are highly mobile even in the absence of PARylation. In the other histone tails, PARylation resulted in very small changes in $J(0)$, demonstrating little effect on the ns-ps timescale motions of these regions (Figures S3E–S3G). However, some small changes mapped to the same DNA-proximal residues in the H2B N-terminal tail (approximately Thr22-Lys25) that showed significant CSPs following PARylation (Figures S3B and S3F).

From these data alone, it is difficult to determine whether the PAR-dependent changes in H3 tail dynamics emanate from altered interactions within a single nNCP (i.e., “intra-nucleosomal” interactions) or from changes in interactions between nucleosomes. Ionic strength has previously been shown to modulate inter-nucleosomal interactions, with lower salt concentrations giving rise to weaker NCP self-association, as discussed in more detail subsequently. Previous studies in our laboratory have shown that in the presence of 100 mM NaCl, the translational diffusion of NCPs becomes slower with increasing NCP concentration, consistent with a small degree of self-association, whereas in the absence of salt, this is not observed.⁹ Thus, one way of establishing whether interactions are within or between neighboring nNCPs is to carry out experiments at different salt concentrations; the absence of a salt dependency then provides strong evidence for intra-nucleosomal effects. With this in mind, we tested whether lowering the salt concentration in H3-labeled nNCP samples from 100 mM, which was typically used, to 0 mM NaCl (20 mM sodium phosphate was present in all samples) would change the $J(0)$ profile for H3 in PARylated or unmodified nNCPs. Notably, the results obtained in the presence and absence of salt were largely comparable (Figure 2C). $J(0)$ values recorded across the unmodified H3 N-terminal tail were very similar between the two salt conditions, showing that disrupting inter-nucleosomal interactions via changes in salt concentration did not lead to an increase in H3 tail mobility. A similar lack of salt dependence on tail motions was observed in a comparison of PARylated samples, where widespread decreases in $J(0)$ values were noted in the presence and absence of salt. These data strongly support the notion that changes in structural dynamics upon PARylation reflect changes in intra-nucleosomal interactions as opposed to changes in inter-particle contacts.

PARylation has negligible effects on histone core structure and dynamics

In order to establish how PARylation affects the structural dynamics of the histone core, we used methyl-transverse relaxation optimized spectroscopy (TROSY) NMR⁸⁷ to probe PAR-dependent changes in the ordered segments of each histone. In contrast to ¹⁵N-based experiments that lack the sensitivity for studies of rigid regions in high-molecular-weight particles, the

(C) Per-residue $J(0)$ values calculated for the H3 N-terminal tail in PARylated (red, filled circles) and unmodified (black, filled circles) nNCPs at 100 mM NaCl, or PARylated (gold, unfilled circles) and unmodified (blue, unfilled circles) nNCPs at 0 mM NaCl, all at 37°C. Vertical hatched lines indicate positions of PARylated residues. Error bars represent propagated uncertainty from NMR experiments used to obtain spectral density values (see STAR Methods).

(D) ¹H-¹³C methyl HMQC spectra of H3 and H4, with (red) and without (black) PARylation, in 20 mM sodium phosphate, 100 mM NaCl, 1 mM EDTA, pH 6.0, 37°C, 23.5 T. Asterisks (*) denote aliased peaks.

(E) CSPs calculated from spectra in (D). Horizontal hatched lines denote CSP = 10 Hz.

See also Figure S3.

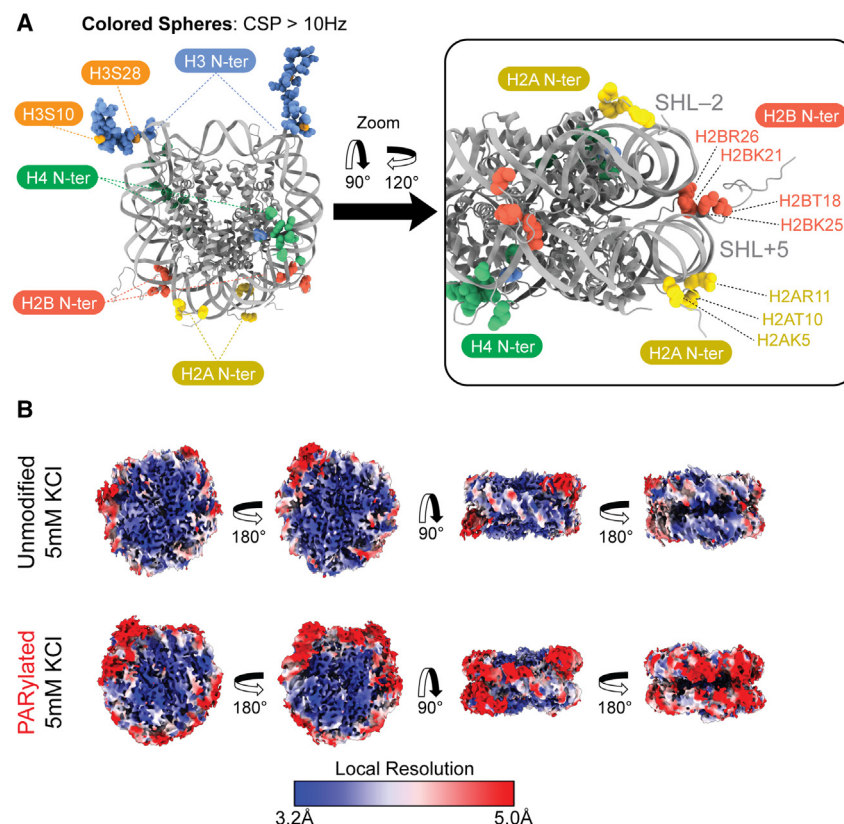


Figure 3. Structural dynamics of poly(ADP-ribosylated) nNCPs focusing on histone tails and DNA

(A) Cartoon illustration of the NCP (PDB: 1KX5⁹¹), showing positions of histone residues (3D spheres) that displayed PARylation-dependent CSPs > 10 Hz in ¹H-¹⁵N HSQC and ¹H-¹³C methyl HMQC spectra. Color-coding for each histone is as follows: H2A (gold), H2B (red), H3 (blue), and H4 (green). PARylated serine residues in H3 are marked in orange. Regions of the NCP for which no information is available from NMR analyses or for which CSPs < 10 Hz are depicted in gray. Right inset: zoomed-in perspective of the H2B N-terminal tails emerging between the DNA gyres, highlighting PARylation-dependent CSPs. H2A and H4 N-terminal tails are also visible. H3 tails are omitted for clarity.

(B) Cryo-EM electron density maps of PARylated and unmodified nNCPs colored by local resolution. Four different views of the same two density maps (unmodified and PARylated) are shown. Samples were prepared in “low” salt conditions: 20 mM Tris, 5 mM KCl, 0.1 mM EDTA, pH 7.5. See also Figures S3 and S5.

utility of methyl-TROSY-based experiments in this regard is now well established.^{88,89} We therefore prepared four samples, where in each case, methyl groups in Ile (only δ1), Leu, and Val residues of one histone were labeled with ¹³C and ¹H (“ILV-labeled”; only one of the two prochiral methyls of Val and Leu was randomly ¹³CH₃-labeled⁹⁰) in an otherwise ¹²C, ²H background. Remarkably, ¹H-¹³C heteronuclear multiple quantum coherence (HMQC) spectra of ILV-labeled H3—the only histone to be directly modified—in unmodified and PARylated nNCPs were almost identical (Figure 2D and 2E). The only notable CSPs were detected in methyl resonances originating from Leu20, which is unsurprising, given its position within the N-terminal tail. Analysis of methyl resonances from other histones yielded comparable results, although subtle CSPs were noted in the H4 N-terminal tail (in Ile0—a non-native isoleucine residue inserted at the N-terminal tail, Leu10, Leu21, and Val22) (Figures 2D and 2E). Changes in peak intensities can be indicative of dynamical changes on the μs-ms time scale, as has been observed in previous studies.⁹ However, we could not detect any such changes in ILV-H3 HMQC spectra between PARylated and unmodified nNCPs. These results suggest that PARylation does not produce structural or dynamical μs-ms changes in the histone core region.

By mapping the CSPs from our ¹⁵N- and methyl-TROSY-based NMR experiments onto a structural model of the NCP, we can conclude that PARylation solely induces perturbations in the histone tails (Figure 3A). Principle among those affected is the H3 N-terminal tail, whose direct attachment to the PAR chains prob-

ably dictates this larger effect. The H4 N-terminal tail also showed smaller PAR-dependent amide and methyl CSPs. CSPs detected in the H2A and H2B tails were small in comparison with H3 and tended to cluster near where these tails emerge from the core, in close proximity to DNA. For instance, some of the largest PAR-dependent CSPs observed in the H2B N-terminal tail correspond to cationic residues sandwiched between the DNA gyres (e.g., Lys21, Lys25, and Arg 26) (Figure 3A).

Effects of nucleosome PARylation extend beyond histone tail interactions

Aside from the case of H3, our NMR dynamics data argue against a widescale loss of histone tail-DNA interactions following PARylation. We asked, then, whether removal of all tails might result in an even greater enhancement of ligation than PARylation. Limited proteolysis has previously been used to remove flexible regions of the NCP such as the tails while keeping the core structure intact.^{18,92} We subjected nNCPs to the same treatment before purifying and assessing the integrity of the resulting “tailless” nNCPs by size exclusion chromatography (Figure S4A) and native gel electrophoresis (Figure S4B). In both cases, trypsinization manifested in a homogeneous nNCP species with no aggregation. Surprisingly, PARylated nNCPs were ligated more extensively than trypsinized nNCPs at all tested XRCC1/LIG3 concentrations (Figures S4C–S4E). These data suggest that liberation of histone tail-DNA interactions cannot fully account for the stimulatory effects of PARylation on nNCP ligation rates.

PARylation enhances DNA conformational flexibility without major disruptions to the core structure

Finding that histone tail removal was less effective than PARylation in promoting DNA ligation, we then asked whether PARylation

Table 1. Cryo-EM data collection and refinement statistics

	Sample condition			
	Unmodified nNCP 100 mM KCl	PARYlated nNCP 100 mM KCl	Unmodified nNCP 5 mM KCl	PARYlated nNCP 5 mM KCl
Magnification			75,000	
Voltage (keV)			300	
Electron exposure ($e^- \text{Å}^{-2}$)			40	
Defocus range (μm)			1.0–2.0	
Raw pixel size (Å)			1.03	
Symmetry imposed			C1	
<i>Ab initio</i> number of particle images	450,543	431,062	298,432	184,286
Number of particle images after cleaning	213,430	175,028	200,627	56,805
Final number of particle images (3.8 Å map with a loose mask)	42,000	18,000	200,627	40,000
Map resolution (Å , corrected FSC with auto-tightened mask)	3.5	3.3	3.7	3.4
FSC threshold	0.143	0.143	0.143	0.143
Map resolution range (Å)	2.2–11.2	2.2–13.4	2.2–9.3	2.2–12.0

directly affects the dynamics of nucleosomal DNA. However, the relative rigidity of DNA coupled with the slow tumbling rate of the NCP makes ^{15}N -based NMR spin-relaxation experiments on DNA untenable. Although methyl TROSY-based experiments focusing on methyl-labeled DNA bases have been performed,⁹³ the samples are both time-consuming and costly to produce. Therefore, we opted to compare unmodified and PARYlated nNCPs using cryo-EM, focusing particularly on the local resolution of DNA density (Figure S5A; Table 1). Resolution losses can indicate enhanced conformational flexibility, which, when analyzed in a region-specific manner across the density map, can effectively localize increases in motion.

The cryo-EM maps of unmodified and PARYlated nucleosomes were very similar, especially in the histone core (Figures 3B, S5B, and S5C). There were no significant changes in resolution of the core regions between the two types of nNCPs, which is consistent with our methyl-TROSY data (Figures 2D, 2E, S3C, and S3D). In contrast, a general worsening of resolution across the entire length of DNA was observed for the PARYlated nucleosome (Figures 3B and S5C). Regions exhibiting the poorest local resolution clustered toward the DNA termini in both the unmodified and PARYlated nNCPs, which likely emanate from intrinsic unwrapping motions. To account for the possibility that poorer resolution reflected potentially high salt concentrations in cryo-EM samples containing 100 mM KCl and to determine if differences in local resolution occurred consistently in an independent structure determination, we repeated the cryo-EM study at 5 mM KCl. Varying the salt concentration did not lead to noticeable differences in nNCP conformation or in the pattern of variation in local resolution, with an exception being that one of the DNA termini was unresolved in the unmodified nNCPs at 5 mM KCl (Figure 3B). Thus, the density maps and associated local resolution measurements performed at different salt concentrations corroborate that PARYlation enhances the conformational flexibility of nucleosomal DNA while leaving the core unchanged.

We then used hydrogen/deuterium exchange mass spectrometry (HDX-MS) to further study the impact of PARYlation on nNCP conformational dynamics at the level of backbone amides. Detecting differences in the relative uptake of deuterium can report on PARYlation-dependent changes in solvent accessibility and hydrogen bonding in the histone core. Unmodified and PARYlated nNCPs were subjected to HDX-MS under identical conditions, except PARYlated samples additionally contained automodified mChPARP1 and HPF1. Similar to previous work,⁹⁴ we obtained excellent sequence coverage for the histone core and minimal coverage for the tails. In both the unmodified and PARYlated samples, most peptides originating from the histone core regions displayed low or negligible deuterium uptake, consistent with previous HDX-MS measurements indicating structural rigidity in the core.^{94,95} Certain regions of H3 located in proximity to the DNA termini exhibited very slow, time-dependent increases in deuterium uptake (red box, Figure S5D); however, the differences in the exchange rates between the unmodified and PARYlated sample were negligible (Figure S5E). Consistent with our cryo-EM and methyl-TROSY data, HDX-MS confirms that PARYlation does not impact the conformation or exposure of the histone core.

PARYlation inhibits nucleosome-nucleosome interactions

As previously stated, nucleosomes can self-associate to form oligomers in solution, even in the absence of extrinsic-binding factors. In our cryo-EM experiments, we sometimes observed filamentous nNCP oligomers (Figure 4A). Notably, these structures were never seen in PARYlated nNCP samples under the same conditions, suggesting that PARYlation abrogates NCP oligomerization.

NCP oligomers populate a distribution of sizes based on the propensity of monomers to self-associate. We previously developed a model for quantifying these affinities based on the assumption that NCP oligomers form via stacking of monomers,

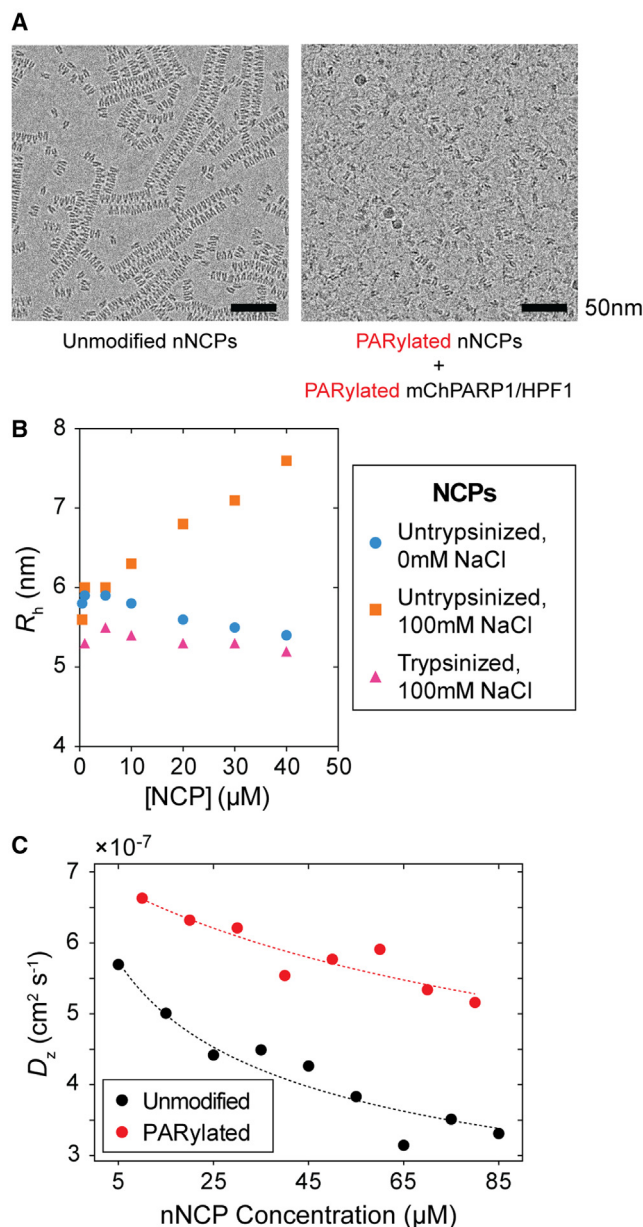


Figure 4. Nucleosome-nucleosome interactions are weakened by poly(ADP-ribosylation)

(A) Cryo-EM micrographs of unmodified and PARylated nNCPs captured in the presence of 100 mM NaCl. Note that only a fraction of the unmodified nNCP samples showed the extensive stacking seen here. Scale bars: 50 nm.

(B) Average hydrodynamic radii (R_h) calculated from DLS measurements of nNCP samples containing different salt and nNCP concentrations and/or following trypsinization.

(C) Diffusion coefficients (D_z) measured by NMR-pulsed field gradient experiments on unmodified (black) or PARylated (red) nNCP samples at different concentrations, 25°C. All samples contained 20 mM sodium phosphate, 100 mM NaCl, 1 mM EDTA, pH 6.0. Fitted curves were extracted from a self-association model where nNCPs interact in a stacking mode.⁹

See also Figure S4.

as visualized in some of our cryo-EM images.⁹ In this model, higher NCP-NCP interaction affinities correlate with more frequent sampling of larger complexes possessing higher effective hydrodynamic radii. Therefore, diffusion data correlating hydrodynamic radius with NCP concentration can be used to estimate the affinity of NCP-NCP interactions within this stacking mode along with the average number of particles in a stacked complex in solution. Dynamic light scattering (DLS) measurements revealed that nNCPs exhibit increased hydrodynamic radii as a function of nNCP concentration (100 mM NaCl), which is consistent with oligomerization (Figure 4B). As expected, this increase was salt-dependent. Excluding NaCl from the sample caused the average hydrodynamic radius to decrease as a function of nNCP concentration, possibly due to nonideality in the diffusive behavior of the highly charged nNCPs.⁹⁶ Trypsinized nNCPs failed to self-associate at 100 mM NaCl, suggesting that the tails contribute to this behavior, as has been previously appreciated especially in the case of H4.^{97–100}

To further clarify how PARylation impacts nucleosome self-association, we measured nNCP diffusion using NMR pulsed-field gradient experiments,¹⁰¹ focusing on methyl resonances originating from PARylated or unmodified nNCPs. Surprisingly, we found that PARylated nNCPs exhibited a higher diffusion coefficient than their unmodified counterparts at each concentration point (Figure 4C). This contradicted the expectation that adding PAR chains to NCPs would substantially enlarge their hydrodynamic radii and retard diffusion. The apparent diffusion coefficients measured in both samples decreased as a function of nNCP concentration, although significantly less so in the PARylated case (Figure 4C). By fitting the data to the aforementioned stacking model, we calculated an approximately 3-fold decrease in the affinity of nNCPs to self-associate following PARylation (K_D values of 42 ± 25 and 185 ± 100 μ M for the unmodified and PARylated nNCPs, respectively). These affinity estimates are qualitative due to the absence of observable stacking morphologies in PARylated nNCP samples. Nevertheless, these data show that PARylation decreases the formation of higher-order oligomeric assemblies of nNCPs.

PARYlation modulates biomolecular condensates containing XRCC1/LIG3, nucleosomes, and mChPARP1

Under certain conditions, polynucleosomal arrays phase separate into dense, liquid-like condensates.²³ Phase separation is driven by nucleosome-nucleosome interactions that are compounded when nucleosomes are concatenated in an array. Although mononucleosomes engage in similar kinds of associative interactions, they lack this multivalent character and are therefore expected to phase separate less readily. Moreover, our diffusion data suggest that PARylation weakens nucleosome-nucleosome interactions and, thus, might disfavor phase separation even further (Figure 4C). However, we noted that the components of our *in vitro* ligation assays (i.e., mChPARP1/HPF1 and XRCC1/LIG3) form a rich network of interactions with each other as well as with PAR and DNA (Figure 5A).^{71,78,102–108} This led us to wonder whether PAR-binding proteins could counteract the decondensing effects of PARylation to instead promote phase separation by introducing

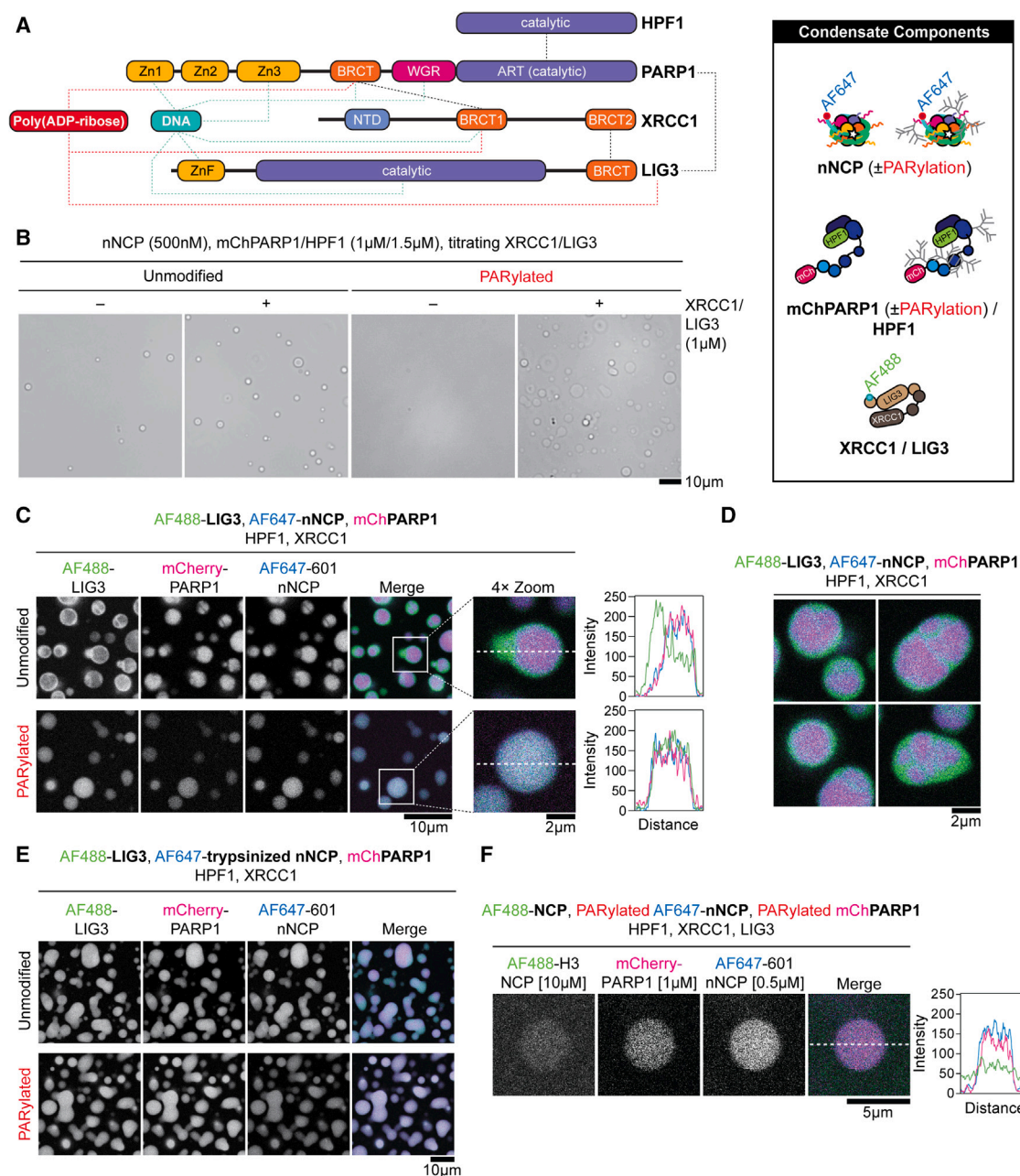


Figure 5. Poly(ADP-ribosylation) regulates colocalization of nNCPs with various factors within condensates

(A) Left, schematic representation of the domain organization and known interactions between PARP1, HPF1, XRCC1, and LIG3 (black hatched lines), and with PAR (red hatched lines) and DNA (turquoise hatched lines). Zn1,2,3, zinc-binding domains 1, 2, and 3; BRCT, breast cancer type 1 susceptibility protein C-terminal domain; WGR, tryptophan-glycine-arginine-rich domain; ART, ADP-ribosyltransferase domain; NTD, N-terminal domain; ZnF, zinc-finger domain. Right, graphic illustration of condensate components with potential labeling schemes and PTMs.

(B) Differential interference contrast (DIC) micrographs of nNCP samples containing mChPARP1/HPF1 (1 μM/1.5 μM, respectively), with or without XRCC1/LIG3 (1 μM) and PARylation. Micrographs including PARylation were contrast-adjusted to better highlight features. Scale bar: 10 μm.

(C) Fluorescence micrographs of condensate samples containing partially AF488-labeled LIG3 (1 μM), XRCC1 (1 μM), mChPARP1/HPF1 (1 μM/1.5 μM), and partially AF647-labeled nNCPs (500 nM), with or without PARylation. Right, plot depicting fluorescence intensities measured in each indicated channel as a function of distance along the hatched white line in the adjacent merged image. Scale bars: 10 or 2 μm (zoomed-in panels).

(D) Examples of condensates from the unPARylated condition in (C). Fluorescent channels are overlaid and depicted in the same color scheme for clarity. Scale bar: 2 μm.

(E) Fluorescence micrographs of condensate samples containing trypsinized, partially AF647-labeled nNCPs (500 nM), partially AF488-labeled LIG3 (1 μM), XRCC1 (1 μM), mChPARP1/HPF1 (1 /1.5 μM), with or without PARylation. Scale bar: 10 μm.

(legend continued on next page)

new interactions into the system—both with each other and with PARylated nucleosomes.

By light microscopy, we found that mChPARP1 and nNCPs form spherical condensates in the absence of PARylation (Figures 5B and S6A). Titrating in XRCC1 and LIG3 did not alter the appearances of the condensates. In the absence of XRCC1 and LIG3, PARylation completely dispersed the condensates, suggesting that, in the absence of other proteins, PARylation diminishes the propensity of PARP1 and nNCPs to phase separate. However, as the XRCC1/LIG3 concentration increased, droplets began to appear (Figures 5B and S6A). These results are consistent with the expectation that PARylation reduces condensate formation by diminishing nucleosome-nucleosome and nucleosome-PARP1 interactions. Conversely, PAR-binding proteins such as XRCC1 and LIG3 can again promote condensate formation above a sufficient concentration in the presence of PARylation.

XRCC1 and LIG3 engage in a specific interaction involving their breast cancer type 1 susceptibility protein C-terminal (BRCT) domains (Figure 5A). To test whether this interaction contributes to condensate formation, we purified a truncated variant of LIG3 lacking the BRCT domain (LIG3 Δ BRCT) and titrated it into nNCP PARylation reactions containing XRCC1 at constant concentration. We did not witness condensate formation in the same range of concentrations previously tested with full-length LIG3 (Figure S6B). We also titrated full-length LIG3 into PARylated samples excluding XRCC1, finding again that condensates did not form under the same range of concentrations (Figure S6C). Together, these results demonstrate that both XRCC1 and LIG3 contribute to condensate formation in the presence of PARylation and that specific interactions involving the LIG3 BRCT domain are essential for this behavior.

We then asked whether condensate formation would affect ligation rates. We again exploited the LIG3 Δ BRCT mutant, predicting that disrupting the LIG3-XRCC1 interaction would abrogate condensate formation while leaving ligase activity unchanged. LIG3 Δ BRCT exhibited similar ligation rates on PARylated nNCPs as the full-length enzyme despite failing to promote condensate formation under the same conditions (Figure S6D). Similarly, varying the XRCC1 concentration in the ligation reactions modulated condensate formation but did not affect ligation (Figure S6E), further suggesting that ligation and condensate formation are not correlated under these conditions.

As a correlation between condensation and LIG3 activity was not observed, we wondered whether condensation could impact function through the recruitment of key molecular components. Condensates organize biochemically active molecules within cellular space, enabling colocalization of molecules with correlated activities or, conversely, segregation of molecules whose activities are orthogonal.¹⁰⁹ As DNA repair foci recruit specific repair factors to damage sites within chromatin, we wondered if our *in vitro* condensates could also regulate colocalization of DNA repair factors and nNCPs in a PARylation-dependent

manner. To examine the spatial organization of components within nNCP-containing condensates, we prepared AF488-labeled versions of LIG3 and XRCC1 along with mChPARP1 and AF647-labeled nNCPs for visualization by fluorescence microscopy. XRCC1 and LIG3 were included at sufficiently high concentrations (1 μ M each) to instigate condensation regardless of whether PARylation had been induced (Figure 5C). In the absence of PARylation, mChPARP1 and AF647-labeled nNCPs preferentially localized to an internal compartment surrounded by an outer ring of intense AF488-LIG3 signal (Figures 5C and 5D). Similar results were obtained when XRCC1 was labeled instead of LIG3, implying that the two colocalize (Figure S6F). Strikingly, PARylation caused the AF488-LIG3 (or AF488-XRCC1), mChPARP1, and AF647-nNCP signals to colocalize homogeneously within a single compartment, abrogating the segregated morphology seen in the absence of PARylation (Figures 5C, 5D, and S6F). Given that histone tail interactions significantly contribute to phase separation,^{23,24} we evaluated how removing the tails impacts the morphologies of NCP-containing condensates. Interestingly, condensates containing trypsinized nNCPs exhibited colocalization of nNCPs, mChPARP1, and LIG3 even in the absence of PARylation (Figure 5E). Thus, histone tail interactions and PARylation contribute to the multiphasic character of the condensates, with removal of the former and inclusion of the latter promoting colocalization of all visible components, particularly XRCC1/LIG3, with PARP1 and nNCPs.

We then tested whether PARylated nNCPs partition more strongly inside condensates than unmodified NCPs. We combined PARylated, AF647-labeled nNCPs with a 20-fold molar excess of unmodified, unnicked NCPs partially labeled with AF488 on histone H3, along with automodified mChPARP1, HPF1, and XRCC1/LIG3 (both unlabeled) (Figure 5F). PARylated nNCPs were highly enriched in the droplets (partition coefficient, 11.4 ± 0.7 , $n = 30$ droplets), whereas unPARylated NCPs were more evenly distributed inside and outside the condensates (partition coefficient, 1.4 ± 0.2 , $n = 30$ droplets). Thus, PARylation strongly enhances nNCP partitioning within condensates, whereas unmodified nNCPs are only weakly enriched, even while being present at a far higher concentration. Selective co-enrichment of repair factors and PARylated nucleosomes harboring DNA damage sites inside condensates may increase the frequency of repair-promoting interactions while disfavoring competing, unproductive interactions between enzymes and undamaged chromatin. In this manner, condensate formation could play a role in regulating repair activities such as ligation in the complex nuclear environment.

In addition to LIG3, several SSBR- and base excision repair (BER)-related proteins are recruited to DNA repair foci via interactions with PAR or XRCC1, which function as protein interaction “scaffolds” at damage sites.¹¹⁰ During the DNA damage response, XRCC1 is phosphorylated by casein kinase 2 (CK2), which greatly enhances its affinity to interact with SSBR- and BER-related proteins possessing phosphoprotein binding

(F) Representative fluorescence micrographs of a condensate prepared with partially AF647-labeled PARylated nNCPs (500 nM), PARylated mChPARP1/HPF1 (1/1.5 μ M), XRCC1/LIG3 (1 μ M), and partially AF488-labeled unnicked, unmodified NCPs (10 μ M). Right, plot depicting fluorescence intensities measured in each indicated channel along the hatched white line in the adjacent merged image. Scale bar: 5 μ m.

See also Figures S6 and S7.

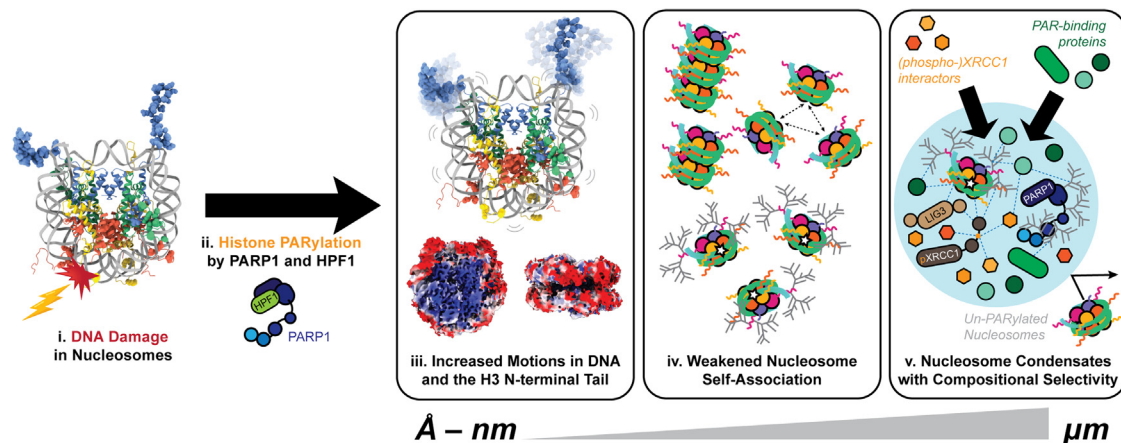


Figure 6. Poly(ADP-ribose)ylation affects nucleosome structural dynamics and spatial organization across different length scales

(i) Damage occurs in nucleosomal DNA. (ii) PARP1 and HPF1 are recruited to nucleosomal DNA damage sites and catalyze PARylation of the H3 N-terminal tails. (iii) PARylation enhances H3 tail motions on the ns-ps timescale and induces DNA conformational fluctuations, correlating with enhanced accessibility of the DNA toward MNase, LIG3, and likely other enzymes. (iv) PARylation weakens interactions between nucleosomes, preventing their association into higher-order oligomers. (v) Histone PARylation forges interactions between nucleosomes and PAR-binding proteins such as XRCC1 and LIG3, which promote formation of biomolecular condensates. Other proteins, including PAR-binding proteins and those which interact with CK2-phosphorylated XRCC1, also contribute to condensation and favorably partition with their cognate binding partners. Undamaged nucleosomes, which are not PARylated, are not enriched inside condensates. Differential condensate partitioning may act as a mechanism for enforcing selective localization of factors to sites of DNA damage in chromatin.

domains, such as forkhead associated (FHA) domains (Figure S6G).^{110,111} We assessed the localization of three other PAR- and XRCC1-interacting DNA-repair factors, polynucleotide kinase 3'-phosphatase (PNKP), aprataxin (APTX), and aprataxin and PNKP-like factor (APLF), inside condensates containing PARylated or unmodified nNCPs and CK2-phosphorylated XRCC1 (Figures S6H–S6J and S7). Like LIG3, APLF, APTX, and PNKP failed to colocalize with mChPARP1 and nNCPs in the absence of PARylation, instead occupying distinct subcompartments within multiphasic condensates (Figures S7D and S7E). PARylation caused all factors to colocalize inside homogeneous single-phase droplets, showing that PARylation-dependent compartmentalization follows a consistent pattern across these examples (Figure S7C). Furthermore, phosphorylation of XRCC1 greatly enhanced the partitioning of APLF, APTX, and PNKP inside PARylated-nNCP condensates, whereas DNA polymerase β (POLB), which interacts with XRCC1 via a phospho-independent interface,¹¹² partitioned strongly in the presence or absence of XRCC1 phosphorylation (Figure S7B). These results show that PARylation and XRCC1 phosphorylation regulate the spatial organization and enrichment of DNA repair factors within biomolecular condensates according to their known interaction tendencies, possibly reflecting an important element of these PTMs' functionality in the formation of DNA repair foci.

DISCUSSION

Epigenetic modifications are one of several essential ways by which chromatin structure and conformation are regulated. In this regard, PARylation has at least two well-established functions. First, PARylation of histones causes decompaction of chromatin in specific regions of the nucleus. Second, PAR

chains recruit interacting factors, such as chromatin remodelers, that may impart their own modifications to chromatin structure in a localized fashion. Through these direct and indirect activities, PARylation enhances the accessibility of chromatin to various DNA-templated biochemical reactions. Although the biological significance of PARylation is clear, it is unclear how these functions correlate with changes in nucleosome structure and dynamics. In this study, we demonstrated that PARylation impacts multiple aspects of nucleosome structure, spanning from the atomic-scale motions of individual NCP components to the micron-scale organization of nucleosomes and other factors within biomolecular condensates (Figure 6).

A notable property of PAR is its extensive size. *In vitro* estimates of PAR chain length often surpass thirty-five units, potentially reaching up to ~ 100 nm long.^{72,113} Here, using NMR, we estimated chain lengths of ~ 75 ADP-ribose units associated per histone H3. In an extended conformation, chains of such length could exceed the diameter of a single NCP, even without considering the presence of extensive branches.^{114,115} By virtue of its size, PAR could potentially interact with and alter the dynamics of all the histone tails despite attachment to only one. However, our backbone ^{15}N NMR spin-relaxation measurements only indicated significant enhancements in the ns-ps time scale dynamics of the H3 N-terminal tail following PARylation. These observations mirror the effects of other histone PTMs studied to date, such as phosphorylation and lysine acetylation.^{9,116–119} Although these modifications are chemically quite distinct, they all alter the charge characteristics of the tails, either by imparting more negative charge, as is the case with PARylation, or by neutralizing pre-existing positive charges. Evidence from simulations and experimentation have both related these chemical changes to a weakening of electrostatic interactions between the tails and the DNA.⁸³ Methyl spectra reporting

on core residues showed negligible changes in peak intensities or positions in all four histones, implying that PARylation had little impact on core structural dynamics, and, hence, little coupling of motions in the tails and core.

In this study, we conducted ligation experiments on NCPs containing a single-strand nick located relatively far from the H3 tail. The connection between changes in H3 tail dynamics and ligation of a distant nick site likely reflects the unique H3 N-terminal tail position within the NCP; its protrusion near the DNA entry and exit sites endows it with a special degree of influence over DNA breathing motions.^{11,120} Deletion of this tail was shown to destabilize the NCP and promote higher populations of an unwrapped state.¹⁵ Although PARylation diminishes tail-DNA interactions in the case of H3, additional factors must account for the influence of PARylation on ligation rates, as we found that removing all the histone tails—including that of H3—did not stimulate ligase activity to the same degree as PARylation. Our cryo-EM local resolution analyses show PARylation-dependent increases in DNA conformational flexibility without structural perturbation of the histone core. These results suggest an important functional consequence: that PARylation enhances nucleosomal DNA accessibility and ligase activity while leaving the overall conformation of the nucleosome intact. The loss in local resolution across the entire length of DNA further suggests that PARylation can affect long-range dynamical changes despite being confined to one histone tail. This may enable PAR to enhance repair reactions, regardless of where damage sites occur relative to H3 within nucleosomes—an important consideration, given that damage can occur at essentially any position within chromatin.

Due to their large size and repetitive structure, PAR chains can support multiple interactions, making them a likely candidate for driving condensate formation.⁵⁷ Indeed, the involvement of PARylation in biomolecular condensate formation has been previously demonstrated in other systems.^{46–48,57,121,122} In the present case, PARP1, HPF1, and NCPs formed condensates that are disrupted by PARylation, while introducing additional PAR-binding proteins such as XRCC1 and LIG3 promoted condensation. Thus, it would be an oversimplification to state that PARylation generally favors or disfavors phase separation; rather, the effects of this modification depend on the context of its interacting proteins and their own states of post-translational modification.

Although the *in vitro* condensates considered here have extremely simplified compositions, they recapitulate several interesting qualities associated with nuclear DNA damage foci. We highlight the role of XRCC1 and LIG3 as two PAR-binding proteins that interact with PARylated nucleosomes to form condensates. In cells, it has been shown that XRCC1 and LIG3 form dense nuclear puncta in a DNA damage-dependent manner. Mutating key residues in the BRCT1 domain of XRCC1 prevents it from interacting with PAR and accumulating within these structures.¹⁰² Deletion of the LIG3 BRCT domain similarly prevents its colocalization with DNA damage-induced foci.¹²³ We found that XRCC1/LIG3 condensate formation was disrupted by similar perturbations *in vitro*: excluding XRCC1 or truncating LIG3 abolished condensation of PARylated nNCPs and PARP1, showing that common interactions underlie the formation of our *in vitro* condensates and DNA damage foci.

Recent studies have illustrated the potential roles of phase separation in chromatin organization.^{124–126} Gibson et al. demonstrated that polynucleosome arrays form liquid-like condensates with distinct compartments regulated by histone acetylation.²³ Our own microscopy data suggest that PARylation and phosphorylation regulate enrichment and compartmentalization of DNA repair proteins within condensates centered on nucleosomes. We propose that focal accumulation of repair proteins in cells occurs dynamically within condensates nucleated by PARylation and key scaffold molecules such as XRCC1. In this manner, condensation may provide a physical mechanism for translating DNA damage-dependent signaling events into the spatial reorganization of DNA-repair functions. Reductive condensate models such as the one we have investigated provide a useful means for studying the overlapping functions of the many PTMs involved in DNA repair and provide a conceptual basis for examining the structural organization of DNA damage puncta in live cells.

Limitations of the study

The condensates we have analyzed herein have extremely simplified compositions compared with the diverse DNA repair foci existing in cells. Although this simplicity has enabled us to precisely control and analyze these condensates for the purposes of experimentation and to recapitulate some *in vivo* results, it is nevertheless a limitation. The lack of an observed correlation between condensate formation and ligase activity may reflect the simplicity of our model or, alternatively, that the main role of the condensate is one of organization. Future studies will be instrumental in further defining the nature of DNA damage foci and testing to what extent our *in vitro* insights can be applied to understanding the function of these compartments *in vivo*.

STAR★METHODS

Detailed methods are provided in the online version of this paper and include the following:

- **KEY RESOURCES TABLE**
- **RESOURCE AVAILABILITY**
 - Lead contact
 - Materials availability
 - Data and code availability
- **EXPERIMENTAL MODEL AND STUDY PARTICIPANT DETAILS**
 - Bacterial strains
- **METHOD DETAILS**
 - Cloning of bacterial expression plasmids
 - Recombinant protein and DNA purification
 - Protein modification
 - 601-DNA manipulation
 - NCP reconstitution and PARylation
 - Enzyme assays
 - Nuclear magnetic resonance spectroscopy
 - Hydrogen-deuterium exchange mass spectrometry
 - Cryogenic electron microscopy
 - Dynamic light scattering and fitting of diffusion data

- Light microscopy
- **QUANTIFICATION AND STATISTICAL ANALYSIS**
 - Ligation assays
 - Partition coefficients derived from fluorescence micrographs
 - Error analysis of $J(0)$ data

SUPPLEMENTAL INFORMATION

Supplemental information can be found online at <https://doi.org/10.1016/j.molcel.2023.12.019>.

ACKNOWLEDGMENTS

We acknowledge salary support from an Alexander Graham Bell Canada Graduate Scholarship – Doctoral Award (M.L.N.), a Canadian Institutes of Health Research (CIHR) Post-doctoral fellowship (S.K.H.), a Holmes Award from the National Research Council of Canada (T.H.K.), and a Restracom fellowship from the Hospital for Sick Children Research Institute (R.W.H.). We thank Nicolas Bolik-Coulon for providing purified ^{13}C , ^{15}N -labeled histone H3. We also acknowledge the SickKids Structural and Biophysical Core Facility for provision of and assistance with instrumentation used for DLS measurements. This work was supported by grants from the Natural Sciences and Engineering Research Council of Canada to S.V. (RGPIN-2021-02843), L.E.K. (2015-04347), and J.D.F.-K. (2016-06718) and from CIHR grants FND-50357 (L.E.K.) and FND-148375 (J.D.F.-K.).

AUTHOR CONTRIBUTIONS

Conceptualization, M.L.N., T.H.K., J.D.F.-K., and L.E.K.; formal analysis, M.L.N., T.H.K., S.K.H., R.W.H., and M.G.; funding acquisition, J.D.F.-K. and L.E.K.; investigation, M.L.N., T.H.K., S.K.H., R.W.H., and M.G.; resources, M.L.N., T.H.K., S.K.H., A.P., and M.T.; supervision, S.V., J.L.R., H.O.L., J.D.F.-K., and L.E.K.; visualization, M.L.N., T.H.K., S.K.H., R.W.H., and M.G.; writing – original draft, M.L.N. and L.E.K.; writing – review and editing, M.L.N., T.H.K., S.K.H., R.W.H., S.V., J.L.R., H.O.L., J.D.F.-K., and L.E.K.

DECLARATION OF INTERESTS

The authors declare no competing interests.

Received: August 29, 2023

Revised: October 30, 2023

Accepted: December 13, 2023

Published: January 11, 2024

REFERENCES

1. Luger, K., Dechassa, M.L., and Tremethick, D.J. (2012). New insights into nucleosome and chromatin structure: an ordered state or a disordered affair? *Nat. Rev. Mol. Cell Biol.* **13**, 436–447.
2. Luger, K., Mäder, A.W., Richmond, R.K., Sargent, D.F., and Richmond, T.J. (1997). Crystal structure of the nucleosome core particle at 2.8 Å resolution. *Nature* **389**, 251–260.
3. McGinty, R.K., and Tan, S. (2015). Nucleosome structure and function. *Chem. Rev.* **115**, 2255–2273.
4. Koyama, M., and Kurumizaka, H. (2018). Structural diversity of the nucleosome. *J. Biochem.* **163**, 85–95.
5. Ahmad, K., Henikoff, S., and Ramachandran, S. (2022). Managing the steady state chromatin landscape by nucleosome dynamics. *Annu. Rev. Biochem.* **91**, 183–195.
6. Shi, X., Zhai, Z., Chen, Y., Li, J., and Nordenskiöld, L. (2022). Recent advances in investigating functional dynamics of chromatin. *Front. Genet.* **13**, 870640.
7. Musselman, C.A., and Kutateladze, T.G. (2022). Visualizing conformational ensembles of the nucleosome by NMR. *ACS Chem. Biol.* **17**, 495–502.
8. Li, G., Levitus, M., Bustamante, C., and Widom, J. (2005). Rapid spontaneous accessibility of nucleosomal DNA. *Nat. Struct. Mol. Biol.* **12**, 46–53.
9. Kim, T.H., Nosella, M.L., Bolik-Coulon, N., Harkness, R.W., Huang, S.K., and Kay, L.E. (2023). Correlating histone acetylation with nucleosome core particle dynamics and function. *Proc. Natl. Acad. Sci. USA* **120**, e2301063120.
10. Kiteviski-LeBlanc, J.L., Yuwen, T., Dyer, P.N., Rudolph, J., Luger, K., and Kay, L.E. (2018). Investigating the dynamics of destabilized nucleosomes using methyl-TROSY NMR. *J. Am. Chem. Soc.* **140**, 4774–4777.
11. Armeev, G.A., Kniazeva, A.S., Komarova, G.A., Kirpichnikov, M.P., and Shaytan, A.K. (2021). Histone dynamics mediate DNA unwrapping and sliding in nucleosomes. *Nat. Commun.* **12**, 2387.
12. Shi, X., Prasanna, C., Soman, A., Pervushin, K., and Nordenskiöld, L. (2020). Dynamic networks observed in the nucleosome core particles couple the histone globular domains with DNA. *Commun. Biol.* **3**, 639.
13. Li, Z., and Kono, H. (2016). Distinct roles of histone H3 and H2A tails in nucleosome stability. *Sci. Rep.* **6**, 31437.
14. Brower-Toland, B., Wacker, D.A., Fulbright, R.M., Lis, J.T., Kraus, W.L., and Wang, M.D. (2005). Specific contributions of histone tails and their acetylation to the mechanical stability of nucleosomes. *J. Mol. Biol.* **346**, 135–146.
15. Ferreira, H., Somers, J., Webster, R., Flaus, A., and Owen-Hughes, T. (2007). Histone tails and the H3 alphaN helix regulate nucleosome mobility and stability. *Mol. Cell Biol.* **27**, 4037–4048.
16. Rabadano, S.O., Shannon, M.D., Izmailov, S.A., Gonzalez Salguero, N., Zandian, M., Purusottam, R.N., Poirier, M.G., Skrynnikov, N.R., and Jaroniec, C.P. (2021). Histone H4 tails in nucleosomes: a fuzzy interaction with DNA. *Angew. Chem. Int. Ed. Engl.* **60**, 6480–6487.
17. Valieva, M.E., Gerasimova, N.S., Kudryashova, K.S., Kozlova, A.L., Kirpichnikov, M.P., Hu, Q., Botuyan, M.V., Mer, G., Feofanov, A.V., and Studitsky, V.M. (2017). Stabilization of nucleosomes by histone tails and by FACT revealed by spFRET microscopy. *Cancers (Basel)* **9**.
18. Ausio, J., Dong, F., and van Holde, K.E. (1989). Use of selectively trypsinized nucleosome core particles to analyze the role of the histone “tails” in the stabilization of the nucleosome. *J. Mol. Biol.* **206**, 451–463.
19. Allahverdi, A., Yang, R., Korolev, N., Fan, Y., Davey, C.A., Liu, C.F., and Nordenskiöld, L. (2011). The effects of histone H4 tail acetylations on cation-induced chromatin folding and self-association. *Nucleic Acids Res.* **39**, 1680–1691.
20. Otterstrom, J., Castells-Garcia, A., Vicario, C., Gomez-Garcia, P.A., Cosma, M.P., and Lakadamyali, M. (2019). Super-resolution microscopy reveals how histone tail acetylation affects DNA compaction within nucleosomes in vivo. *Nucleic Acids Res.* **47**, 8470–8484.
21. Gordon, F., Luger, K., and Hansen, J.C. (2005). The core histone N-terminal tail domains function independently and additively during salt-dependent oligomerization of nucleosomal arrays. *J. Biol. Chem.* **280**, 33701–33706.
22. Tse, C., and Hansen, J.C. (1997). Hybrid trypsinized nucleosomal arrays: identification of multiple functional roles of the H2A/H2B and H3/H4 N-termini in chromatin fiber compaction. *Biochemistry* **36**, 11381–11388.
23. Gibson, B.A., Doolittle, L.K., Schneider, M.W.G., Jensen, L.E., Gamarra, N., Henry, L., Gerlich, D.W., Redding, S., and Rosen, M.K. (2019). Organization of chromatin by intrinsic and regulated phase separation. *Cell* **179**, 470–484.e21.
24. Hammonds, E.F., Harwig, M.C., Paintsil, E.A., Tillison, E.A., Hill, R.B., and Morrison, E.A. (2022). Histone H3 and H4 tails play an important role in nucleosome phase separation. *Biophys. Chem.* **283**, 106767.

25. Buttress, T., He, S., Wang, L., Zhou, S., Saalbach, G., Vickers, M., Li, G., Li, P., and Feng, X. (2022). Histone H2B.8 compacts flowering plant sperm through chromatin phase separation. *Nature* **611**, 614–622.
26. Polach, K.J., Lowary, P.T., and Widom, J. (2000). Effects of core histone tail domains on the equilibrium constants for dynamic DNA site accessibility in nucleosomes. *J. Mol. Biol.* **298**, 211–223.
27. Allis, C.D., and Jenuwein, T. (2016). The molecular hallmarks of epigenetic control. *Nat. Rev. Genet.* **17**, 487–500.
28. Bowman, G.D., and Poirier, M.G. (2015). Post-translational modifications of histones that influence nucleosome dynamics. *Chem. Rev.* **115**, 2274–2295.
29. Caldecott, K.W. (2008). Single-strand break repair and genetic disease. *Nat. Rev. Genet.* **9**, 619–631.
30. Xie, N., Zhang, L., Gao, W., Huang, C., Huber, P.E., Zhou, X., Li, C., Shen, G., and Zou, B. (2020). NAD⁺ metabolism: pathophysiologic mechanisms and therapeutic potential. *Signal Transduct. Target. Ther.* **5**, 227.
31. Fisher, A.E., Hohegger, H., Takeda, S., and Caldecott, K.W. (2007). Poly(ADP-ribose) polymerase 1 accelerates single-strand break repair in concert with poly(ADP-ribose) glycohydrolase. *Mol. Cell. Biol.* **27**, 5597–5605.
32. Amé, J.C., Rolli, V., Schreiber, V., Niedergang, C., Apiou, F., Decker, P., Muller, S., Höger, T., Ménissier-de Murcia, J., and de Murcia, G. (1999). PARP-2, a novel mammalian DNA damage-dependent poly(ADP-ribose) polymerase. *J. Biol. Chem.* **274**, 17860–17868.
33. Reber, J.M., and Mangerich, A. (2021). Why structure and chain length matter: on the biological significance underlying the structural heterogeneity of poly(ADP-ribose). *Nucleic Acids Res.* **49**, 8432–8448.
34. Alemasova, E.E., and Lavrik, O.I. (2019). Poly(ADP-ribosylation) by PARP1: reaction mechanism and regulatory proteins. *Nucleic Acids Res.* **47**, 3811–3827.
35. Bonfiglio, J.J., Fontana, P., Zhang, Q., Colby, T., Gibbs-Seymour, I., Atanassov, I., Bartlett, E., Zaja, R., Ahel, I., and Matic, I. (2017). Serine ADP-ribosylation depends on HPF1. *Mol. Cell* **65**, 932–940.e6.
36. Jungmichel, S., Rosenthal, F., Altmeyer, M., Lukas, J., Hottiger, M.O., and Nielsen, M.L. (2013). Proteome-wide identification of poly(ADP-ribosylation) targets in different genotoxic stress responses. *Mol. Cell* **52**, 272–285.
37. Ray Chaudhuri, A., and Nussenzweig, A. (2017). The multifaceted roles of PARP1 in DNA repair and chromatin remodelling. *Nat. Rev. Mol. Cell Biol.* **18**, 610–621.
38. Bacic, L., Gaullier, G., Sabantsev, A., Lehmann, L.C., Brackmann, K., Dimakou, D., Halic, M., Hewitt, G., Boulton, S.J., and Deindl, S. (2021). Structure and dynamics of the chromatin remodeler ALC1 bound to a PARylated nucleosome. *eLife* **10**, e71420.
39. Lehmann, L.C., Hewitt, G., Albara, S., Leitner, A., Marklund, E., Maslen, S.L., Maturi, V., Chen, Y., van der Spoel, D., Skehel, J.M., et al. (2017). Mechanistic insights into autoinhibition of the oncogenic chromatin remodeler ALC1. *Mol. Cell* **68**, 847–859.e7.
40. Poirier, G.G., de Murcia, G., Jongstra-Bilen, J., Niedergang, C., and Mandel, P. (1982). Poly(ADP-ribosylation) of polynucleosomes causes relaxation of chromatin structure. *Proc. Natl. Acad. Sci. USA* **79**, 3423–3427.
41. Strickfaden, H., McDonald, D., Kruhlak, M.J., Haince, J.F., Th'ng, J.P.H., Rouleau, R., Ishibashi, T., Corry, G.N., Ausio, J., Underhill, D.A., et al. (2016). Poly(ADP-ribosylation)-dependent transient chromatin decondensation and histone displacement following laser microirradiation. *J. Biol. Chem.* **291**, 1789–1802.
42. Tulin, A., and Spradling, A. (2003). Chromatin loosening by poly(ADP-ribose) polymerase (PARP) at *Drosophila* puff loci. *Science* **299**, 560–562.
43. Kim, M.Y., Mauro, S., Gévy, N., Lis, J.T., and Kraus, W.L. (2004). NAD⁺-dependent modulation of chromatin structure and transcription by nucleosome binding properties of PARP-1. *Cell* **119**, 803–814.
44. Pinnola, A., Naumova, N., Shah, M., and Tulin, A.V. (2007). Nucleosomal core histones mediate dynamic regulation of poly(ADP-ribose) polymerase 1 protein binding to chromatin and induction of its enzymatic activity. *J. Biol. Chem.* **282**, 32511–32519.
45. Wacker, D.A., Ruhl, D.D., Balagamwala, E.H., Hope, K.M., Zhang, T., and Kraus, W.L. (2007). The DNA binding and catalytic domains of poly(ADP-ribose) polymerase 1 cooperate in the regulation of chromatin structure and transcription. *Mol. Cell. Biol.* **27**, 7475–7485.
46. Altmeyer, M., Neelsen, K.J., Teloni, F., Pozdnyakova, I., Pellegrino, S., Gröfte, M., Rask, M.D., Streicher, W., Jungmichel, S., Nielsen, M.L., et al. (2015). Liquid demixing of intrinsically disordered proteins is seeded by poly(ADP-ribose). *Nat. Commun.* **6**, 8088.
47. Patel, A., Lee, H.O., Jawerth, L., Maharana, S., Jahnel, M., Hein, M.Y., Stoyanov, S., Mahamid, J., Saha, S., Franzmann, T.M., et al. (2015). A liquid-to-solid phase transition of the ALS protein FUS accelerated by disease mutation. *Cell* **162**, 1066–1077.
48. McGurk, L., Gomes, E., Guo, L., Mojsilovic-Petrovic, J., Tran, V., Kalb, R.G., Shorter, J., and Bonini, N.M. (2018). Poly(ADP-ribose) prevents pathological phase separation of TDP-43 by promoting liquid demixing and stress granule localization. *Mol. Cell* **71**, 703–717.e9.
49. Singatulina, A.S., Hamon, L., Sukhanova, M.V., Desforges, B., Joshi, V., Bouhss, A., Lavrik, O.I., and Pastré, D. (2019). PARP-1 activation directs FUS to DNA damage sites to form PARG-reversible compartments enriched in damaged DNA. *Cell Rep.* **27**, 1809–1821.e5.
50. Lyon, A.S., Peeples, W.B., and Rosen, M.K. (2021). A framework for understanding the functions of biomolecular condensates across scales. *Nat. Rev. Mol. Cell Biol.* **22**, 215–235.
51. Tibble, R.W., Depaix, A., Kowalska, J., Jemielity, J., and Gross, J.D. (2021). Biomolecular condensates amplify mRNA decapping by biasing enzyme conformation. *Nat. Chem. Biol.* **17**, 615–623.
52. Peeples, W., and Rosen, M.K. (2021). Mechanistic dissection of increased enzymatic rate in a phase-separated compartment. *Nat. Chem. Biol.* **17**, 693–702.
53. Pessina, F., Giavazzi, F., Yin, Y., Gioia, U., Vitelli, V., Galbiati, A., Barozzi, S., Garre, M., Oldani, A., Flaus, A., et al. (2019). Functional transcription promoters at DNA double-strand breaks mediate RNA-driven phase separation of damage-response factors. *Nat. Cell Biol.* **21**, 1286–1299.
54. Oshidari, R., Huang, R., Medghalchi, M., Tse, E.Y.W., Ashgriz, N., Lee, H.O., Wyatt, H., and Mekhail, K. (2020). DNA repair by Rad52 liquid droplets. *Nat. Commun.* **11**, 695.
55. Wang, Y.L., Zhao, W.W., Bai, S.M., Feng, L.L., Bie, S.Y., Gong, L., Wang, F., Wei, M.B., Feng, W.X., Pang, X.L., et al. (2022). MRNIP condensates promote DNA double-strand break sensing and end resection. *Nat. Commun.* **13**, 2638.
56. Kilic, S., Lezaja, A., Gatti, M., Bianco, E., Michelena, J., Imhof, R., and Altmeyer, M. (2019). Phase separation of 53BP1 determines liquid-like behavior of DNA repair compartments. *EMBO J.* **38**, e101379.
57. Leung, A.K.L. (2020). Poly(ADP-ribose): a dynamic trigger for biomolecular condensate formation. *Trends Cell Biol.* **30**, 370–383.
58. Smith, R., Zentout, S., Rother, M., Bigot, N., Chapuis, C., Mihut, A., Zobel, F.F., Ahel, I., van Attikum, H., Timinszky, G., et al. (2023). HPF1-dependent histone ADP-ribosylation triggers chromatin relaxation to promote the recruitment of repair factors at sites of DNA damage. *Nat. Struct. Mol. Biol.* **30**, 678–691.
59. Aubin, R.J., Fréchette, A., de Murcia, G., Mandel, P., Lord, A., Grondin, G., and Poirier, G.G. (1983). Correlation between endogenous nucleosomal hyper(ADP-ribosylation) of histone H1 and the induction of chromatin relaxation. *EMBO J.* **2**, 1685–1693.
60. de Murcia, G., Huletsky, A., Lamarre, D., Gaudreau, A., Pouyet, J., Daune, M., and Poirier, G.G. (1986). Modulation of chromatin superstructure induced by poly(ADP-ribose) synthesis and degradation. *J. Biol. Chem.* **261**, 7011–7017.

61. Smith, R., Lebeauupin, T., Juhász, S., Chapuis, C., D'Augustin, O., Dutertre, S., Burkovich, P., Biertümpfel, C., Timinszky, G., and Huet, S. (2019). Poly(ADP-ribose)-dependent chromatin unfolding facilitates the association of DNA-binding proteins with DNA at sites of damage. *Nucleic Acids Res.* **47**, 11250–11267.
62. Timinszky, G., Till, S., Hassa, P.O., Hothorn, M., Kustatscher, G., Nijmeijer, B., Colombelli, J., Altmeyer, M., Stelzer, E.H., Scheffzek, K., et al. (2009). A macrodomain-containing histone rearranges chromatin upon sensing PARP1 activation. *Nat. Struct. Mol. Biol.* **16**, 923–929.
63. Yang, G., Chen, Y., Wu, J., Chen, S.H., Liu, X., Singh, A.K., and Yu, X. (2020). Poly(ADP-ribosyl)ation mediates early phase histone eviction at DNA lesions. *Nucleic Acids Res.* **48**, 3001–3013.
64. Ahel, D., Horejsi, Z., Wiechens, N., Polo, S.E., Garcia-Wilson, E., Ahel, I., Flynn, H., Skehel, M., West, S.C., Jackson, S.P., et al. (2009). Poly(ADP-ribose)-dependent regulation of DNA repair by the chromatin remodeling enzyme ALC1. *Science* **325**, 1240–1243.
65. Lowary, P.T., and Widom, J. (1998). New DNA sequence rules for high affinity binding to histone octamer and sequence-directed nucleosome positioning. *J. Mol. Biol.* **276**, 19–42.
66. Yamanaka, H., Penning, C.A., Willis, E.H., Wasson, D.B., and Carson, D.A. (1988). Characterization of human poly(ADP-ribose) polymerase with autoantibodies. *J. Biol. Chem.* **263**, 3879–3883.
67. Huber, A., Bai, P., de Murcia, J.M., and de Murcia, G. (2004). PARP-1, PARP-2 and ATM in the DNA damage response: functional synergy in mouse development. *DNA Repair (Amst)* **3**, 1103–1108.
68. Huambachano, O., Herrera, F., Rancourt, A., and Satoh, M.S. (2011). Double-stranded DNA binding domain of poly(ADP-ribose) polymerase-1 and molecular insight into the regulation of its activity. *J. Biol. Chem.* **286**, 7149–7160.
69. Ménissier-de Murcia, J., Molinete, M., Gradwohl, G., Simonin, F., and de Murcia, G. (1989). Zinc-binding domain of poly(ADP-ribose)polymerase participates in the recognition of single strand breaks on DNA. *J. Mol. Biol.* **210**, 229–233.
70. Zhu, Z., Samuelson, J.C., Zhou, J., Dore, A., and Xu, S.Y. (2004). Engineering strand-specific DNA nicking enzymes from the type IIS restriction endonucleases BsaI, BsmBI, and BsmAI. *J. Mol. Biol.* **337**, 573–583.
71. Gibbs-Seymour, I., Fontana, P., Rack, J.G.M., and Ahel, I. (2016). HPF1/C4orf27 is a PARP-1-Interacting protein that regulates PARP-1 ADP-ribosylation activity. *Mol. Cell* **62**, 432–442.
72. Tan, E.S., Krukenberg, K.A., and Mitchison, T.J. (2012). Large-scale preparation and characterization of poly(ADP-ribose) and defined length polymers. *Anal. Biochem.* **428**, 126–136.
73. Rudolph, J., Roberts, G., Muthurajan, U.M., and Luger, K. (2021). HPF1 and nucleosomes mediate a dramatic switch in activity of PARP1 from polymerase to hydrolase. *eLife* **10**, e65773.
74. Tomkinson, A.E., Vijayakumar, S., Pascal, J.M., and Ellenberger, T. (2006). DNA ligases: structure, reaction mechanism, and function. *Chem. Rev.* **106**, 687–699.
75. Sallmyr, A., Rashid, I., Bhandari, S.K., Naila, T., and Tomkinson, A.E. (2020). Human DNA ligases in replication and repair. *DNA Repair (Amst)* **93**, 102908.
76. Cannan, W.J., Rashid, I., Tomkinson, A.E., Wallace, S.S., and Pederson, D.S. (2017). The human ligase IIIalpha-XRCC1 protein complex performs DNA nick repair after transient unwrapping of nucleosomal DNA. *J. Biol. Chem.* **292**, 5227–5238.
77. Chafin, D.R., Vitolo, J.M., Henricksen, L.A., Bambara, R.A., and Hayes, J.J. (2000). Human DNA ligase I efficiently seals nicks in nucleosomes. *EMBO J.* **19**, 5492–5501.
78. Caldecott, K.W., McKeown, C.K., Tucker, J.D., Ljungquist, S., and Thompson, L.H. (1994). An interaction between the mammalian DNA repair protein XRCC1 and DNA ligase III. *Mol. Cell. Biol.* **14**, 68–76.
79. Odell, I.D., Barbour, J.E., Murphy, D.L., Della-Maria, J.A., Sweasy, J.B., Tomkinson, A.E., Wallace, S.S., and Pederson, D.S. (2011). Nucleosome disruption by DNA ligase III-XRCC1 promotes efficient base excision repair. *Mol. Cell. Biol.* **31**, 4623–4632.
80. Min, W.K., and Wang, Z.Q. (2009). Poly (ADP-ribose) glycohydrolase (PARG) and its therapeutic potential. *Front. Biosci. (Landmark Ed.)* **14**, 1619–1626.
81. Martinez-Zamudio, R., and Ha, H.C. (2012). Histone ADP-ribosylation facilitates gene transcription by directly remodeling nucleosomes. *Mol. Cell. Biol.* **32**, 2490–2502.
82. Clark, D.J. (2010). Nucleosome positioning, nucleosome spacing and the nucleosome code. *J. Biomol. Struct. Dyn.* **27**, 781–793.
83. Ghoneim, M., Fuchs, H.A., and Musselman, C.A. (2021). Histone tail conformations: a fuzzy affair with DNA. *Trends Biochem. Sci.* **46**, 564–578.
84. Krüger, A., Bürkle, A., Hauser, K., and Mangerich, A. (2020). Real-time monitoring of PARP1-dependent PARylation by ATR-FTIR spectroscopy. *Nat. Commun.* **11**, 2174.
85. Leidecker, O., Bonfiglio, J.J., Colby, T., Zhang, Q., Atanassov, I., Zaja, R., Palazzo, L., Stockum, A., Ahel, I., and Matic, I. (2016). Serine is a new target residue for endogenous ADP-ribosylation on histones. *Nat. Chem. Biol.* **12**, 998–1000.
86. Palazzo, L., Leidecker, O., Prokhorova, E., Dauben, H., Matic, I., and Ahel, I. (2018). Serine is the major residue for ADP-ribosylation upon DNA damage. *eLife* **7**, e34334.
87. Tugarinov, V., Hwang, P.M., Ollerenshaw, J.E., and Kay, L.E. (2003). Cross-correlated relaxation enhanced ¹H-¹³C NMR spectroscopy of methyl groups in very high molecular weight proteins and protein complexes. *J. Am. Chem. Soc.* **125**, 10420–10428.
88. Rosenzweig, R., and Kay, L.E. (2014). Bringing dynamic molecular machines into focus by methyl-TROSY NMR. *Annu. Rev. Biochem.* **83**, 291–315.
89. Schütz, S., and Sprangers, R. (2020). Methyl TROSY spectroscopy: a versatile NMR approach to study challenging biological systems. *Prog. Nucl. Magn. Reson. Spectrosc.* **116**, 56–84.
90. Tugarinov, V., and Kay, L.E. (2004). An isotope labelling strategy for methyl TROSY spectroscopy. *J. Biomol. NMR* **28**, 165–172.
91. Davey, C.A., Sargent, D.F., Luger, K., Maeder, A.W., and Richmond, T.J. (2002). Solvent mediated interactions in the structure of the nucleosome core particle at 1.9 Å resolution. *J. Mol. Biol.* **319**, 1097–1113.
92. Böhm, L., and Crane-Robinson, C. (1984). Proteases as structural probes for chromatin: the domain structure of histones. *Biosci. Rep.* **4**, 365–386.
93. Abramov, G., Velyvis, A., Rennella, E., Wong, L.E., and Kay, L.E. (2020). A methyl-TROSY approach for NMR studies of high-molecular-weight DNA with application to the nucleosome core particle. *Proc. Natl. Acad. Sci. USA* **117**, 12836–12846.
94. Sanulli, S., Trnka, M.J., Dharmarajan, V., Tibble, R.W., Pascal, B.D., Burlingame, A.L., Griffin, P.R., Gross, J.D., and Narlikar, G.J. (2019). HP1 reshapes nucleosome core to promote phase separation of heterochromatin. *Nature* **575**, 390–394.
95. Karch, K.R., Coradin, M., Zandarashvili, L., Kan, Z.Y., Gerace, M., Englander, S.W., Black, B.E., and Garcia, B.A. (2018). Hydrogen-deuterium exchange coupled to top- and middle-down mass spectrometry reveals histone tail dynamics before and after nucleosome assembly. *Structure* **26**, 1651–1663.e3.
96. Schmitz, K.S. (1990). Polyelectrolyte solutions. In *Introduction to Dynamic Light Scattering by Macromolecules*, K.S. Schmitz, ed. (Academic Press, Inc.), pp. 205–259.
97. Moore, S.C., and Ausió, J. (1997). Major role of the histones H3-H4 in the folding of the chromatin fiber. *Biochem. Biophys. Res. Commun.* **230**, 136–139.
98. Bertin, A., Renouard, M., Pedersen, J.S., Livolant, F., and Durand, D. (2007). H3 and H4 histone tails play a central role in the interactions of recombinant NCPs. *Biophys. J.* **92**, 2633–2645.

99. Kan, P.Y., Caterino, T.L., and Hayes, J.J. (2009). The H4 tail domain participates in intra- and internucleosome interactions with protein and DNA during folding and oligomerization of nucleosome arrays. *Mol. Cell. Biol.* **29**, 538–546.
100. Dorigo, B., Schalch, T., Bystricky, K., and Richmond, T.J. (2003). Chromatin fiber folding: requirement for the histone H4 N-terminal tail. *J. Mol. Biol.* **327**, 85–96.
101. Altieri, A.S., Hinton, D.P., and Byrd, R.A. (1995). Association of biomolecular systems via pulsed field gradient NMR self-diffusion measurements. *J. Am. Chem. Soc.* **117**, 7566–7567.
102. Breslin, C., Hornyak, P., Ridley, A., Rulten, S.L., Hanzlikova, H., Oliver, A.W., and Caldecott, K.W. (2015). The XRCC1 phosphate-binding pocket binds poly (ADP-ribose) and is required for XRCC1 function. *Nucleic Acids Res.* **43**, 6934–6944.
103. El-Khamisy, S.F., Masutani, M., Suzuki, H., and Caldecott, K.W. (2003). A requirement for PARP-1 for the assembly or stability of XRCC1 nuclear foci at sites of oxidative DNA damage. *Nucleic Acids Res.* **31**, 5526–5533.
104. Leppard, J.B., Dong, Z., Mackey, Z.B., and Tomkinson, A.E. (2003). Physical and functional interaction between DNA ligase IIIalpha and poly(ADP-ribose) polymerase 1 in DNA single-strand break repair. *Mol. Cell. Biol.* **23**, 5919–5927.
105. Polo, L.M., Xu, Y., Hornyak, P., Garces, F., Zeng, Z., Hailstone, R., Matthews, S.J., Caldecott, K.W., Oliver, A.W., and Pearl, L.H. (2019). Efficient single-strand break repair requires binding to both poly(ADP-ribose) and DNA by the central BRCT domain of XRCC1. *Cell Rep.* **26**, 573–581.e5.
106. Langelier, M.F., Planck, J.L., Roy, S., and Pascal, J.M. (2012). Structural basis for DNA damage-dependent poly(ADP-ribosylation) by human PARP-1. *Science* **336**, 728–732.
107. Dasovich, M., Beckett, M.Q., Bailey, S., Ong, S.E., Greenberg, M.M., and Leung, A.K.L. (2021). Identifying poly(ADP-ribose)-binding proteins with photoaffinity-based proteomics. *J. Am. Chem. Soc.* **143**, 3037–3042.
108. Caldecott, K.W., Aoufouchi, S., Johnson, P., and Shall, S. (1996). XRCC1 polypeptide interacts with DNA polymerase β and possibly poly (ADP-ribose) polymerase, and DNA ligase III is a novel molecular 'nick-sensor' in vitro. *Nucleic Acids Res.* **24**, 4387–4394.
109. Banani, S.F., Lee, H.O., Hyman, A.A., and Rosen, M.K. (2017). Biomolecular condensates: organizers of cellular biochemistry. *Nat. Rev. Mol. Cell Biol.* **18**, 285–298.
110. Caldecott, K.W. (2019). XRCC1 protein; form and function. *DNA Repair (Amst)* **81**, 102664.
111. Loizou, J.I., El-Khamisy, S.F., Zlatanou, A., Moore, D.J., Chan, D.W., Qin, J., Sarno, S., Meggio, F., Pinna, L.A., and Caldecott, K.W. (2004). The protein kinase CK2 facilitates repair of chromosomal DNA single-strand breaks. *Cell* **117**, 17–28.
112. Marintchev, A., Robertson, A., Dimitriadis, E.K., Prasad, R., Wilson, S.H., and Mullen, G.P. (2000). Domain specific interaction in the XRCC1-DNA polymerase beta complex. *Nucleic Acids Res.* **28**, 2049–2059.
113. Hayashi, K., Tanaka, M., Shimada, T., Miwa, M., and Sugimura, T. (1983). Size and shape of poly(ADP-ribose): examination by gel filtration, gel electrophoresis and electron microscopy. *Biochem. Biophys. Res. Commun.* **112**, 102–107.
114. Alvarez-Gonzalez, R., and Jacobson, M.K. (1987). Characterization of polymers of adenosine diphosphate ribose generated in vitro and in vivo. *Biochemistry* **26**, 3218–3224.
115. Miwa, M., Saikawa, N., Yamaizumi, Z., Nishimura, S., and Sugimura, T. (1979). Structure of poly(adenosine diphosphate ribose): identification of 2'-[1''-ribosyl-2''-(or 3'')-(1'''-ribosyl)]adenosine-5',5'',5'''-tris(phosphate) as a branch linkage. *Proc Natl Acad Sci USA* **76**, 595–599.
116. Ikebe, J., Sakuraba, S., and Kono, H. (2016). H3 histone tail conformation within the nucleosome and the impact of K14 acetylation studied using enhanced sampling simulation. *PLoS Comput. Biol.* **12**, e1004788.
117. Stützer, A., Liokatis, S., Kiesel, A., Schwarzer, D., Sprangers, R., Söding, J., Selenko, P., and Fischle, W. (2016). Modulations of DNA contacts by linker histones and post-translational modifications determine the mobility and modifiability of nucleosomal H3 tails. *Mol. Cell* **61**, 247–259.
118. North, J.A., Javai, S., Ferdinand, M.B., Chatterjee, N., Picking, J.W., Shoffner, M., Nakkula, R.J., Bartholomew, B., Ottesen, J.J., Fishel, R., et al. (2011). Phosphorylation of histone H3(T118) alters nucleosome dynamics and remodeling. *Nucleic Acids Res.* **39**, 6465–6474.
119. Furukawa, A., Wakamori, M., Arimura, Y., Ohtomo, H., Tsunaka, Y., Kurumizaka, H., Umehara, T., and Nishimura, Y. (2020). Acetylated histone H4 tail enhances histone H3 tail acetylation by altering their mutual dynamics in the nucleosome. *Proc. Natl. Acad. Sci. USA* **117**, 19661–19663.
120. Nurse, N.P., Jimenez-Useche, I., Smith, I.T., and Yuan, C. (2013). Clipping of flexible tails of histones H3 and H4 affects the structure and dynamics of the nucleosome. *Biophys. J.* **104**, 1081–1088.
121. Rhine, K., Dasovich, M., Yoniles, J., Badiie, M., Skanchy, S., Ganser, L.R., Ge, Y., Fare, C.M., Shorter, J., Leung, A.K.L., et al. (2022). Poly(ADP-ribose) drives condensation of FUS via a transient interaction. *Mol. Cell* **82**, 969–985.e11.
122. Sukhanova, M.V., Singatulina, A.S., Pastré, D., and Lavrik, O.I. (2020). Fused in sarcoma (FUS) in DNA repair: tango with poly(ADP-ribose) polymerase 1 and compartmentalisation of damaged DNA. *Int. J. Mol. Sci.* **21**, 7020.
123. Mortusewicz, O., Rothbauer, U., Cardoso, M.C., and Leonhardt, H. (2006). Differential recruitment of DNA ligase I and III to DNA repair sites. *Nucleic Acids Res.* **34**, 3523–3532.
124. Shin, Y., Chang, Y.C., Lee, D.S.W., Berry, J., Sanders, D.W., Ronceray, P., Wingreen, N.S., Haataja, M., and Brangwynne, C.P. (2018). Liquid nuclear condensates mechanically sense and restructure the genome. *Cell* **175**, 1481–1491.e13.
125. Larson, A.G., Elnatan, D., Keenen, M.M., Trnka, M.J., Johnston, J.B., Burlingame, A.L., Agard, D.A., Redding, S., and Narlikar, G.J. (2017). Liquid droplet formation by HP1 α suggests a role for phase separation in heterochromatin. *Nature* **547**, 236–240.
126. Wang, L., Gao, Y., Zheng, X., Liu, C., Dong, S., Li, R., Zhang, G., Wei, Y., Qu, H., Li, Y., et al. (2019). Histone modifications regulate chromatin compartmentalization by contributing to a phase separation mechanism. *Mol. Cell* **76**, 646–659.e6.
127. Liszczak, G., Diehl, K.L., Dann, G.P., and Muir, T.W. (2018). Acetylation blocks DNA damage-induced chromatin ADP-ribosylation. *Nat. Chem. Biol.* **14**, 837–840.
128. Weber, A.R., Krawczyk, C., Robertson, A.B., Kuśnierczyk, A., Vågbo, C.B., Schuermann, D., Klungland, A., and Schär, P. (2016). Biochemical reconstruction of TET1-TDG-BER-dependent active DNA demethylation reveals a highly coordinated mechanism. *Nat. Commun.* **7**, 10806.
129. Kennedy, M.J., Hughes, R.M., Peteya, L.A., Schwartz, J.W., Ehlers, M.D., and Tucker, C.L. (2010). Rapid blue-light-mediated induction of protein interactions in living cells. *Nat. Methods* **7**, 973–975.
130. Schindelin, J., Arganda-Carreras, I., Frise, E., Kaynig, V., Longair, M., Pietzsch, T., Preibisch, S., Rueden, C., Saalfeld, S., Schmid, B., et al. (2012). Fiji: an open-source platform for biological-image analysis. *Nat. Methods* **9**, 676–682.
131. Pettersen, E.F., Goddard, T.D., Huang, C.C., Meng, E.C., Couch, G.S., Croll, T.I., Morris, J.H., and Ferrin, T.E. (2021). UCSF ChimeraX: structure visualization for researchers, educators, and developers. *Protein Sci.* **30**, 70–82.
132. Punjani, A., Rubinstein, J.L., Fleet, D.J., and Brubaker, M.A. (2017). cryoSPARC: algorithms for rapid unsupervised cryo-EM structure determination. *Nat. Methods* **14**, 290–296.
133. Kato, H., van Ingen, H., Zhou, B.R., Feng, H., Bustin, M., Kay, L.E., and Bai, Y. (2011). Architecture of the high mobility group nucleosomal

- protein 2-nucleosome complex as revealed by methyl-based NMR. *Proc. Natl. Acad. Sci. USA* **108**, 12283–12288.
134. Morrison, E.A., Bowerman, S., Sylvers, K.L., Wereszczynski, J., and Musselman, C.A. (2018). The conformation of the histone H3 tail inhibits association of the BPTF PHD finger with the nucleosome. *eLife* **7**, e31481.
135. Chang, A.Y., Chau, V.W.Y., Landas, J.A., and Pang, Y. (2017). Preparation of calcium competent *Escherichia coli* and heat-shock transformation. *JEMI Methods* **1**, 22–25.
136. Kay, L.E., Keifer, P., and Saarinen, T. (1992). Pure absorption gradient enhanced heteronuclear single quantum correlation spectroscopy with improved sensitivity. *J. Am. Chem. Soc.* **114**, 10663–10665.
137. Sklenar, V., Piotto, M., Leppik, R., and Saudek, V. (1993). Gradient-tailored water suppression for 1H-15N HSQC experiments optimized to retain full sensitivity. *J. Magn. Reson.* **102**, 241–245.
138. Hansen, D.F., Feng, H., Zhou, Z., Bai, Y., and Kay, L.E. (2009). Selective characterization of microsecond motions in proteins by NMR relaxation. *J. Am. Chem. Soc.* **131**, 16257–16265.
139. Hansen, D.F., Yang, D., Feng, H., Zhou, Z., Wiesner, S., Bai, Y., and Kay, L.E. (2007). An exchange-free measure of 15N transverse relaxation: an NMR spectroscopy application to the study of a folding intermediate with pervasive chemical exchange. *J. Am. Chem. Soc.* **129**, 11468–11479.
140. Choy, W.Y., Mulder, F.A., Crowhurst, K.A., Muhandiram, D.R., Millett, I.S., Doniach, S., Forman-Kay, J.D., and Kay, L.E. (2002). Distribution of molecular size within an unfolded state ensemble using small-angle X-ray scattering and pulse field gradient NMR techniques. *J. Mol. Biol.* **316**, 101–112.
141. Hwang, T.L., and Shaka, A.J. (1995). Water suppression that works. Excitation sculpting using arbitrary wave-forms and pulsed-field gradients. *J. Magn. Reson. A* **112**, 275–279.
142. Glasoe, P.K., and Long, F.A. (1960). Use of glass electrodes to measure acidities in deuterium oxide 1,2. *J. Phys. Chem.* **64**, 188–190.
143. Mikkelsen, K., and Nielsen, S.O. (1960). Acidity measurements with the glass electrode in H₂O-D₂O mixtures. *J. Phys. Chem.* **64**, 632–637.
144. Hamuro, Y., and Coales, S.J. (2018). Optimization of feasibility stage for hydrogen/deuterium exchange mass spectrometry. *J. Am. Soc. Mass Spectrom.* **29**, 623–629.
145. Yang, M., Hoepfner, M., Rey, M., Kadek, A., Man, P., and Schriemer, D.C. (2015). Recombinant Nepenthesin II for hydrogen/deuterium exchange mass spectrometry. *Anal. Chem.* **87**, 6681–6687.
146. Majumdar, R., Manikwar, P., Hickey, J.M., Arora, J., Middaugh, C.R., Volkin, D.B., and Weis, D.D. (2012). Minimizing carry-over in an online pepsin digestion system used for the H/D exchange mass spectrometric analysis of an IgG1 monoclonal antibody. *J. Am. Soc. Mass Spectrom.* **23**, 2140–2148.
147. Vahidi, S., Bi, Y., Dunn, S.D., and Konermann, L. (2016). Load-dependent destabilization of the gamma-rotor shaft in FOF1 ATP synthase revealed by hydrogen/deuterium-exchange mass spectrometry. *Proc. Natl. Acad. Sci. USA* **113**, 2412–2417.
148. Sørensen, L., and Salbo, R. (2018). Optimized workflow for selecting peptides for HDX-MS data analyses. *J. Am. Soc. Mass Spectrom.* **29**, 2278–2281.
149. Guttman, M., Wales, T.E., Whittington, D., Engen, J.R., Brown, J.M., and Lee, K.K. (2016). Tuning a high transmission ion guide to prevent gas-phase proton exchange during H/D exchange MS analysis. *J. Am. Soc. Mass Spectrom.* **27**, 662–668.
150. Houde, D., Berkowitz, S.A., and Engen, J.R. (2011). The utility of hydrogen/deuterium exchange mass spectrometry in biopharmaceutical comparability studies. *J. Pharm. Sci.* **100**, 2071–2086.
151. Engen, J.R., and Wales, T.E. (2015). Analytical aspects of hydrogen exchange mass spectrometry. *Annu. Rev. Anal. Chem. (Palo Alto, Calif)* **8**, 127–148.
152. Du, S., Alvarado, J.J., Wales, T.E., Moroco, J.A., Engen, J.R., and Smithgall, T.E. (2022). ATP-site inhibitors induce unique conformations of the acute myeloid leukemia-associated Src-family kinase, Fgr. *Structure* **30**, 1508–1517.e3.
153. Marr, C.R., Benlekhir, S., and Rubinstein, J.L. (2014). Fabrication of carbon films with ~500nm holes for cryo-EM with a direct detector device. *J. Struct. Biol.* **185**, 42–47.
154. Johnson, C.S., Jr. (1993). Effects of chemical exchange in diffusion-ordered 2D NMR spectra. *J. Magn. Reson. A* **102**, 214–218.
155. Schneider, C.A., Rasband, W.S., and Eliceiri, K.W. (2012). NIH Image to ImageJ: 25 years of image analysis. *Nat. Methods* **9**, 671–675.

STAR★METHODS

KEY RESOURCES TABLE

REAGENT or RESOURCE	SOURCE	IDENTIFIER
Bacterial and virus strains		
BL21 CodonPlus Competent Cells: <i>Escherichia coli</i> BL21 (DE3) RIPL strain	Agilent	Cat. No. 230280
OverExpress C41(DE3) Chemically Competent Cells	Sigma Aldrich	Cat. No. CMC0017
Chemicals, peptides, and recombinant proteins		
Isopropyl- β -1-thiogalactopyranoside (IPTG)	BioBasic Canada	Cat. No. IB0168
Ammonium- ^{15}N chloride	Sigma-Aldrich	Cat. No. 299251
Deuterium oxide (D_2O)	Cambridge Isotopes Laboratories	Cat. No. DLM-4DR-PK
D-glucose, U- $^{13}\text{C}_6$	Cambridge Isotopes Laboratories	Cat. No. CLM-1396
D-glucose, U- $^{13}\text{C}_6$, 1,2,3,4,5,6,6- $^2\text{H}_7$	Cambridge Isotopes Laboratories	Cat. No. CDLM-3813
α -ketobutyric acid, methyl- ^{13}C , 3,3- ^2H sodium salt	Cambridge Isotopes Laboratories	Cat. No. CDLM-7318
α -ketoisovaleric acid, 3-methyl- ^{13}C , 1,4,4,4- ^2H sodium salt	Cambridge Isotopes Laboratories	Cat. No. CDLM-7317
Nicotinamide adenine dinucleotide disodium salt	Sigma Aldrich	Cat. No. 6754
Adenosine 5'-diphosphoribose sodium salt	Sigma Aldrich	Cat. No. A0752
Adenosine 5'-triphosphate disodium salt	Sigma Aldrich	Cat. No. A2383
EcoRV	New England Biolabs	Cat. No. R0195
Micrococcal nuclease	New England Biolabs	Cat. No. 0247S
Trypsin-Ultra™, Mass spectrometry grade	New England Biolabs	Cat. No. 8101S
T4 DNA ligase	New England Biolabs	Cat. No. M0202
Alexa Fluor 488- C_5 -maleimide	Thermo Fisher Scientific	Cat. No. A10254
Biotin-maleimide (N-biotinoyl-N'-(6-maleimidohexanoyl)hydrazide	Sigma Aldrich	Cat. No. B1267
SafeView	Applied Biological Materials	Cat. No. G108
SYBR Gold	Invitrogen	Cat. No. S33102
Novex™ TBE-urea gels, 15%	Invitrogen	Cat. No. EC6885BOX
Bolt™ Bis-Tris Plus Mini Protein Gels, 4-12%, 1.0mm, WedgeWell™ format	Invitrogen	Cat. No. NW04120BOX
Ni Sepharose 6 Fast Flow, 100mL	Cytiva	Cat. No. 17531802
Ficoll PM400	Sigma-Aldrich	Cat. No. F4375
Critical commercial assays		
QIAGEN Plasmid Giga Kit	QIAGEN	Cat. No. 12191
QIAGEN Plasmid Mini Kit	QIAGEN	Cat. No. 12123
Gibson Assembly™ Master Mix	New England Biolabs	Cat. No. E2611L
KAPA HiFi HotStart ReadyMix	Roche	Cat. No. 7958935001
GenepHlow™ Gel/PCR Kit	Geneaid	Cat. No. DFH100
Deposited data		
Cryo-EM map of the unmodified nucleosome core particle in 100 mM KCl with local resolution values	This study	Accession no.: EMD-41182
Cryo-EM map of the PARylated nucleosome core particle in 100 mM KCl with local resolution values	This study	Accession no.: EMD-41183
Cryo-EM map of the unmodified nucleosome core particle in 5 mM KCl with local resolution values	This study	Accession no.: EMD-41184
Cryo-EM map of the PARylated nucleosome core particle in 5 mM KCl with local resolution values	This study	Accession no.: EMD-41178
Unprocessed Image Files	This study	https://doi.org/10.17632/3j5dydhxp.1

(Continued on next page)

Continued

REAGENT or RESOURCE	SOURCE	IDENTIFIER
Oligonucleotides		
601DNA 31mer sequence with 5'-phosphate and 3'-Alexa Fluor 647: P-AGGCACGTGTCAGATATATACATCCTGTGAT-AF647	Integrated DNA Technologies	Custom Order
Recombinant DNA		
pUC19 601 DNA	Muir Lab	N/A
pET21b Histone H2A (<i>D. melanogaster</i>)	Muir Lab	N/A
pET28 Histone H2B TEV-His ₆ (<i>D. melanogaster</i>)	Muir Lab	N/A
pET21b Histone H3 (<i>D. melanogaster</i>)	Muir Lab	N/A
pET21b Histone H4 (<i>D. melanogaster</i>)	Muir Lab	N/A
pET SUMO mCherry-PARP1 (<i>H. sapiens</i>)	This study	N/A
pET SUMO HPF1 (<i>H. sapiens</i>)	This study	N/A
pET SUMO LIG3 α (<i>H. sapiens</i>)	This study	N/A
pET SUMO LIG3 Δ BRCT (<i>H. sapiens</i>)	This study	N/A
pET SUMO XRCC1 (<i>H. sapiens</i>)	This study	N/A
pET SUMO APLF (<i>H. sapiens</i>)	This study	N/A
pET SUMO APTX (<i>H. sapiens</i>)	This study	N/A
pET SUMO PNKP (<i>H. sapiens</i>)	This study	N/A
pET SUMO POLB (<i>H. sapiens</i>)	This study	N/A
pET SUMO PARG (<i>H. sapiens</i>)	This study	N/A
pET SUMO CSNK2A1 (<i>H. sapiens</i>)	This study	N/A
pET SUMO CSNK2B (<i>H. sapiens</i>)	This study	N/A
pET21a mAP-His ₆	Genscript	Custom Order
pCOLA Duet-1 <i>nt.bsmAI R221D bsmAIM</i>	Genscript	Custom Order
pET30 HPF1-His-Sumo-Flag (<i>H. sapiens</i>)	Muir Lab ¹²⁷	Addgene Plasmid No. 111577
pGEX4T LIG3	Schär Lab ¹²⁸	Addgene Plasmid No. 81055
pCRY2PHR-mCherryN1	Tucker Lab ¹²⁹	Addgene Plasmid No. 26866
pCMV-SPORT6 PARP1	Mammalian Gene Collection	cDNA Clone MGC: 40266
pDONR223 LIG3	Mammalian Gene Collection	cDNA Clone MGC: 75006
Software and algorithms		
ImageJ	Schindelin et al. ¹³⁰	https://imagej.nih.gov/ij/
Fiji	Schindelin et al. ¹³⁰	https://imagej.net/Fiji/Downloads
UCSF Chimera X v1.5	Pettersen et al. ¹³¹	https://www.cgl.ucsf.edu/chimerax/download.html
CryoSPARC v4	Punjani et al. ¹³²	https://cryosparc.com/download
Modeling of Diffusion Data (NCP Stacking Analysis Code)	This study; Kim et al. ⁹	https://doi.org/10.5281/zenodo.10324511
Peakipy	Dr. Jacob Brady	https://pypi.org/project/peakipy/1.1.3/
Other		
Superdex 200 Increase 10/300 GL	Cytiva	Cat. No. 28992944
Superdex 75 Increase 10/300 GL	Cytiva	Cat. No. 29148721
HiLoad Superdex 75 pg 16/600	Cytiva	Cat. No. 28989333
HiLoad Superdex 200 pg 16/600	Cytiva	Cat. No. 28989335
HiLoad Superdex 200 pg 26/600	Cytiva	Cat. No. 28989336
HiTrap DEAE Sepharose 5mL FF	Cytiva	Cat. No. 17505501
HiTrap SP Sepharose 5mL FF	Cytiva	Cat. No. 17505401
HiTrap Desalting 5mL	Cytiva	Cat. No. 29048604
HiPrep Desalting 26/10	Cytiva	Cat. No. 17508701
MonoS FPLC HR 5/5	Pharmacia	N/A

(Continued on next page)

Continued

REAGENT or RESOURCE	SOURCE	IDENTIFIER
MonoQ FPLC HR 5/5	Pharmacia	N/A
Nepenthesin-2 Column (2.1mm internal diameter, 20mm length)	AffiPro	Cat. No. AP-PC-004
Low Volume 384-Well Black Polystyrene/Clear Bottom Microplate	Corning	Cat. No. 3540
Cell Imaging Plate, 96-well, glass bottom	Eppendorf	Cat. No. 0030 471.030
Siliconized Glass Circle Cover Slips, 22mm	Hampton Research	Cat. No. HR3-231
Glass Bottom Culture Dish, 35mm dish, 14mm micro-well, no. 1.0 coverglass	MatTek Life Sciences	Cat. No. P35G-1.0-14-C
Symmetrical MICRO NMR Tubes for D ₂ O, 5mm, optimized for Bruker	Shigemi Co., Ltd.	Cat. No. BMS-005B

RESOURCE AVAILABILITY

Lead contact

Further information and inquiries about reagents should be directed to the lead contact, Lewis E. Kay (lewis.kay@utoronto.ca).

Materials availability

Plasmids generated in this study (as indicated in the [key resources table](#)) are deposited in Addgene and are available for purchase through this distributor, or by contacting one of the lead authors.

Data and code availability

- Assignments of NMR spectra are available in the published literature.^{9,133,134} Cryo-electron microscopy data are deposited in the Electron Microscopy Data Bank with accession codes listed in the [key resources table](#). All other data, including microscopy datafiles, gel images from enzyme assays, and DLS measurements are available upon request to the [lead contact](#). Additionally, unprocessed image files, including gel images and micrographs, can be found on Mendeley Data (DOI listed in the [key resources table](#)).
- Original code for analyzing NCP self-association from diffusion data is available as of the date of publication (DOI listed in the [key resources table](#)). peakipy is a Python package developed by Dr. Jacob Brady and is publicly available on github (<https://github.com/j-brady/peakipy>) or the Python Package Index, PyPI (<https://pypi.org/project/peakipy/1.1.3/>).
- Any additional information required to reanalyze the data reported in this paper is available from the [lead contact](#) upon request.

EXPERIMENTAL MODEL AND STUDY PARTICIPANT DETAILS

Bacterial strains

The *Escherichia coli* DH10B strain (ThermoFisher Scientific) was used for cloning and manipulation of plasmid constructs for recombinant protein expression. *E. coli* strains C41(DE3) (Sigma Aldrich) and BL21-CodonPlus (DE3)-RIPL (Invitrogen) were used for preparative-scale recombinant protein and 601-DNA expression and purification.

METHOD DETAILS

Cloning of bacterial expression plasmids *XRCC1*, *LIG3*, and DNA repair proteins

Plasmids harbouring cDNA clones of *H. sapiens* *XRCC1* and *PARG* were acquired from the Mammalian Gene Collection (MGC), made available through the SickKids Proteomics, Analytics, Robotics and Chemical Biology (SPARC) Centre. MGC cDNA clones of *H. sapiens* *APLF*, *APTX*, *PNKP* and *POLB* were purchased from Dharmacon. Plasmids encoding the alpha-splice isoform of *H. sapiens* *LIG3* (i.e., including the C-terminal BRCT domain), and Flag-, His₆-SUMO-tagged *HPF1* were obtained from Addgene (pGEX4T-hLIG3 and pET30 HPF1-His-SUMO-Flag, respectively; see [key resources table](#)).^{127,128} The open reading frame (ORF) of each gene was amplified from cDNA by polymerase chain reaction (PCR) and inserted in frame with a N-terminal hexahistidine (His₆)-SUMO tag in a linearized Champion pET SUMO (ThermoFisher Scientific) vector via Gibson assembly (New England Biolabs). Sequences encoding the full-length protein were used in every case, unless otherwise specified. PCR was performed with Kapa HiFi HotStart Readymix (Roche) using custom primers with calculated annealing temperatures of ~60°C. The purity of the PCR products was assessed using agarose gel electrophoresis, and in cases where PCR-amplified inserts were insufficiently pure for Gibson

assembly, an intermediate agarose gel extraction and purification step using a Geneaid gel extraction and PCR cleanup kit was included. The fidelity of each construct was validated by DNA sequencing using primers complementary to the T7 promoter or termination sequences.

For the LIG3 Δ BRCT truncation mutant, PCR primers were designed to amplify the DNA segment encoding residues 1-779 of LIG3 in the final translated protein. This fragment was inserted into pET SUMO via Gibson assembly as described above.

mCherry-tagged PARP1

A plasmid harbouring a cDNA clone of *H. sapiens* PARP1 was purchased from the MGC via SPARC. The ORF corresponding to the full-length protein (residues 1-1014) was amplified by PCR and inserted via Gibson assembly in frame with an ORF encoding mCherry (originally amplified from pCRY2PHR-mCherryN1 obtained from Addgene; see [key resources table](#))¹²⁹ and a N-terminal His₆-SUMO tag in a linearized Champion pET SUMO (ThermoFisher Scientific) vector. A short linker sequence, encoding “Ser-Gly-Pro-Ser” in the expressed fusion protein, was included in the overlapping segments of the mCherry and PARP1 DNA fragments. Successful assembly of this construct was validated by DNA sequencing using T7 promoter and T7 terminator primers along with a custom reverse primer that anneals ~300 bp from the 5' end of PARP1 (to check the linker and junction between mCherry and PARP1).

Metagenome-derived alkaline phosphatase

The metagenome-derived alkaline phosphatase (mAP) ORF sequence derived from Genbank (accession code GQ250428) was synthesized by Genscript with custom codon optimization for expression in *E. coli*. The synthetic ORF was subcloned into a pET21a plasmid (also by Genscript) in frame with a N-terminal His₆ tag. The final construct was validated by DNA sequencing using the T7 terminator primer.

Nt.BsmAI

Nt.BsmAI is a mutant of the restriction endonuclease, BsmAI, containing a point mutation (R221D) that favors the formation of single-strand over double-strand cuts. Gene synthesis (with codon optimization for expression in *E. coli*) and subcloning were performed by Genscript. DNA fragments encoding His₆-SUMO-Nt.BsmAI and the DNA methyltransferase bsmAIM were inserted into a pCOLA Duet vector. Coexpression of the methyltransferase was necessary to mitigate toxicity caused by Nt.BsmAI expression.

Casein kinase 2

DNA fragments encoding the ORFs for casein kinase 2 α and β subunits (i.e., full-length human CSNK2A1 and CSNK2B), codon optimized for expression in *E. coli*, were ordered from Genscript. The ORFs were amplified by PCR, gel purified, and inserted into linearized pET SUMO vectors in frame with a N-terminal His₆-SUMO tag via Gibson assembly. Cloning fidelity was validated by DNA sequencing using T7 and T7 terminator primers.

Recombinant protein and DNA purification

Expression and initial purification of mCherry-tagged PARP1, XRCC1, LIG3, PARG, HPF1, casein kinase 2 and other DNA repair proteins in *E. coli*

pET SUMO constructs encoding full-length mCherry-PARP1, XRCC1, PARG, HPF1, APLF, APTX, PNKP, POLB, and casein kinase 2 (α and β subunits) were overexpressed in *E. coli* under identical conditions, except where indicated. Each pET SUMO vector containing the construct of interest was transformed into chemically-competent *E. coli* BL21-CodonPlus (DE3)-RIPL prepared in house using the calcium chloride method.¹³⁵ Successful transformants were selected on lysogeny broth (LB)-agar plates containing kanamycin (50 μ g mL⁻¹). For LIG3 and LIG3 Δ BRCT constructs, chemically-competent *E. coli* BL21 (DE3) C41 cells were transformed with the pRIPL plasmid and selected on LB-agar containing chloramphenicol (34 μ g mL⁻¹). Successful transformants were then used to prepare chemically-competent *E. coli* BL21 (DE3) C41 RIPL cells which were used for expression of pET SUMO LIG3 and LIG3 Δ BRCT. Successful transformants containing both the pRIPL and pET SUMO vectors were selected on LB-agar containing chloramphenicol (34 μ g mL⁻¹) in addition to kanamycin.

Bacterial colonies obtained following transformation and selection were used to inoculate ~60 mL LB liquid cultures which were then incubated overnight at 37 °C, shaking at 250 rpm. The next morning, these cultures were used to inoculate 4 × 1 L LB cultures in 2.5 L Fernbach flasks. Smaller culture volumes (i.e., 2 × 1 L LB cultures) were used for APLF, HPF1, LIG3 Δ BRCT and POLB due to their high expression levels. 1 L cultures were incubated at 37 °C with 250 rpm shaking until an optical density (OD₆₀₀) of 0.9-1.1 was measured, at which point isopropyl- β -D-thiogalactopyranoside (IPTG) was added to a final concentration of 0.5 mM. For mChPARP1, 0.1 mM ZnSO₄ was also added at this time. Cultures were then allowed to incubate overnight (~18 h) at 16 °C with 250 rpm shaking. Cells were harvested by centrifugation and resuspended in lysis buffer: 25 mM Tris, 250 mM NaCl, 10% v/v glycerol, 2.5 mM 2-mercaptoethanol, 25 mM imidazole, pH 7.5. Small amounts of bovine pancreatic DNase I and hen egg-white lysozyme were added to hydrolyze DNA and aid in lysis, respectively. A “cComplete” protease inhibitor cocktail (Millipore Sigma) was added in a ratio of 1 tablet per 100 mL of suspended cells.

Cell suspensions were sonicated on ice using a QSonica Q500 sonicator outfitted with a 6 mm probe operating at 30% power with 2 s pulses interspersed with 2 s delays for a combined runtime of 8 minutes. Lysates were then clarified by centrifugation (15000 rpm, 4 °C, 30 min) in a JA20 rotor (Beckman Coulter) operating in an Avanti J-26 XP centrifuge. The soluble fraction was loaded onto a 10 mL bed volume of Ni-NTA Sepharose Fast Flow resin, pre-equilibrated in lysis buffer in a gravity column. All subsequent steps were performed at 4 °C to limit proteolysis and aggregation. Repeated washes with lysis buffer (~3 column volumes, CV) were followed by two elution steps, the first with 3 CV of lysis buffer + 100 mM imidazole, the second with 6 CV of lysis buffer + 250 mM imidazole. Most proteins eluted in the 250 mM imidazole fractions, as assessed by SDS-PAGE and Coomassie staining. Fractions containing the

highest amounts of the protein of interest were dialyzed overnight against 20 mM Tris, 500 mM NaCl, 0.5 mM benzamidine, 2.5 mM 2-mercaptoethanol, pH 7.5. Ulp protease (possessing a N-terminal His₆ tag; purified in-house) was included to cleave the His₆-SUMO tag. The cleaved protein was then re-applied to the Ni-NTA resin pre-equilibrated in lysis buffer. Following several washes with lysis buffer (usually exceeding 5 CV), most of the cleaved protein of interest eluted from the column, while His₆-Ulp and His₆-SUMO would remain bound along with any uncleaved protein. At this stage, subsequent purification steps diverged depending on the protein.

Purification of mChPARP1 and XRCC1

Flowthrough and wash fractions from the second nickel column containing mChPARP1 or XRCC1 were pooled and concentrated by centrifugation in an Amicon Ultra-15 concentrator unit equipped with a 50 kDa molecular weight cutoff (MWCO) membrane. Concentrated samples (~5 mL volume) were loaded onto a HiLoad Superdex 200 26/60 (Cytiva) column pre-equilibrated in 25 mM Tris, 1 M NaCl, 0.5 mM sodium ethylenediaminetetraacetic acid (EDTA), 2 mM dithiothreitol (DTT), pH 7.5, and resolved isocratically over 1 CV at a constant flow rate of 1.5 mL min⁻¹. Fractions were assessed by SDS-PAGE and Coomassie staining. Those containing the highest amounts of pure protein were pooled and diluted with Q buffer A (10 mM Tris, 0.5 mM EDTA, 2.5 mM 2-mercaptoethanol, pH 8.0) to achieve a final NaCl concentration of 200 mM. Note that lower salt concentrations should be avoided to prevent aggregation and/or phase separation at this stage. Samples were then resolved on a monoQ FPLC HR 5/5 anion exchange column (Pharmacia) attached to an AKTA FPLC system (GE Healthcare) using a linear buffer gradient extending from 90% Q buffer A/10% Q buffer B (10 mM Tris, 1 M NaCl, 0.5 mM EDTA, 2.5 mM 2-mercaptoethanol, pH 8.0) to 100% buffer B over 50 mL. This step was crucial to remove contaminating bacterial DNA, which typically eluted at NaCl concentrations above ~300 mM (i.e., 30% buffer B), from XRCC1 or mChPARP1, which both eluted at relatively low salt concentrations. Samples of fractions containing XRCC1 or mChPARP1 were resolved on 15% tris-borate-EDTA (TBE)-urea polyacrylamide gels stained with SYBR Gold to confirm the absence of fragmented DNA. Protein-containing fractions were then pooled and dialyzed against storage buffer 250: 25 mM Tris, 250 mM NaCl, 0.5 mM EDTA, 2 mM DTT, pH 7.5. The buffer-exchanged samples were again concentrated, aliquoted, and flash frozen in a dry ice-ethanol slurry for long term storage at -80 °C.

Purification of LIG3 and LIG3 ΔBRCT

Following the second nickel column, most LIG3 and LIG3 ΔBRCT was present in the wash fractions (containing ~250 mM NaCl). These fractions were pooled and loaded onto a 5 mL HiTrap Blue HP column (Cytiva) pre-equilibrated in Blue buffer A (25 mM HEPES, 300 mM NaCl, 0.5 mM EDTA, 2.5 mM 2-mercaptoethanol, 10% v/v glycerol, pH 7.5) using a peristaltic pump (Cytiva). The column was then attached to an AKTA FPLC system (GE Healthcare) and bound proteins were eluted with a linear gradient from 100% Blue buffer A to 100% Blue buffer B (same as A except containing 2 M NaCl) over 50 mL (10 CV). LIG3 and LIG3 ΔBRCT both eluted around ~400-600 mM NaCl. Fractions were assessed by SDS-PAGE and Coomassie staining. Those containing LIG3 or LIG3 ΔBRCT were concentrated in an Amicon Ultra-15 centrifugal concentrator outfitted with a 50 kDa MWCO membrane and injected onto a HiLoad Superdex 200 26/60 (Cytiva) column pre-equilibrated in 25 mM Tris, 1 M NaCl, 0.5 mM EDTA, 2 mM DTT, pH 7.5. Proteins were resolved isocratically over 1 CV with a constant flow rate of 1.5 mL min⁻¹. Fractions containing the purest protein were pooled and dialyzed against storage buffer 500: 25 mM Tris, 500 mM NaCl, 0.5 mM EDTA, 2 mM DTT, pH 7.5. Buffer-exchanged samples were again concentrated, aliquoted, and flash frozen in a dry ice-ethanol slurry for long term storage at -80 °C.

Purification of APLF, APTX, PNKP, POLB, and PARG

Following the second nickel column APLF, APTX, PNKP, POLB, and PARG were purified according to the same protocol, with the exception that additional ion exchange steps were included after size exclusion chromatography as needed. Fractions from the second nickel column containing the protein of interest were pooled and concentrated in an Amicon Ultra-15 centrifugal concentrator outfitted with a 10 kDa MWCO membrane (for PARG, a 50 kDa MWCO membrane sufficed). Note that for APLF, Ulp cleavage was typically incomplete, although the expression yield was so high that the final yield was uncompromised. Concentrated proteins were resolved isocratically on a HiLoad Superdex 200 26/60 (Cytiva) column pre-equilibrated in 25 mM Tris, 1 M NaCl, 0.5 mM sodium EDTA, 2 mM DTT, pH 7.5, at a constant flow rate of 1.5 mL min⁻¹. Fractions were assessed by SDS-PAGE and Coomassie staining.

At this stage, APTX, POLB and PARG were of sufficient purity to proceed directly to buffer exchange and storage. Fractions containing the purest protein were pooled and dialyzed against storage buffer 500. Samples were then concentrated again, aliquoted, and flash frozen for long term storage at -80 °C.

After size exclusion chromatography, APLF and PNKP required an additional ion exchange step to reach acceptable purity. Fractions containing PNKP were pooled and diluted with SP buffer A (25 mM HEPES, 0.5 mM EDTA, 2.5 mM 2-mercaptoethanol, pH 7.0) to yield a final NaCl concentration of ~50 mM. Samples were loaded onto a 5 mL HiTrap SP HP column (Cytiva) pre-equilibrated in 95% SP buffer A/5% SP buffer B (25 mM HEPES, 1 M NaCl, 0.5 mM EDTA, 2.5 mM 2-mercaptoethanol, pH 7.0) using a peristaltic pump. Bound proteins were eluted by attaching the column to an AKTA FPLC and applying a linear buffer gradient from 95% SP buffer A/5% SP buffer B to 100% buffer B over 50 mL (10 CV). For APLF, a similar protocol was followed using a 5 mL HiTrap Q HP column (Cytiva) and Q buffers A (25 mM Tris, 0.5 mM EDTA, 2.5 mM 2-mercaptoethanol, pH 8.0) and B (same as A but including 1 M NaCl). In all cases, fractions were assessed by SDS-PAGE and Coomassie staining. Those containing the purest protein were pooled and dialyzed against storage buffer 500, concentrated and stored at -80 °C.

Purification of HPF1

Following the second nickel column, fractions containing the highest amounts of HPF1 were pooled and concentrated by centrifugation in an Amicon Ultra-15 concentrator unit equipped with a 10 kDa molecular weight cutoff (MWCO) membrane. Concentrated samples were resolved on a HiLoad Superdex 75 26/60 (Cytiva) column pre-equilibrated in 25 mM Tris, 250 mM NaCl, 0.5 mM EDTA, 2 mM DTT, pH 7.5, and resolved isocratically over 1 CV with a constant flow rate of 1.5 mL min⁻¹. Fractions were assessed by SDS-PAGE and Coomassie staining. Those containing the purest protein were pooled and diluted with S buffer A (25 mM bis-tris, 0.5 mM EDTA, 2.5 mM 2-mercaptoethanol, pH 6.0) to achieve a final NaCl concentration of ~50 mM. Samples were then injected onto a monoS FPLC HR 5/5 cation exchange column (Pharmacia) attached to an AKTA FPLC and pre-equilibrated in 5% S buffer B (25 mM bis-tris, 2 M NaCl, 0.5 mM EDTA, 2.5 mM 2-mercaptoethanol, pH 6.0). Proteins were eluted using a linear buffer gradient extending from 5% to 50% buffer B over 50 mL. Fractions containing the purest protein were pooled and dialyzed against storage buffer 250: 25 mM Tris, 250 mM NaCl, 0.5 mM EDTA, 10% v/v glycerol, 2 mM DTT, pH 7.5. Buffer-exchanged samples were again concentrated, aliquoted, and flash frozen in a dry ice-ethanol slurry for long term storage at -80 °C.

Purification of CK2

Casein kinase 2 α and β subunits were expressed and purified separately according to the protocol described above ([expression and initial purification of mCherryPARP1, XRCC1, LIG3, PARG, HPF1, casein kinase 2 and other DNA repair proteins in E. coli](#)). Fractions from the second nickel column containing CK2 α or β (with His₆-SUMO tags removed by Ulp) were pooled and concentrated in an Amicon Ultra-15 centrifugal concentrator outfitted with a 10 kDa MWCO membrane. Each was further purified on a HiLoad Superdex 75 16/60 (Cytiva) column pre-equilibrated in 25 mM Tris, 250 mM NaCl, 0.5 mM EDTA, 2 mM DTT, pH 7.5, and resolved isocratically over 1 CV with a constant flow rate of 0.5 mL min⁻¹. Fractions containing purified protein were pooled and concentrated again. To assemble the active tetrameric form of the kinase complex (containing 2 α and 2 β subunits), the two purified subunits were combined in a 1:1 ratio in the same size exclusion buffer described above. This mixture was resolved on a Superdex 200 Increase 10/300 column GL column in the same buffer at 4 °C, using a constant flow rate of 0.3 mL min⁻¹. Three species eluted—the earliest eluting peak corresponded to the assembled tetramer as assessed by SDS-PAGE, while the later eluting peaks corresponded to leftover unassembled α and β subunit monomers. Fractions containing the assembled complex were pooled, concentrated, and buffer exchanged into 25 mM Tris, 170 mM NaCl, 15% v/v glycerol, 0.5 mM EDTA, 2 mM DTT, pH 7.5. Concentrated aliquots were flash frozen and stored at a final concentration of 7.5 μ M (based on 280 nm UV absorbance measurements, assuming a tetrameric $\alpha_2\beta_2$ assembly) at -80 °C.

Histone expression and purification

pET21b vectors encoding untagged *D. melanogaster* H2A, H3 or H4 were transformed into chemically competent *E. coli* BL21-CodonPlus (DE3)-RIPL cells. Successful transformants were selected on LB-agar containing carbenicillin (100 μ g mL⁻¹). A pET28 vector containing *D. melanogaster* H2B tagged with a N-terminal TEV-cleavable His₆-tag was transformed into the same cell line, except kanamycin-containing (50 μ g mL⁻¹) LB-agar was used for selection. Note that the H2B and H4 constructs contained an additional isoleucine residue at the N terminus (in the case of H2B, just after the TEV cleavage sequence) to improve expression yield.

For protonated histone samples, colonies from overnight selection were picked and added to 50 mL LB cultures supplemented with 100 μ g mL⁻¹ ampicillin (for H2A, H3, H4) or 50 μ g mL⁻¹ kanamycin (H2B), which were allowed to incubate overnight at 37 °C with 250 rpm shaking. These cultures were then used to inoculate 1 L LB cultures in 2.5 L Fernbach flasks. Large-scale cultivation continued at 37 °C with 250 rpm shaking until an OD₆₀₀ of ~1.0 was attained, at which point 1 mM IPTG was added. For H2A, H2B and H3, induced cultures were allowed to grow overnight (~18 h) at 37 °C before harvesting. For H4, whose expression is more toxic to *E. coli*, the cells were harvested 5 h following induction and incubation at 37 °C. In each case, cells were harvested by centrifugation in an Avanti J-26 XP centrifuge equipped with a JLA 9.1000 rotor.

To prepare perdeuterated histones, colonies were added to 200 mL LB cultures supplemented with the appropriate antibiotic early in the morning. These cultures were allowed to incubate for ~6–8 h at 37 °C with 250 rpm shaking until they became turbid, at which point they were sedimented by centrifugation. Cell pellets were resuspended in 200 mL M9 media (6 g L⁻¹ disodium hydrogen phosphate, 3 g L⁻¹ potassium dihydrogen phosphate, 1 g L⁻¹ NaCl, 0.5 g L⁻¹ ammonium chloride, pD 7.4) prepared with D₂O (Cambridge Isotope Laboratories) instead of H₂O and supplemented with 2 mM MgSO₄, 0.1 mM CaCl₂, 3 g L⁻¹ ¹²C₆H₇-D-glucose (Cambridge Isotope Laboratories), 10 mg L⁻¹ D-biotin, 10 mg L⁻¹ thiamine and the appropriate antibiotic. Deuterated growth media was sterile filtered prior to use. For ¹⁵N isotopic labelling, ammonium chloride (the sole nitrogen source in this recipe) was substituted with ammonium-¹⁵N chloride (Sigma Aldrich). For ¹³C isotopic labelling, ¹²C₆H₇-D-glucose was substituted with ¹³C₆H₇-glucose. These cultures were allowed to continue incubating overnight (~18 h) at 37 °C with 250 rpm shaking. The next day, the cultures were expanded to 1 L volumes of the same growth media in 2.5 L Fernbach flasks and kept growing at 37 °C with 250 rpm shaking. Upon reaching an OD₆₀₀ of ~1.0, IPTG was added to a final concentration of 1 mM. For selective labelling of methyl groups in isoleucine, leucine, and valine residues with ¹³C¹H (otherwise perdeuterated and carbon natural abundance), the following precursors were added to growth media ~1 h prior to IPTG induction: 60 mg L⁻¹ ¹³C-methyl, 3,3-²H, α -ketobutyric acid and 80 mg L⁻¹ 3-methyl-¹³C, 3,4,4,4-²H, α -ketoisovaleric acid (Cambridge Isotope Laboratories). After induction, H2A, H2B and H3-expressing cells were incubated overnight at 37 °C with 250 rpm shaking and harvested the next day. H4 cultures were harvested 5 h following induction.

Following expression and harvesting, cell pellets were resuspended in wash buffer: 50 mM Tris, 100 mM NaCl, 1% v/v Triton X-100, pH 7.5. Cell suspensions were subjected to sonication (30% power, 2 s pulses with 2 s delays, 10 min total runtime) on ice. Lysates were sedimented by centrifugation at 18000 \times g, 30 min at 4 °C. The insoluble material was resuspended in wash buffer lacking Triton

X-100 and sonicated a second time using the same settings as above. The lysate was sedimented again under the same conditions. Insoluble material was resuspended in unfolding buffer (20 mM Tris, 6 M guanidinium chloride, pH 7.5) and sonicated again, as above. In the case of H2B, 20 mM imidazole was included in the unfolding buffer.

For H2A, H3 and H4, the lysates were sedimented a final time and dialyzed twice against 1 L volumes of urea buffer A: 50 mM sodium phosphate, 7 M urea, 1 mM EDTA, 50 mM NaCl, pH 7.4. Note that this buffer was prepared from 8 M urea that had been pre-treated with 50 g L⁻¹ Amberlite resin (Millipore-Sigma) for at least 1 h at room temperature. Histones solubilized in urea buffer were loaded onto two tandem 5 mL HiTrap SP HP columns (Cytiva) pre-equilibrated in urea buffer A on a peristaltic pump. Following loading, the columns were attached to an AKTA FPLC, and bound material was eluted over a linear buffer gradient from 100% urea buffer A to 100% urea buffer B (50 mM sodium phosphate, 7 M urea, 1 mM EDTA, 1 M NaCl, pH 7.4). Fractions were assessed by SDS-PAGE and Coomassie staining. Those containing the highest amounts of pure protein were pooled and dialyzed twice against 5 L deionized water before being lyophilized for long term storage at -20 °C.

For His-tagged H2B, the insoluble material remaining after the second wash step was resuspended in unfolding buffer supplemented with 20 mM imidazole. Following another round of sonication and sedimentation, the soluble fraction was loaded onto a 10 mL bed volume of Ni-NTA Sepharose Fast Flow resin pre-equilibrated in unfolding buffer + 20 mM imidazole. Bound H2B was eluted with elution buffer: 20 mM Tris, 6 M guanidinium chloride, 500 mM NaCl, 300 mM imidazole, pH 7.5. Fractions containing H2B were pooled and slowly dripped into a rapidly stirring solution of TEV cleavage buffer (20 mM sodium phosphate, 500 mM L-arginine chloride, 500 mM NaCl, 2 mM DTT, pH 7.5) using a peristaltic pump system. TEV protease was added to this solution for overnight cleavage of the His-tag at 4 °C. The protease and tag were removed by applying this reaction mixture to the Ni-NTA column under the same conditions described above. H2B present in the flowthrough was dialyzed twice against 5 L deionized water and lyophilized for long term storage at -20 °C.

Expression and purification of mAP

The pET21a plasmid encoding His₆-tagged mAP was transformed into chemically competent *E. coli* BL21-CodonPlus (DE3)-RIPL cells which were subsequently selected on carbenicillin (100 µg mL⁻¹)-containing LB-agar. Colonies were used to inoculate a 50 mL LB culture containing ampicillin (100 µg mL⁻¹) which was incubated overnight at 37 °C with 250 rpm shaking. This small-scale culture was then used to inoculate 1 L LB cultures in 2.5 L Fernbach flasks which were incubated under the same conditions until an OD₆₀₀ of ~0.9 was attained. IPTG (0.5 mM) was added to induce mAP expression over ~18 h at 18 °C with 250 rpm shaking. Cells were harvested by centrifugation and resuspended in periplasmic lysis buffer (200 mM Tris, 20% w/v sucrose, 1 mM EDTA, pH 7.5). Approximately 1 mg of hen egg white lysozyme were added to aid in lysing the bacterial cell wall. The cell suspension was incubated on ice for 5 min. Osmotic shock was induced by immediate addition of an equal volume of ice-cold water. The suspension was centrifuged at 12000 × *g* for 20 min at 4 °C. The soluble fraction was applied to Ni-Sepharose resin pre-equilibrated in wash buffer (25 mM Tris, 250 mM NaCl, 10% v/v glycerol, 2.5 mM 2-mercaptoethanol, pH 7.5). After extensive washing with several CVs of wash buffer and wash buffer containing 100 mM imidazole, bound protein was finally eluted with elution buffer (25 mM Tris, 250 mM imidazole, 250 mM NaCl, 10% v/v glycerol, 2.5 mM 2-mercaptoethanol, pH 7.5). Fractions were assessed by SDS-PAGE and Coomassie staining. Those containing mAP were concentrated using an Amicon Ultra-15 centrifugal concentrator unit equipped with a 10 kDa MWCO membrane and injected onto a HiLoad Superdex 75 16/600 column equilibrated in 25 mM Tris, 500 mM NaCl, 0.5 mM EDTA, 2 mM DTT, pH 7.5. The protein was resolved isocratically over 1 CV at a flow rate of 0.3 mL min⁻¹. Fractions were again assessed by electrophoresis; those containing mAP were generally quite pure. After pooling and concentrating the relevant fractions to ~110 µM, the protein was flash frozen and stored in gel filtration buffer at -80 °C.

Expression and purification of Nt.BsmAI

The pCOLA Duet-1 vector containing the *nt.bsmAI* (N-terminally tagged with His₆-SUMO) and *bsmAI/M* genes was transformed into chemically competent *E. coli* BL21-CodonPlus (DE3)-RIPL cells. Successful transformants were selected on kanamycin-containing LB-agar and used to inoculate a 50 mL LB culture containing kanamycin (100 µg mL⁻¹). Following overnight incubation at 37 °C with 250 rpm shaking, this small-scale culture was used to inoculate 1 L LB cultures in 2.5 L Fernbach flasks. Large-scale cultures were incubated under the same conditions until an OD₆₀₀ of ~0.9 was attained, at which point IPTG was added to a final concentration of 0.3 mM. Cells were cultivated for another 18 h at 18 °C with 250 rpm shaking before being harvested by centrifugation. Cell pellets were resuspended in lysis buffer (25 mM Tris, 250 mM NaCl, 10% v/v glycerol, 25 mM imidazole, 2.5 mM 2-mercaptoethanol, pH 7.5) supplemented with microgram-milligram amounts of bovine pancreatic DNase I, hen egg white lysozyme, and 1 cOmplete protease inhibitor cocktail tablet. Lysis was achieved by sonication on ice (using a QSonica Q500 sonicator; 30% power, 2 s pulses with 2 s delays, 8 min total). Lysates were clarified by centrifugation at 21000 × *g* for 30 min at 4 °C. The soluble fraction was loaded onto Ni-Sepharose resin equilibrated in the same buffer. Multiple washes (~10 CV) with lysis buffer were followed by elution using several CVs of 25 mM Tris, 250 mM NaCl, 250 mM imidazole, 10% v/v glycerol, 2.5 mM 2-mercaptoethanol, pH 7.5. Fractions containing SUMO-tagged Nt.BsmAI were pooled and dialyzed overnight against 20 mM Tris, 150 mM NaCl, 2.5 mM 2-mercaptoethanol, 0.5 mM benzamidine, pH 7.5. His₆-tagged Ulp protease was added to cleave the His₆-SUMO tag. Reapplication of the sample onto the nickel resin under the same buffer conditions enabled separation of the cleaved Nt.BsmAI from the His₆-SUMO tag and protease. Flow-through and wash fractions containing Nt.BsmAI were applied to a HiLoad Superdex 75 16/600 gel filtration column equilibrated in 25 mM Tris, 300 mM NaCl, 2 mM DTT, pH 7.5. Purest fractions were collected and concentrated for long term storage in the same buffer condition, with glycerol added to a final volume fraction of 20% v/v to stabilize the enzyme during repeated freeze/thaw cycles. Aliquots were flash frozen and stored at -80 °C.

Expression and purification of 601-DNA

A pUC19 vector harbouring approximately 30 copies of the 601-DNA sequence separated by short 12 bp linkers was transformed into chemically competent *E. coli* BL21 (DE3) cells. Transformants were selected on LB-agar containing ampicillin ($100 \mu\text{g mL}^{-1}$). Colonies were picked and used to inoculate 5 mL volumes of Terrific Broth+ (TB+), containing $100 \mu\text{g mL}^{-1}$ ampicillin, 0.4% v/v glycerol, 7 mM MgSO_4 , which were then grown at 37°C with 250 rpm shaking. Upon reaching an OD_{600} of ~ 2.0 , these cultures were used to inoculate 100 mL TB+ cultures that were then incubated under the same growth conditions. After several hours, an OD_{600} of ~ 1.5 was attained, at which point these cultures were transferred to larger 1 L volumes of TB+ in 2.5 L Fernbach flasks. Incubation continued overnight at 37°C with 250 rpm shaking. The next morning, cells were sedimented by centrifugation and stored at -20°C until later use. Prior to storage, plasmid DNA from ~ 4 mL volumes of each culture were extracted using a QIAGEN Plasmid Mini kit (following the manufacturer's instructions) in order to roughly estimate the plasmid DNA content in each pellet. This was an important consideration for guaranteeing consistency in yield and for determining the appropriate number of columns to use in large-scale DNA purifications to follow.

Plasmid DNA was extracted from cell pellets originating from 1 L TB+ growths using a QIAGEN Plasmid Giga kit. The manufacturer's instructions were followed with slight variations. Based on the estimated yield from each cell pellet, 1 QIAcolumn was used per ~ 10 mg plasmid DNA. 300 mL buffer QC was used instead of the recommended 600 mL during the washing steps. 180 mL buffer QF was used for elution instead of the recommended 100 mL. During the precipitation step, the DNA solution was stirred rapidly, while 2-propanol was added gradually in order to prevent formation of DNA aggregates that were difficult to redissolve.

DNA precipitates were dissolved directly into NEB3 buffer (50 mM Tris, 100 mM NaCl, 10 mM MgCl_2 , pH 7.9) for overnight digestion by EcoRV (NEB) at 37°C . The reaction mixture was loaded onto two tandem 5 mL HiTrap DEAE Sepharose FF columns (Cytiva) pre-equilibrated in Q buffer A. Copies of 601-DNA and the corresponding 12 bp interspersing segments were separated from the remainder of the plasmid using a linear buffer gradient from 100% Q buffer A to 100% Q buffer B—601-DNA and 12mers bound to the columns while the plasmid backbone did not. Fractions containing 601-DNA were resolved isocratically on a HiLoad Superdex 200 26/600 column pre-equilibrated in refolding buffer high ('RB High', 10 mM Tris, 2 M KCl, 1 mM EDTA, pH 7.5) to separate 601-DNA from the 12mer segments. Fractions containing 601-DNA were pooled and concentrated using an Amicon Ultra-15 centrifugal concentrator unit bearing a 10 kDa MWCO membrane. For long term storage, 601-DNA was kept in RB High at 4°C .

Protein modification

Alexa Fluor 488- C_5 -maleimide labeling of H3 Q125C

Purified and lyophilized H3 (Q125C) was dissolved in modified unfolding buffer: 20 mM sodium phosphate, 6 M guanidinium chloride, 2 mM tris(2-carboxyethyl)phosphine (TCEP), pH 7.5. Alexa Fluor 488- C_5 -maleimide was dissolved in dimethylsulfoxide (DMSO) to a working concentration of 20 mM. The labeling reaction was conducted in a mixture containing $20 \mu\text{M}$ H3 (Q125C) and $200 \mu\text{M}$ AF488- C_5 -maleimide diluted in modified unfolding buffer. Following an overnight (~ 18 h) incubation at 4°C in the dark with constant rocking, a small sample was analyzed by SDS-PAGE to ensure successful labeling. Minimal precipitation arose during labelling; this was sedimented by centrifugation at $21000 \times g$ for 5 min at 4°C . The soluble fraction of the sample was resolved on a HiLoad Desalting 26/60 column pre-equilibrated in quenching buffer: 20 mM Tris, 6 M guanidinium chloride, 2.5 mM 2-mercaptoethanol, 0.5 mM EDTA, pH 7.5. Fractions containing the AF488-labeled protein were pooled and purified further on a monoS FPLC 5/5 cation exchange column to completely remove any remaining unconjugated dye. Prior to injection, the sample was diluted in monoS buffer A (20 mM bis-tris, 1 mM EDTA, 2.5 mM 2-mercaptoethanol, pH 6.0) to achieve a guanidinium chloride concentration of ~ 100 mM. Bound H3 was eluted using a linear gradient up to 100% monoS buffer B (20 mM bis-tris, 1 M NaCl, 1 mM EDTA, 2.5 mM 2-mercaptoethanol, pH 6.0); the unconjugated dye eluted in the flowthrough. Fractions were again analyzed by SDS-PAGE and fluorescence imaging to ensure stringent separation of the free dye from the protein. AF488-labelled H3 was collected and buffer exchanged into unfolding buffer (20 mM Tris, 6 M guanidinium chloride, pH 7.5) for long term storage at -20°C .

Alexa Fluor 488- C_5 -maleimide labeling of XRCC1 and LIG3

XRCC1 (unmodified or phosphorylated) and LIG3 were exchanged into labeling buffer by dialysis: 25 mM Tris, 500 mM NaCl, 2 mM TCEP, 0.5 mM EDTA, pH 7.5. AF488- C_5 -maleimide was dissolved in DMSO to a working concentration of 20 mM. Labelling reaction mixtures contained $20 \mu\text{M}$ protein and $200 \mu\text{M}$ AF488- C_5 -maleimide dissolved in labeling buffer. After overnight incubation at 4°C in the dark, small samples of each reaction were analyzed by SDS-PAGE to ensure successful labeling. No visible aggregation was present during labeling of (phospho-)XRCC1 or LIG3, although samples were nevertheless sedimented by centrifugation at $21000 \times g$ for 5 min at 4°C prior to desalting. The soluble fraction of each sample was resolved on a HiLoad Desalting 26/60 column pre-equilibrated in quenching buffer: 25 mM Tris, 500 mM NaCl, 2.5 mM 2-mercaptoethanol, 0.5 mM EDTA, pH 7.5. Small amounts of unconjugated dye co-eluted with the proteins, necessitating additional purification on a monoS FPLC 5/5 column. A similar purification scheme was used as in the case of H3 labelling, except a final NaCl concentration of ~ 150 mM was achieved by diluting the sample with monoS buffer A before application onto the column. Most XRCC1 and LIG3 eluted at higher NaCl concentrations while unconjugated AF488 failed to bind. Fractions were analyzed by SDS-PAGE and fluorescence imaging to ascertain complete separation of the unconjugated dye from the protein. AF488-labelled (phospho-)XRCC1 and LIG3 were pooled, concentrated, aliquoted, and flash frozen for storage at -80°C .

Alexa Fluor 488-N-hydroxysuccinimidyl-ester labelling of APLF, APTX, PNKP, and POLB

Labeling of APLF, APTX, PNKP, and POLB was performed with *N*-hydroxysuccinimidyl (NHS)-ester-based chemistry instead of with maleimide. Purified proteins were dialyzed overnight at 4 °C into NHS labeling buffer: 25mM HEPES, 500mM NaCl, 0.5mM EDTA, 1mM TCEP, pH 7.5. AF488-NHS ester was dissolved in dimethylformamide to a working concentration of 10mM. Labeling reactions containing a 1:4 ratio of protein:dye dissolved in NHS labeling buffer were allowed to incubate for 2h at room temperature with constant rocking. Sample tubes were covered in aluminium foil to reduce light exposure. Reactions were quenched by adding 25 mM Tris, 2 mM 2-mercaptoethanol, pH 7.5 to each sample. To remove unconjugated dye, APTX, PNKP and POLB were diluted in monoS buffer A to achieve a final salt concentration of ~100 mM before being loaded onto a monoS FPLC 5/5 column. Protein was separated from unconjugated dye using the same protocol described for AF488-C₅-maleimide labeling of H3. Protein-containing fractions were analyzed by SDS-PAGE and fluorescence imaging to ensure complete separation of unconjugated dye from the protein.

For APLF, monoS purification was unsuccessful, necessitating an additional purification on a monoQ FPLC 5/5 column. The quenched APLF labelling reaction was diluted with monoQ buffer A (20 mM Tris, 0.5 mM EDTA, 2.5 mM 2-mercaptoethanol, pH 8.0) to achieve a final NaCl concentration of ~100 mM. The sample was loaded and resolved on the monoQ column using a linear buffer gradient from 100% monoQ buffer A to 100% buffer B (20 mM Tris, 1 M NaCl, 0.5 mM EDTA, 2.5 mM 2-mercaptoethanol, pH 8.0). Fractions containing APLF were pooled and concentrated using an Amicon Ultra-15 centrifugal concentrator unit equipped with a 30 kDa MWCO membrane and injected onto a HiLoad Superdex 200 16/600 column pre-equilibrated in 25 mM Tris, 150 mM NaCl, 2 mM DTT, 0.5 mM EDTA, pH 7.5. Protein-containing fractions were analyzed by SDS-PAGE and fluorescence imaging to ensure removal of any residual unconjugated dye.

All AF488-labelled proteins were collected and concentrated for storage at -80 °C. Prior to imaging experiments, aliquots of each protein were thawed and freshly dialyzed in separate GeBaFlex mini cassettes (with 3 kDa MWCO membranes) against 25 mM Tris, 500 mM NaCl, 2 mM DTT, 0.5 mM EDTA, pH 7.5 at 4 °C.

Phosphorylation of XRCC1 with CK2

Aliquots of purified XRCC1 and CK2 $\alpha_2\beta_2$ tetramer were thawed on ice. A reaction mixture was prepared with the following composition: 25 mM Tris, 50 mM NaCl, 1 mM DTT, 4 mM ATP-Mg (pH corrected to 7.5 with 12 M NaOH), 10 μ M XRCC1, 1 μ M CK2 tetramer, pH 7.5. Note that small amounts of glycerol carried over from the CK2 storage buffer. Phosphorylation was allowed to proceed overnight with gentle rocking at lab temperature (~22 °C). The next day, small samples were set aside for SDS-PAGE and LC/MS-MS analysis. CK2 was separated from phosphorylated XRCC1 by resolving the entire sample on a HiLoad Superdex 200 26/60 column pre-equilibrated in 25 mM Tris, 500 mM NaCl, 2 mM DTT, 0.5 mM EDTA, pH 7.5. Fractions found to contain phosphorylated XRCC1 (but not CK2) by SDS-PAGE analysis were pooled, collected, and concentrated using an Amicon centrifugal concentrator equipped with a 30 kDa MWCO membrane. Concentrated protein was aliquoted and stored at 10.5 μ M final concentration in the chromatography buffer at -80 °C.

601-DNA manipulation

mAP reaction

To remove terminal phosphate groups from 601-DNA, a reaction mixture was assembled with the following components: 25 mM Tris, 100 mM KCl, 1 mM CaCl₂, 2 mM DTT, 3 μ M DNA, 0.5 μ M mAP, pH 7.5. This was allowed to incubate overnight at 37 °C. The reaction was quenched by incubation in a water bath heated >65 °C for ~10 min. 601-DNA was purified by applying this mixture onto a monoQ FPLC HP 5/5 column pre-equilibrated in Q buffer A and eluting over a linear salt gradient into Q buffer B. 601-DNA normally elutes at salt concentrations ~600 mM (i.e., 60% buffer B) while other reaction components elute earlier. mAP activity was validated using a crude ligation assay: 1 μ L of the mAP reaction was combined with 1 mM magnesium adenosine triphosphate (Mg-ATP), 25 mM Tris, 1 mM DTT and T4 DNA ligase (NEB), pH 7.5 in a 10 μ L volume. Following a 10 min incubation period at 37 °C, products were resolved on a 1% agarose-tris-acetic acid-EDTA (TAE) gel stained with SafeView (Applied Biological Materials). Complete DNA dephosphorylation results in no ligation, with 601-DNA migrating as a single 153 bp species.

Nicking reaction with Nt.BsmAI

mAP-treated 601-DNA was buffer exchanged into water by dialysis or repeated concentration and dilution in an Amicon Ultra-15 centrifugal concentrator unit. The nicking reaction mixture contained the following: 50 mM Tris, 300 mM NaCl, 10 mM MgCl₂, 500 nM 601-DNA, 0.125 nM Nt.BsmAI, pH 8.7. Note that this reaction composition was carefully optimized to favour single strand cleavage. Nicking was allowed to proceed overnight at 37 °C. The next day, small samples of the reaction were resolved on denaturing TBE-urea 15% polyacrylamide and native TBE 12% polyacrylamide gels to ensure proper nicking and a lack of double-strand cuts, respectively. DNA was visualized by SYBR Gold staining. Nicked, dephosphorylated 601-DNA (n601) was purified from the other reaction components on a monoQ FPLC HR 5/5 column, exactly as detailed in the previous section on mAP treatment. Fractions containing n601 were pooled and exchanged into water.

Incorporation of the 3'-Alexa Fluor 647-, 5'-phosphate-labeled oligonucleotide

A DNA fragment with the same sequence as the portion of 601-DNA spanning the Nt.BsmAI nick site to the 3'-terminus was ordered from Integrated DNA Technologies. This oligonucleotide (simply called the '31mer' for brevity) was modified by the manufacturer to contain a 5'-phosphate and a 3'-Alexa Fluor 647 (AF647) fluorescent dye (Figure S1A). Upon receipt, the lyophilized 31mer was dissolved in DNase-free high purity water to a final concentration of 100 μ M. n601-DNA dissolved in water was mixed in a 1:1 ratio with the 31mer to yield final concentrations of 5 μ M in 50 mM NaCl. This mixture was heated to 95 °C for 5 min in a PCR machine to induce

DNA denaturation. Subsequent re-annealing of the 31mer with n601-DNA was achieved by allowing the sample to slowly re-equilibrate to room temperature on the bench over the course of 30 min. The cooled sample was injected onto a HiLoad Superdex 200 26/600 column pre-equilibrated in RB High. Unannealed 31mer eluted as a distinct peak after n601-DNA and was easily separable. Successful incorporation of the 31mer into n601-DNA was validated by native gel electrophoretic analysis; the efficiency of incorporation was estimated to be ~50% based on detection and quantification of AF647 fluorescence intensity in bands corresponding to n601-DNA. Partially AF647-labelled n601-DNA was pooled and concentrated for storage in RB High at 4 °C or -20 °C.

NCP reconstitution and PARylation

Histone octamer reconstitution

Lyophilized histones were dissolved in unfolding buffer (20 mM Tris, 6 M guanidinium chloride, pH 7.5) to a convenient working concentration (i.e., around 0.5–1 mM). Appropriate combinations of labeled and unlabeled histones were chosen depending on the desired composition of the octamer. For example, for enzyme assay samples, fully protonated histones with natural carbon and nitrogen isotope abundances were used. For NMR samples, typically a single histone of interest was ILV-labeled, perdeuterated, and enriched with ¹⁵N, while the others were only perdeuterated (possessing natural carbon and nitrogen isotope abundances).

The four histones (H2A, H2B, H3, H4) dissolved in unfolding buffer were combined in a 1:1:1:1 ratio at final concentrations of 70 μM. Excess unfolding buffer was added to achieve this final concentration. The mixture was placed in a GeBaFlex dialysis cassette scaled to the appropriate size depending on the sample volume. To prepare amounts of octamer that were sufficient for NMR samples, volumes typically exceeded 3.5 mL, while for enzyme assay samples, volumes could be less than 250 μL. Gradient dialysis was performed overnight at 4 °C. Briefly, the dialysis cassette was placed in a foam holder and floated in a rapidly stirring solution of RB High (10 mM Tris, 2 M KCl, 1 mM EDTA, pH 7.5). The volume of this solution was scaled (200 mL or 400 mL) depending on the size of the reconstitution reaction (400 mL was typically used for sample volumes exceeding 250 μL). A small hole was drilled into the side of the plastic beaker used to hold this solution at the 200 or 400 mL mark. An excess volume of RB High (0.8 L for the smaller scale reconstitutions, 1.6 L for the larger) was allowed to drip into the solution holding the sample using a peristaltic pump calibrated to ~1–1.5 mL min⁻¹. As more and more RB High was added in this manner, excess volume would flow out of the hole into a catchment tray. This was allowed to proceed until the excess volume of RB High was depleted, typically overnight.

Octamer reconstitution samples were resolved on a Superdex 200 Increase 10/300 column GL column pre-equilibrated with RB High at 4 °C. If required, samples were concentrated beforehand using an Amicon Ultra-4 centrifugal concentrator unit equipped with a 10 kDa MWCO membrane to achieve the maximum allowable volume for injection (500 μL). Octamer samples were resolved isocratically at a flow rate of 0.4 mL min⁻¹ over 1 CV. A Gaussian peak corresponding to the properly formed octamer would typically elute midway through the run while later-eluting, less prominent species comprising leftover histones and sub-octameric complexes would follow. Fractions corresponding to the octamer were analyzed by SDS-PAGE and Coomassie staining and then concentrated in RB High. Concentrations in the range of ~20–50 μM were considered ideal. Samples remained stable in RB High at 4 °C typically up to several months.

NCP reconstitution for enzyme assays, dynamic light scattering, and microscopy

Enzyme assays and imaging experiments (both cryo-EM and light microscopy) typically required smaller amounts of NCP than NMR samples, so samples needed for the former applications were prepared in a smaller format. The protocol was identical whether the 601-DNA was fluorescently labelled, nicked or unnicked. Histone octamers dissolved in RB High were mixed in a 1.1:1 molar ratio with (n)601-DNA also dissolved in RB High. Final concentrations of 6 μM DNA and 6.6 μM octamer were often used. Absorbance measurements at 260 nm (for DNA) or 280 nm (for histone octamers) UV light were used to measure concentrations. Higher octamer concentrations were used to minimize the amount of leftover ‘free’ DNA which could convolute interpretation of assay and microscopy data if present at moderate-to-high concentrations. For samples employed in fluorescence imaging and ligation experiments, n601-DNA containing ~5 mol% AF647-labeled 31mer was used. Otherwise, unlabeled n601-DNA sufficed. For MNase and DLS experiments, unnicked, unlabeled 601-DNA was used instead.

Gradient dialysis at 4 °C was set up in a similar fashion as for octamer reconstitution. The octamer-DNA mixture was placed in a GeBaFlex dialysis cassette floating in 200 mL RB High. For these smaller-scale reconstitutions, sample volumes were typically ≤ 250 μL. A 1 L volume of pre-chilled RB Low (10 mM Tris, 150 mM KCl, 1 mM EDTA, pH 7.5) was dripped into the beaker containing the sample and the RB High at a constant flow rate of 1 mL min⁻¹. As in the case of octamer reconstitution, a small hole was inserted at the 200 mL mark to allow spillover of excess buffer into a catchment tray. Rapid stirring was essential to ensure proper mixing of the RB Low and High. This process continued until the RB Low was depleted. Minimal amounts of precipitation were typically observed.

Proper (n)NCP assembly was validated by native gel electrophoresis on a TBE 6% polyacrylamide gel with an applied voltage of 80 V over 75 min. Running buffer was pre-chilled, and the tank containing the buffer and gel apparatus was submerged in ice water to ensure homogenous cooling. (n)NCPs were visualized by AF647 fluorescence or SafeView (for DNA) or Coomassie (for histones). Samples were centrifuged at maximum speed (21000 × g for 10 min at 4 °C) to remove precipitates. Samples stored in RB Low at 4 °C were stable long term. NCP concentration was measured based on DNA absorbance at 260 nm by spectrophotometry.

Octamer wrapping with n601-DNA for NMR samples

Samples prepared for NMR required higher nNCP concentrations than other types of experiments, so a larger reconstitution format was used. Prior to large-scale NCP reconstitution, a smaller-scale trial run was used every time to identify an ideal DNA:octamer

concentration ratio. Due to small, sample-to-sample variations in concentration measurements and buffer conditions, inclusion of this step insured against losing large amounts of DNA or octamer to aggregation. n601-DNA was held at a constant concentration (6 μ M) while the octamer concentration was varied 0.8–1.2 \times in increments of 0.1. Octamers contained the desired isotopic enrichment patterns and were prepared in RB High as described above. 50–70 μ L volumes of each condition were placed in GeBaFlex mini cassettes floating in 200 mL RB High. Gradient dialysis was performed at 4 $^{\circ}$ C using 1 L of RB Low as described in the previous section. Native gel electrophoresis using a TBE 6%-polyacrylamide gel was used to estimate the ratio of nNCP to free n601-DNA remaining in the samples. Optimal ratios were defined as those containing the least aggregation and the highest ratio of NCP to free DNA; often ratios of 0.9–1.0 octamer:DNA were selected. For NMR samples, higher concentrations of DNA were preferred to minimize the concentration of free histones left in the sample.

Using the optimal octamer:DNA ratio, a large-scale reconstitution reaction was prepared. Sample volumes exceeding 10 mL in multiple GeBaFlex maxi cassettes were typical. The volumes of RB High and RB Low were scaled up to 400 mL and 2 L respectively. Gradient dialysis at 4 $^{\circ}$ C proceeded as described, followed by native gel electrophoresis to ensure proper reconstitution. nNCP samples were concentrated in Amicon Ultra-15 centrifugal concentration units equipped with 10 kDa MWCO membranes and stored in RB Low at 4 $^{\circ}$ C until further use.

For unPARylated nNCP NMR samples, the nNCP was buffer exchanged into 20 mM sodium phosphate, 100 mM NaCl, 0.1 mM EDTA, pH 6.0 by serial concentration and dilution. The final nNCP concentration was measured by 260 nm absorbance based on the theoretical molar absorptivity of n601-DNA; all samples contained between 80–110 μ M in \sim 300 μ L. Deuterium oxide (D_2O) was added to a final concentration of 3% v/v. Samples were inserted into 5 mm Shigemi tubes prior to data acquisition.

Small-scale nNCP PARylation

Small-scale PARylation reactions were typically prepared with the following composition: 25 mM Tris, 37.5 mM KCl, 112.5 mM NaCl, 0.5 μ M nNCP, 1 μ M mChPARP1, 1.5 μ M HPF1, 0.5 mM $MgCl_2$, 2.5 mM DTT, 1 mM NAD^+ , pH 7.5. mChPARP1 and HPF1 were premixed at 10 \times concentration (i.e., 10 μ M mChPARP1 and 15 μ M HPF1) in storage buffer 250 (25 mM Tris, 250 mM NaCl, 0.5 mM EDTA) prior to addition. In some conditions, HPF1 was excluded and replaced with storage buffer 250. nNCP samples were prepared in RB Low (10 mM Tris, 150 mM KCl, 1 mM EDTA, pH 7.5). NAD^+ stock solutions (10 mM) were prepared in deionized water and filtered. PARylation reactions were allowed to proceed for 20 min at 37 $^{\circ}$ C. To qualitatively assess the extent of PARylation, samples were quenched in 4 \times SDS-PAGE loading buffer and resolved on 4%–12% polyacrylamide SDS gels. Histones and mChPARP1 were visualized by Coomassie staining, or, when nNCPs contained AF488-H3, AF488 fluorescence. Variations in the reaction compositions were introduced depending on the experiment. For example, for PARylation of nNCPs containing AF488-labelled H3 in Figure S1F, HPF1 was selectively excluded in some conditions. Please see the sections pertaining to specific assays for more details.

Large-scale nNCP PARylation for NMR

PARylated nNCP NMR samples were prepared by enzymatically modifying samples that had been previously used to acquire data in the unmodified state. For instance, the unmodified and PARylated spectra derived from H3 originated from the same nNCP sample containing isotopically labeled H3, before and after PARylation.

nNCP NMR samples were incorporated into PARylation reaction mixtures with the following final composition: 25 mM Tris, 150 mM NaCl, 1 μ M nNCP, 1 μ M mChPARP1, 1.5 μ M HPF1, 0.5 mM $MgCl_2$, 2.5 mM DTT, 2 mM NAD^+ , pH 7.5. mChPARP1 and HPF1 were premixed at 10 \times concentration (i.e., 10 μ M mChPARP1 and 15 μ M HPF1) in storage buffer 250 (25 mM Tris, 250 mM NaCl, 0.5 mM EDTA) prior to addition. nNCP samples were buffer exchanged into RB Low prepared with sodium instead of potassium chloride (10 mM Tris, 150 mM NaCl, 1 mM EDTA, pH 7.5). NAD^+ stock solutions were prepared in deionized water and filtered. The reaction was allowed to proceed at 37 $^{\circ}$ C for 30 min. Sample volumes were scaled depending on the original quantity of nNCP in the NMR sample, but typically exceeded 30 mL. Following this incubation period, the entire sample volume was loaded into a 50 mL Superloop and connected to an AKTA FPLC System in line with a HiLoad Superdex 200 26/60 size exclusion column pre-equilibrated in NMR buffer at 4 $^{\circ}$ C. Typically the NMR buffer had the same composition as described above (20 mM sodium phosphate, 100 mM NaCl, 0.1 mM EDTA, pH 6.0), although the sodium chloride was omitted for experiments conducted with ‘no-salt’ (20 mM sodium phosphate, 0.1 mM EDTA, pH 6.0). Three consecutive injections (with maximum volumes of 12 mL) were performed over three identical runs at a constant flow rate of 1.5 mL min $^{-1}$. Fractions were collected at retention volumes spanning 80–260 mL from the point of injection. Each consecutive injection resulted in nearly identical chromatograms. PARylated nNCPs eluted as a single peak partially overlapping with an earlier-eluting peak containing automodified mChPARP1. Complete separation of these two peaks was not possible. All fractions containing PARylated nNCPs (as assessed by SDS-PAGE and Coomassie staining) were pooled and concentrated using an Amicon Ultra-15 centrifugal concentrator unit bearing a 10 kDa MWCO membrane. Final nNCP concentrations were estimated by calibration of SDS-PAGE band intensities to standardized amounts of H2B loaded on the same gel and stained with Coomassie. Samples were supplemented with 3% v/v D_2O and inserted into 5 mm Shigemi tubes.

Sample preparation for ADP-ribose quantification

A PARylated nNCP NMR sample containing ^{13}C , ^{15}N -labelled H3 (all other histones were protonated and isotopically unlabelled) was prepared according to the protocol described above with the following modifications. After incubating the PARylation reaction for 30 min at 37 $^{\circ}$ C, an equal volume of 8 M guanidium chloride was added to achieve a final concentration of 4 M. This mixture was concentrated to a final volume of \sim 12 mL using an Amicon centrifugal concentrator unit equipped with a 3 kDa MWCO membrane. Portions of the sample were serially injected onto a HiLoad Superdex 200 26/60 size exclusion column pre-equilibrated in 25 mM Tris, 4 M guanidinium chloride, 0.5 mM EDTA, pH 7.5 at lab temperature (\sim 22 $^{\circ}$ C). Each run had a duration of 320 mL (\sim 1 CV) with a constant

flow rate of 1.5 mL min⁻¹, collecting fractions over retention volumes spanning 80–280 mL. PARylated mChPARP1 eluted early in the run, well resolved from DNA and PARylated H3, which were partially overlapping. Some of the unmodified histones coeluted with the PARylated H3, although this was not deemed an issue for subsequent NMR experiments as these histones were isotopically unlabelled. Fractions spanning retention volumes 170–250 mL were pooled and concentrated in an Amicon centrifugal concentrator unit (3 kDa MWCO) to a final volume of ~1.1 mL and dialyzed in a GeBAflex midi dialysis cassette against NMR buffer (20 mM sodium phosphate, 100 mM NaCl, 0.1 mM EDTA, pH 6.0) overnight at 4 °C. A sample of unPARylated, ¹³C, ¹⁵N-labelled H3 (to use as a standard of known H3 concentration in subsequent NMR experiments) was dialyzed against the same buffer in a separate GeBAflex midi cassette. The next morning, both samples were clarified by centrifugation at maximum speed (21000 × *g* for 10 min at 4 °C) and supplemented with 3% v/v D₂O. The PARylated-H3 sample was split into 2 × 500 μL samples; in one sample, 50 nM PARG was added to hydrolyze PAR, while to the other, 0.05 mg mL⁻¹ proteinase K was added to hydrolyze the protein backbone. The PARG reaction was allowed to proceed for 1.5 h at lab temperature (22 °C), whereas the proteinase K-treated sample was incubated overnight at 50 °C. Each sample was transferred to a 5 mm NMR tube. The concentration of the H3 standard was measured by absorbance at 280 nm, using the theoretical molar extinction coefficient calculated from the *Drosophila* H3 primary sequence (4470 M⁻¹ cm⁻¹). Proteinase K treatment was also performed on this sample using the same conditions described above. Another standard containing 1.0 mM ADP-ribose was prepared by dissolving adenosine 5′-diphosphoribose disodium salt powder in the same NMR buffer used for dialyzing the protein samples. This standard was filtered through a 0.22 μm membrane, supplemented with 3% v/v D₂O, and transferred into a 5 mm tube.

Enzyme assays

Ligation assays—General protocol including PARylation

Ligation reactions generally contained the following components: 25 mM Tris, 37.5 mM KCl, 112.5 mM NaCl, 0.5 μM nNCP (containing 5 mol% AF647-labelled n601-DNA), 1 μM mChPARP1, 1.5 μM HPF1, 1 mM MgATP, 1 mM DTT, 1 mM NAD⁺, pH 7.5, with variable concentrations of XRCC1/LIG3. A stock solution of mChPARP1 and HPF1 was premixed at 10× concentration (i.e., 10 μM mChPARP1 and 15 μM HPF1) in storage buffer 250 (25 mM Tris, 250 mM NaCl, 0.5 mM EDTA, pH 7.5)—in samples lacking HPF1, only mChPARP1 was mixed with the same buffer. A stock solution of XRCC1 and LIG3 was also premixed in storage buffer 500 (25 mM Tris, 500 mM NaCl, 0.5 mM EDTA, pH 7.5) at 10× the highest concentration point used in the assay. A stock solution of nNCPs was prepared at 4× concentration (usually 2 μM) in RB Low (10 mM Tris, 150 mM KCl, 1 mM EDTA, pH 7.5). 10 mM NAD⁺ stock solutions were prepared in deionized water and filtered through a 0.22 μm membrane. MgATP, DTT and Tris were also prepared together as a 10× sterile-filtered stock solution with the pH adjusted to 7.5 by addition of aqueous 12 M sodium hydroxide.

For reactions including PARylation, a master mix including every component except XRCC1/LIG3 was prepared. PARylation was initiated by addition of NAD⁺ and allowed to proceed for 20 min at 37 °C. Samples lacking NAD⁺ (i.e., ‘unmodified’ conditions) were also incubated at the same temperature for the sake of consistency. During this period, XRCC1/LIG3 was serially diluted 0.5× in storage buffer 500 across 11 concentration points (including a 12th point containing no XRCC1/LIG3, only buffer) in a 96-well low-protein-binding polypropylene plate. Following the PARylation reaction, the master mix was apportioned in 9 μL volumes into an adjacent row of the 96-well plate. 1 μL of each XRCC1/LIG3 stock solution (at 10× final assay concentration) was transferred simultaneously using a multichannel pipet into the row of samples containing the master mix. Ligation was allowed to proceed for another 20 min at 37 °C. Samples for denaturing gel analysis were quenched by simultaneously transferring 5 μL of each reaction into pre-aliquoted 15 μL portions of loading buffer (1.3× TBE, 2.66 M urea, 8% w/v Ficoll PM400) and mixing vigorously. Each sample was then transferred into a thin-walled PCR tube and heated to 95 °C for 5 min before being rapidly cooled on ice. 10 μL of each sample was loaded onto a TBE-urea 15% polyacrylamide gel pre-equilibrated in 0.5× TBE heated to 70 °C. DNA species were resolved by electrophoresis at a constant voltage (180 V) for 30 min. Products were visualized by AF647 fluorescence originating from the ligated or unligated 31mer segment of n601-DNA using a ChemiDoc MP system.

Ligation assays—including PARG

Ligation assays including PARG were performed identically to the general assay protocol except varying concentrations of PARG were added immediately prior to NAD⁺. In this scenario, 7 μL samples of a master mix including all assay components except for NAD⁺, PARG and XRCC1/LIG3 were added to a 96-well plate. PARG was prepared at 10× the highest assay concentration and serially diluted in storage buffer 500. 1 μL of each PARG dilution was added simultaneously to each sample of master mix followed by 1 μL of 10 mM NAD⁺. One sample contained the maximum PARG concentration (100 nM) with no NAD⁺ (replaced with 1 μL water). The entire plate was sealed and incubated at 37 °C for 20 min. A stock solution containing 150 nM XRCC1/LIG3 was then added (1 μL) simultaneously to each condition. After another 20 min incubation period at 37 °C, samples were resolved by electrophoresis on urea-TBE gels and imaged as described above.

Ligation assays—On “Free” DNA

Assays involving n601-DNA unincorporated into NCPs were performed essentially the same as the general protocol, except the nNCP was substituted with n601-DNA (also including 5 mol% AF647-labelled 31mer) pre-exchanged into RB Low.

Ligation assays—Titration mChPARP1

For assays containing variable concentrations of mChPARP1/HPF1 and no NAD⁺ (Figure S2B), a master mix containing all ligase reaction components except for mChPARP1/HPF1 and XRCC1/LIG3 was prepared and apportioned into 8 μL samples in a 96-well plate. A stock solution of mChPARP1/HPF1 was prepared at 10× the highest concentration point and serially diluted 0.5× in storage

solution 250; the final well contained 0 μ M mChPARP1/HPF1. 1 μ L of each mChPARP1/HPF1 dilution was simultaneously added into the 8 μ L master mix samples. Following a 20 min incubation period at 37 °C, 1 μ L of a 10 \times XRCC1/LIG3 stock solution (150 nM) was added into every sample. Following another 20 min incubation period at 37 °C, the reactions were quenched and resolved by electrophoresis as described in the general protocol.

Ligation assays—Comparing PARylated to trypsinized nNCPs

Assays containing trypsinized nNCPs were performed essentially the same as those containing PARylated nNCPs, except mChPARP1 and HPF1 were omitted. Storage buffer 250 was added in their place to keep the salt concentrations between conditions constant. 1 mM NAD⁺ was included in trypsinized nNCP samples even though mChPARP1/HPF1 was absent. XRCC1/LIG3 were titrated to higher concentrations, reaching 1 μ M maximum and descending in increments of 0.33 \times . Ligation reactions and electrophoresis were otherwise performed exactly as described in the general protocol.

Ligation assays—Titration of XRCC1 or LIG3 Δ BRCT

Assays including mutant LIG3 Δ BRCT were performed identically to the general protocol, except full-length LIG3 was swapped for LIG3 Δ BRCT. In reactions containing variable concentrations of XRCC1, LIG3 and XRCC1 were added separately into 8 μ L samples containing all other components (including PARylated nNCPs). XRCC1 was serially diluted in storage buffer 250 from 10 \times the highest concentration point, while LIG3 was prepared at a constant concentration (150 nM; to yield a final concentration of 15 nM in the reaction) in the same buffer. Following PARylation, 1 μ L XRCC1 (variable concentration) was added simultaneously into each sample followed by 1 μ L LIG3 (constant concentration, 150 nM) to initiate ligation.

Micrococcal nuclease sensitivity assays

Micrococcal nuclease (MNase) reactions contained the following: 25 mM Tris, 37.5 mM KCl, 112.5 mM NaCl, 0.5 μ M (n)NCP, 1 μ M mChPARP1, 1.5 μ M HPF1, 0.5 mM MgCl₂, 2.5 mM DTT, 2.5 mM CaCl₂, 1 mM NAD⁺, 100 gel units μ L⁻¹ MNase (units defined by the manufacturer, NEB), pH 7.5. All components except for MNase were combined in a master mix that was incubated for 20 min at 37 °C to induce PARylation. Samples lacking NAD⁺ were incubated in the same way. A 10 \times stock solution of MNase (1000 gel units μ L⁻¹) was prepared by diluting the enzyme (as supplied by the manufacturer) 1:1 with DNase-free water. Following the 20 min incubation, the 10 \times MNase stock solution was diluted 1:10 into each sample. 5 μ L aliquots were withdrawn at specific time intervals following the addition of MNase and quenched in 15 μ L loading buffer. Samples were transferred to thin-walled PCR tubes and incubated at 95 °C in a PCR machine. After rapid cooling on ice, 10 μ L of each sample was loaded onto a TBE-urea 15% polyacrylamide gel. Both the gel and 0.5 \times TBE electrophoresis buffer were pre-heated to 70 °C. DNA species were resolved by applying a constant voltage (180 V) for 30 min. To stain DNA, the gel was incubated with SYBR Gold (diluted 1:10000 in deionized water) for 5 min with constant agitation. Excess dye was removed by several washes with fresh water prior to imaging. DNA species were visualized on a ChemiDoc MP imaging system using the fluorescence specifications for SYBR Gold.

Electrophoretic mobility shift assays

Binding reactions involving nNCPs and mChPARP1 contained the following: 25 mM Tris, 37.5 mM KCl, 112.5 mM NaCl, 0.5 μ M nNCP with 5% AF647-labelled 31mer, varying concentrations of mChPARP1 (7.8–2000 nM), 0.5 mM MgCl₂, 2.5 mM DTT, 1 mM NAD⁺, pH 7.5. Note that HPF1 was excluded to prevent PARylation of the nNCP. A master mix containing all components except mChPARP1 was assembled. mChPARP1 was prepared at 10 \times the highest concentration point used in the experiment. Serial dilution (with 0.5 \times increments) was performed in storage buffer 250 in a 96-well plate. 9 μ L of master mix was transferred into each well of a row in the 96-well plate. 1 μ L of each mChPARP1 serial dilution was added to a sample of the master mix. The plate was incubated at 37 °C for 20 min to induce PARylation in cases where NAD⁺ had been included. 5 μ L of each sample was then transferred to and mixed with 15 μ L of native loading dye (1.33 \times TBE, 8% w/v Ficoll PM400), from which 10 μ L was then loaded onto a native TBE 6% polyacrylamide gel. Electrophoresis was conducted at a constant voltage (80 V) for 75 min at room temperature. Bound species were visualized by AF647 fluorescence on a ChemiDoc MP imaging system.

Nuclear magnetic resonance spectroscopy

Samples

NMR samples were prepared from reconstituted nNCPs buffer-exchanged into NMR buffer (20 mM sodium phosphate, 100 mM NaCl, 0.1 mM EDTA, 3% D₂O, pH 6.0) at typical concentrations between \sim 90 μ M–110 μ M. A pair of NMR samples was prepared, corresponding to PARylated and unmodified particles, with one histone ²H, ¹⁵N-, and ILV-methyl labelled (the others were uniformly ²H-labelled), as described above. In addition to the eight samples prepared in this manner, we also generated samples of PARylated and unmodified NCPs with either H3 or H4 ²H, ¹⁵N-, ILV-methyl labelled (other histones perdeuterated) using a buffer that lacked NaCl (20 mM sodium phosphate, 0.1 mM EDTA, 3% D₂O, pH 6.0).

Assignment of NCP methyl groups

Assignments of ¹H-¹⁵N amide (NCP tail) and ¹H-¹³C methyl correlations for the individual histones in the context of unmodified NCPs were obtained from previous reports^{9,133,134} and could easily be transferred to spectra of the PARylated particles.

NMR experiments

All NMR experiments were recorded at 37 °C (with the exception of the diffusion experiments which were measured at 25 °C) using either 14.1 T or 18.8 T Bruker Avance III HD spectrometers, or with a 23.5 T Bruker Avance NEO spectrometer, each equipped with a

x, y, z gradient TCI cryoprobe. The integrity of each NCP sample was established by recording ^1H - ^{15}N HSQC spectra using a gradient-enhanced HSQC experiment, 37 °C (18.8 T),¹³⁶ focusing on the histone tail regions, or via ^1H - ^{13}C HMQC datasets, 37 °C (23.5 T) with water suppression achieved using a WATERGATE scheme.¹³⁷

Chemical shift perturbations

CSPs (Hz) were calculated with the following equation, $\sqrt{(\Delta\delta_H \times \nu_{o,H})^2 + (\Delta\delta_N \times \nu_{o,N})^2}$ or $\sqrt{(\Delta\delta_H \times \nu_{o,H})^2 + (\Delta\delta_C \times \nu_{o,C})^2}$ for peaks in ^1H - ^{15}N and ^1H - ^{13}C correlation spectra, respectively, where $\Delta\delta_i$ is the shift difference in ppm and $\nu_{o,i}$ is the Larmor frequency of nucleus i (^1H , ^{13}C or ^{15}N) at the magnetic field at which the experiments were conducted. The CSPs of H3, which were measured from data acquired at 23.5 T, were scaled down to be consistent with the CSPs measured from the other histone NMR data recorded at 18.8 T. In the case where multiple peaks for a given site were observed, the peak with the largest intensity was used for calculating CSPs.

Measurement of $J(0)$ values of backbone amides in NCPs

We have made use of a series of experiments that measure the relaxation rates of four ^{15}N - ^1H two spin terms, either in the presence or absence of ^{15}N and ^1H spin-lock fields, as described previously^{138,139} and more recently in the context of studies of NCPs.⁹ These experiments were supplemented by recording ^{15}N [^1H]-heteronuclear NOEs and ^{15}N R_1 relaxation rates, yielding chemical exchange free measures of histone tail backbone mobility. Details can be found in a previous publication.⁹

Measurement of diffusion

Translational diffusion coefficients were measured via a series of 1D ^{13}C -edited ^1H spectra with nine different gradient strengths (from 10% to 100% maximum, where the maximum strength is 45 G cm⁻¹), 25 °C, using a pulse scheme that is similar to a ^{15}N -edited experiment published previously, but with ^{15}N and ^{13}C pulses interchanged.¹⁴⁰ Encoding and decoding of signals was achieved using pairs of bipolar gradient pulses, where each pulse of the pair has a duration of 1 ms, sandwiched between a diffusion delay period of 300 ms duration. Sample concentrations were varied by successive dilution in NMR buffer: 20 mM sodium phosphate, 100 mM NaCl, 0.1 mM EDTA, 3% D₂O, pH 6.0.

Quantification of ADP-ribose

The average number of ADP-ribose units per PAR chain attached to H3 was quantified by recording ^1H 1D excitation sculpting spectra¹⁴¹ of the PARylated-H3 sample treated with PARG and integrating the aromatic region from 8.5–8.1 ppm. Notably, we observed a very broad, low intensity ‘hump’ derived from the DNA bases which was removed from spectra by insertion of a T_2 filter of 100 ms net duration. Comparison of ADP-ribose peak intensities with the corresponding intensities from the control sample of known adenosine 5'-diphosphoribose concentration (also recorded with a T_2 filter of 100 ms), enabled the determination of the concentration of ADP-ribose units associated with H3. The concentration of H3 in the PARylated-H3 sample to which proteinase K was added was ascertained by recording 1D ^{13}C edited spectra. The spectral region extending from 2.7 ppm – 0.5 ppm was integrated and the integral compared with a proteinase K digested H3 standard of known concentration. In this manner the concentrations of ADP-ribose units and H3 were obtained.

Hydrogen-deuterium exchange mass spectrometry

Unmodified and PARylated nNCPs at 2 μM were equilibrated in 20 mM sodium phosphate, 100 mM NaCl, 0.1 mM EDTA, pH 6.0. Hydrogen-deuterium exchange (HDX) was initiated at room temperature (22 ± 1 °C) by a 10-fold dilution into a D₂O-based buffer with an identical composition as the one described above. The pD of the buffer was adjusted to account for the isotope effect on glass electrodes.^{142,143} HDX was allowed to proceed for 0.2, 1, 5, 15, 60, and 180 minutes. The samples were quenched by mixing 1:1 [v:v] with ice-cold 250 mM sodium dihydrogen phosphate, 3 M guanidinium chloride and 3 mM *N*-dodecylphosphocholine¹⁴⁴ for a final pH of 2.5, followed immediately by flash-freezing in liquid N₂.

Proteolytic digestion, sample handling, and liquid chromatography (LC) were performed on an M-Class ACQUITY UPLC system with HDX technology (Waters). The quenched protein samples were rapidly thawed and loaded onto a 50 μL loop of the UPLC system, resulting in a final injection of 5 pmol of nucleosome core particle per sample. Digestion was carried out online using an immobilized Nepenthesin-II protease¹⁴⁵ column (AffiPro, 1 mm \times 20 mm, 16.2 μL) at 15 °C. The resulting peptides were trapped on a 1.7 μm , 2.1 mm \times 5mm ethylene bridged hybrid (BEH) C18 column (Waters) at flowrate of 100 $\mu\text{L min}^{-1}$ for 3 minutes and separated using reversed-phase chromatography at 0 °C on a 1.8 μm , 1 mm \times 50 mm HSS T3 column (Waters). A linear water: acetonitrile gradient at a flowrate of 100 $\mu\text{L min}^{-1}$ was used to separate the trapped peptides over 8 minutes by ramping acetonitrile from 5% to 35%. Both mobile phases were acidified using 0.1% [v/v] LCMS-grade formic acid. Between each run, the protease column and the injection loop were extensively cleaned using a solution containing 1.5 M guanidinium chloride, 4% [v/v] acetonitrile, 0.8% [v/v] formic acid, and 1.5 mM *N*-dodecylphosphocholine to ensure minimal column carry-over.^{144,146}

The LC outflow was directed to a quadrupole time-of-flight (Q-TOF) Synapt G2Si mass spectrometer (Waters) equipped with a standard electrospray ion source operated in positive-ion mode. The instrument was calibrated online via infusion of LeuEnk solution (1+, 556.2771 Th) from the LockSpray exact mass ionization source (Waters) every 20 seconds at a flow rate of 10 $\mu\text{L min}^{-1}$. Peptide mapping was performed in triplicate using drift time-aligned MS^E data-independent acquisition, as described previously.¹⁴⁷ Mass spectra were recorded over the 50 to 2000 Th range with a scan time of 0.4 s. The transfer collision energy was ramped linearly in alternating scans over 20–40 V to induce fragmentation. Ion mobility separation was controlled manually as described previously.¹⁴⁷ The quadrupole transmission profile was set manually to exclude ions smaller than 300 Th. The TOF mass analyzer was operated in resolution mode. All MS^E data were analyzed using PLGS 3.0.3 (Waters). Raw data were processed with low and high intensity thresholds of 200 and 50 counts, respectively, and data were searched against a customized database including only

the histone sequences. Only peptides identified in all replicates with at least 0.11 product ions per amino acid, and 1 consecutive product ion were processed further.¹⁴⁸

For deuterium uptake measurements, the mass spectrometer parameters were set similar to those recommended by Guttman et al.¹⁴⁹ to minimize ion activation and deuterium loss. The level of deuterium uptake, D , at time t is represented as:

$$D(t) = \frac{m_t - m_0}{m_{100} - m_0}$$

where m_t is the measured centroid mass of the peptide of interest at time t , and m_0 and m_{100} correspond to the measured centroid mass for the undeuterated control and the theoretical maximum deuteration, respectively. HDX data analyses were performed using DynamX 3.0 (Waters). A value of ± 0.50 Da, considerably above the average methodological error (± 0.14 Da),¹⁵⁰ was selected as the cutoff to determine significant differences in relative deuterium incorporation measurements, following the approach described by Engen and coworkers.^{151,152}

Cryogenic electron microscopy

Cryo-EM sample preparation and data collection

Holey gold grids with regular arrays of $\sim 2 \mu\text{m}$ holes were nanofabricated in-house as previously described.¹⁵³ Grids were glow-discharged in air for 15 s prior to application of 3 μL of sample. Each sample contained 2 μM nNCP, either unmodified or PARylated, in EM buffer (20 mM Tris-HCl, 100 mM or 5 mM KCl for high- or low-salt conditions, 0.1 mM EDTA, pH 7.5). PARylated samples also contained automodified mChPARP1 and HPF1. Grids were blotted from the gold side using a Leica EM GP2 plunge freezer (Leica Microsystems) for ~ 2 s (0 s in the Leica setting) at 4 °C and $\sim 95\%$ relative humidity prior to plunge freezing in liquid ethane. Samples were imaged with a Titan Krios G3 electron microscope (ThermoFisher Scientific) equipped with a Falcon 4i direct electron detector camera (ThermoFisher Scientific) and operating at 300 keV. Data collection was automated using the EPU software (ThermoFisher Scientific), applying a defocus range of 1.0 μm to 2.0 μm . Movies were acquired with 30 exposure frames at a nominal magnification of 75,000 \times corresponding to a calibrated pixel size of 1.03 Å, using an exposure rate of $\sim 5.7 \text{ e}^- \text{ pixel}^{-1} \text{ s}^{-1}$ and a total exposure of $\sim 40 \text{ e}^- \text{ Å}^{-2}$. 4969, 3533, 7203, and 3311 movies were collected for the high-salt unmodified, high-salt PARylated, low-salt unmodified, and low-salt PARylated conditions, respectively.

Cryo-EM image analysis

Image analysis was conducted using cryoSPARC v.4.¹³² Patch-based alignments and contrast transfer function (CTF) estimation were carried out during automated data collection in cryoSPARC Live. Particle selection was performed using templates generated from projections of a low-pass filtered NCP map, followed by per-particle motion correction and extraction using a 256 \times 256 pixel box. Following extraction, particles from all four datasets (unmodified and PARylated, high and low salt) were combined into a single dataset containing a total of 1,364,323 particle images (Figure S5A). Several measures were taken to allow accurate comparison of local resolution between maps. The combined dataset was cleaned using three consecutive rounds of 2D classification, yielding a reduced dataset of 645,890 high-quality particle images. From here, particle images were separated according to the specimen preparation condition and used for *ab-initio* 3D reconstruction and map refinement, with a single 3D map calculated for each specimen condition without further removal of any particle images. In this way, we attempted to 1) avoid image analysis steps that would inconsistently keep or remove particles from the four datasets and 2) remove junk and low-quality particle images while retaining the relevant heterogeneity from each dataset that would inform on NCP dynamics. The four maps above had different overall resolutions with the unmodified NCP at 5 mM KCl being the worst. To accurately compare local resolution distribution between the four maps, we reduced the number of particles from each of the other three datasets in the final reconstruction and refinement steps such that the computed maps of all four datasets had overall resolutions of 3.8 Å. This overall nominal resolution includes corrections for the effects of masking and was calculated using the loose mask generated in the non-uniform refinement job in cryoSPARC, which includes the entire NCP molecule including the dynamic DNA entry/exit sites (Figure S5A). Local resolution estimations were carried out on the 3.8 Å maps and the output resolutions were used to colour the 3D map in UCSF ChimeraX.¹³¹

Dynamic light scattering and fitting of diffusion data

DLS sample preparation and analysis

DLS autocorrelation functions were measured using a plate reader format Wyatt DynaPro DLS instrument. Briefly, samples were prepared by dilution of concentrated nNCP or trypsinized nNCP stocks (100 μM) in buffer containing 20 mM sodium phosphate, 100 mM NaCl (omitted for some conditions), 1 mM EDTA, pH 7.5. To remove contaminating dust, the experimental buffer was filtered (0.22 μm) and the sample tubes and the DLS plate wells were evacuated with compressed air prior to use. Prior to loading on the DLS plate, samples were centrifuged at 17500 rpm for 15 min to pellet any large aggregates or dust. Each well contained 20 μL of each sample. Autocorrelation functions (averaged from 25 individual transients) were recorded for each sample well at 25 °C. The average autocorrelation functions were numerically fitted using the DYNAMICS software package (Wyatt Technology) to obtain z-averaged diffusion coefficient (D_z) values.

Analysis of diffusion constants derived from NMR experiments

Diffusion constants from NMR experiments were fit to an isodesmic model of NCP association, as previously described.⁹ In this model, NCPs oligomerize into rodlike stacks, with the thermodynamics of association described by the following set of equilibrium equations:

$$K_A = \frac{[N_2]}{[N_1]^2} = \frac{[N_3]}{[N_2][N_1]} = \dots = \frac{[N_i]}{[N_{i-1}][N_1]} = \dots = \frac{[N_n]}{[N_{n-1}][N_1]} \quad (\text{Equation 1})$$

In Equation 1, NCP monomers are denoted as N_1 and add to growing assemblies in each step with an association constant K_A , where n is the final assumed assembly size (i.e., n NCPs in a stack; values of 100, 200, or 300 were used in the analysis with identical results). Concentrations of individual NCP species were obtained by solving the system of equations in [1], as described previously,⁹ during each round of the fitting procedure using the current value of K_A and the total experimental concentration of NCP particles, N_T . Average diffusion constants, $D_{avg.}$, were subsequently calculated using the solved NCP concentrations in each fitting iteration according to:

$$D_{avg.} = \sum_{i=1}^n \frac{i[N_i]}{N_T} D_i \quad (\text{Equation 2})$$

where D_i is the set of diffusion constants for each NCP species at infinite dilution, with each element of the set assumed to obey a scaling law relating the diffusion constant to the number of NCP monomers in the rodlike assembly,⁹ and i takes into account the number of monomers in a given oligomer. This process was iterated until agreement between experimental and calculated diffusion constants at each NCP concentration was obtained.

It is important to note that we have not taken into account the likely possibility that larger particles will contribute less to the NMR signal due to spin relaxation during constant delays in the pulse sequence used. In addition, Equation 2 is strictly only valid in the limit of fast exchange, which in the case of interconversion between a pair of conformers A and B, requires that:

$$k_{ex} \gg \Delta R_1 + \kappa^2 \Delta D \quad (\text{Equation 3})$$

where k_{ex} is the sum of the rates of forward and backward conversion between A and B, $\Delta R_1 = R_{1,B} - R_{1,A}$ is the difference in longitudinal relaxation between the conformers, $\Delta D = D_B - D_A$, with D_i the diffusion constant of the i^{th} species, and $\kappa = \gamma G \delta$, where γ is the proton gyromagnetic ratio, G is the gradient strength, and δ is the duration of the encoding and decoding gradient pulses.¹⁵⁴ Note that in the NCP case, k_{ex} is the sum of the association and dissociation rates for the successive addition/elimination of a particle. Our analysis of the unmodified (i.e., unPARylated) NCP diffusion profile indicates that 70% of the particles are trimers or less (80% of the particles are monomers and dimers in the PARylated case), for which a maximum ΔD of $3.4 \times 10^{-7} \text{ cm}^2 \text{ s}^{-1}$ is calculated. A value of $(\kappa^2 \Delta D)_{\text{max}} < 2 \text{ s}^{-1}$ is obtained for the experimental setup used, and given the relatively low affinities of particles for each other (K_D values of $42 \pm 24 \text{ } \mu\text{M}$ and $185 \pm 98 \text{ } \mu\text{M}$ are fitted for the unmodified and PARylated NCPs, respectively), k_{ex} is expected to be sufficiently large to satisfy Equation 3. Thus, the approximation of the measured diffusion rate as a population-weighted average of diffusion constants of species in solution is a reasonable assumption. It is worth emphasizing that our goal in fitting the data is simply to provide a qualitative measure as to how the relative NCP affinities change with PARylation. It is clear without any analysis of the data that the PARylated sample diffuses more rapidly than the unmodified NCP, despite its increased size, and that the rate of change of diffusion with NCP concentration is less steep, consistent with a decreased tendency to self-associate (as the extracted K_D values from the fits indicate).

Light microscopy

Sample preparation

Samples prepared for microscopy generally contained the following, with slight variations depending on the experiment: 25 mM Tris, 37.5 mM KCl, 112.5 mM NaCl, 0.5 μM nNCP (containing 5 mol% AF647-labelled n601-DNA; also trypsinized in Figure 5E), 1 μM mChPARP1, 1.5 μM HPF1, 1 μM XRCC1/LIG3 (with or without AF488-labelling), 0.1 mM MgATP, 0.5 mM MgCl_2 , 2.5 mM DTT, 1 mM NAD^+ , pH 7.5. ‘Unmodified’ samples did not contain NAD^+ . Prior to combining all components, mChPARP1 and HPF1 were prepared in a 10 \times stock solution with storage buffer 250. XRCC1 and LIG3 were combined in a 10 \times stock solution prepared with storage buffer 500. For samples containing AF488-labelled XRCC1 or LIG3, 10 mol% of the final concentration of either was substituted for AF488-labelled protein (e.g., to give final concentrations of 0.9 μM XRCC1 and 0.1 μM AF488-labelled XRCC1 in the sample to be imaged). To induce PARylation, samples containing all components except for XRCC1/LIG3 were incubated for 30 min at 37 °C prior to image acquisition. XRCC1/LIG3 were added immediately prior to imaging to induce phase separation. 10 μL of each sample were deposited on 35 mm-diameter uncoated no. 1 coverslip glass-bottom dishes (for fluorescence imaging) or into a black polystyrene glass-bottom (140 μm thickness) 96-well plate (for DIC imaging). Samples were observed immediately, although usually a few minutes were required for enough droplets to accumulate on the glass surface to collect consistent images.

For DIC experiments illustrated in Figures 5B, S5A, and S5B, 10 \times stock solutions containing different concentrations of LIG3, XRCC1/LIG3 or XRCC1/LIG3 ΔBRCT were prepared in storage buffer 500. As in the general sample preparation protocol described above, these were added following PARylation.

For samples illustrated in Figure 5F, unnicked, unPARylated NCPs were added to samples following PARylation (i.e., after the 30min incubation period following addition of NAD⁺. Automodified mChPARP1 is incapable of initiating PARylation). A 4× stock solution containing 37 μM unlabelled NCPs and 3 μM AF488-H3 NCPs in RB Low was prepared. All other components were the same as described above, except 75 mM KCl was present instead of 37.5 mM. The NaCl concentration was adjusted to yield a total combined NaCl and KCl concentration of 150 mM, as in the other imaging samples. The final concentrations of unlabelled and AF488-H3 NCPs were 9.7 μM and 0.3 μM, respectively. XRCC1 and LIG3 were left unlabelled.

In samples containing additional DNA repair proteins (i.e., APLF, APTX, PNKP or POLB), each protein was added to the samples along with (phospho-)XRCC1/LIG3 following the 30min PARylation incubation. 10× stock solutions containing 0.5 μM AF488-labelled repair protein along with 4.5 μM of its unlabelled counterpart were prepared in storage buffer 500. The amount of NaCl added to these samples was scaled down to account for the extra storage buffer 500 included with the DNA repair proteins; the final NaCl concentration still totalled 150 mM after all components were combined.

Differential interference contrast imaging

Differential interference contrast (DIC) micrographs were captured on a Zeiss Axio Observer 7 microscope equipped with an AxioCam 702 monochromatic camera and a LD Plan-Neofluar 63×/0.75 NA Corr M27 objective lens. All images were acquired at 25 °C.

Fluorescence confocal imaging

Fluorescence confocal images were collected on a Leica TCS SP8 Lightning/DML8 system containing a Hamamatsu C9100-13 EM-CCD camera. All images were acquired at room temperature with a 63×/1.3 NA glycerol-immersion objective lens at 2042 × 2042 px image resolution, using 488 nm (20 mW), 552 nm (20 mW) and 638 (30 mW) lasers. Laser powers were adjusted to avoid detector oversaturation.

QUANTIFICATION AND STATISTICAL ANALYSIS

Ligation assays

To quantify ligation, gel images were processed in ImageJ.¹⁵⁵ The ‘upper’ and ‘lower’ bands visualized by AF647 fluorescence were assigned as the fully ligated 153 nt and unligated 31 nt fragments of n601-DNA, respectively. Band intensities were measured manually. Background intensity was quantified as the average signal in regions outside of the bands; these values were subtracted from the band intensity values. The fraction of ligated DNA in each condition was calculated from the quotient of ligated band intensity (I_L) to the sum of the ligated and unligated band (I_{UL}) intensities: $\frac{I_L}{I_L + I_{UL}}$. Ligation data, including mean values and standard deviations taken from multiple replicates, were plotted in GraphPad Prism v6.

Partition coefficients derived from fluorescence micrographs

Fluorescence imaging data was processed using Fiji.¹³⁰ Brightness and contrast levels were left unadjusted between samples. Mean fluorescence intensity values were measured in the centres of similarly sized droplets viewed through the AF488 channel. To measure fluorescence intensity outside of droplets, duplicated images were modified with a Gaussian blur filter (5 σ) and manually thresholded to exclude regions inside the droplets. The region of interest defined in this manner was used to measure the mean intensity outside the droplets in the original, unmodified image. Partition coefficients were calculated by dividing the mean intensity inside the droplets with the mean intensity outside the droplets. Results were averaged across multiple droplets from micrographs originating from three independent experiments. The average partition coefficients and their associated standard deviations were plotted in GraphPad Prism v6.

Error analysis of $J(0)$ data

$J(0)$ values were calculated from analysis of spectra from which ¹⁵N[¹H]-heteronuclear NOEs, ¹⁵N R_1 relaxation rates, and the relaxation rates of a series of four ¹⁵N-¹H two-spin terms were obtained. Peak intensities in all datasets were quantified using peakipy (<https://j-brady.github.io/peakipy/>). The resulting errors in intensities were utilized to calculate the errors of heteronuclear NOE values and relaxation rates, with errors in $J(0)$ values then obtained via propagation of these uncertainties. Further details can be found in our previous publication.⁹

Supplemental information

**Poly(ADP-ribosyl)ation enhances nucleosome
dynamics and organizes DNA damage repair
components within biomolecular condensates**

Michael L. Nosella, Tae Hun Kim, Shuya Kate Huang, Robert W. Harkness, Monica Goncalves, Alisia Pan, Maria Tereshchenko, Siavash Vahidi, John L. Rubinstein, Hyun O. Lee, Julie D. Forman-Kay, and Lewis E. Kay

1. Supplementary Figures

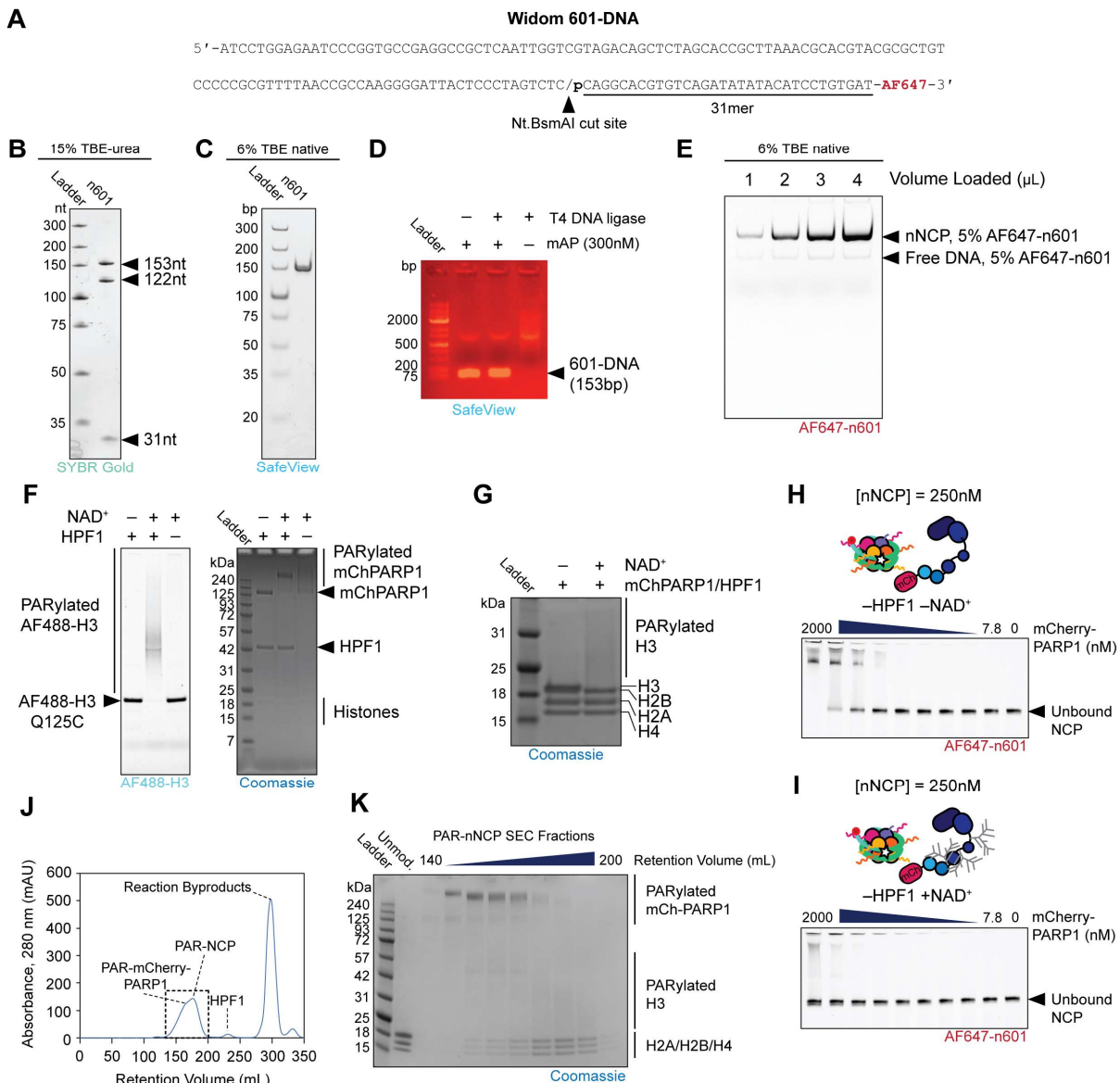


Figure S1. Preparation and modification of nucleosome core particle (NCP) samples; related to Figures 1-5 and STAR Methods. (A) Nucleotide sequence of Widom 601-DNA. The Nt.BsmAI excision site is indicated by a slash (/) within the restriction site: GTCTCN/N, where N is any nucleobase. In the 31nt sequence succeeding the excision site ('31mer'), the location of the 5' phosphate (p) and 3' AlexaFluor 647 label (-AF647) are indicated. (B) Denaturing TBE-urea 15% polyacrylamide gel resolving nicked, mAP-treated 601-DNA. Single-stranded DNA fragments are stained with SYBR Gold. Note the presence of three bands: a 153nt fragment corresponding to the unnicked strand, and 122nt and 31nt fragments corresponding to the nicked strand. (C) Native TBE 6% polyacrylamide gel of nicked, metagenomic alkaline phosphatase (mAP)-treated 601-DNA. A single double-stranded

DNA species corresponding to the full 601-DNA sequence (153nt) is stained with SafeView. (D) 1% agarose-TAE gel depicting products of a T4 ligation reaction including mAP-treated or untreated 601-DNA. Without mAP-treatment, DNA molecules are concatenated by the ligase and migrate as a distribution of high molecular weight species. With mAP-treatment, 601-DNA is impervious to ligation and travels as a single species between the 75bp and 150bp markers. (E) Native TBE 6% polyacrylamide gel depicting various concentrations of 5mol% AF647-labelled nicked 601-DNA-containing NCPs (nNCPs), along with small amounts of residual 'free' DNA. Species are visualized by fluorescence of the AF647 dye adjoined to the 31mer. (F) 4-12% polyacrylamide SDS gel resolving AF488-labelled H3(Q125C)-containing nNCPs PARylated by mChPARP1 in the presence or absence of HPF1. Both panels are the same gel imaged by AF488 fluorescence (*left*) or Coomassie staining (*right*). (G) Coomassie-stained 4-12% polyacrylamide SDS gel showing little change in mobility of H2A, H2B and H4 in the presence (+NAD⁺) or absence (–NAD⁺) of PARylation. Note that unmodified H2B and H3 bands are partially overlapping. (H) Electrophoretic mobility shift assays (EMSAs) involving unPARylated nNCPs and mChPARP1 at different concentrations of mChPARP1, as indicated. Samples are resolved on a native TBE 6% polyacrylamide gel and imaged by AF647 fluorescence of n601-DNA. (I) Same as (H) except mChPARP1 is automodified (20min, 37°C) by adding NAD⁺ prior to electrophoresis. Note that nNCPs are unmodified because HPF1 is absent. (J) Size exclusion chromatogram (SEC) of a nNCP PARylation reaction prepared for NMR and resolved on a HiLoad Superdex 200 26/60 column. Protein and DNA species are detected by UV absorbance at 280nm. (K) Coomassie-stained SDS-polyacrylamide gel resolving SEC fractions corresponding to the hatched box in (J). 'Unmod.' denotes an unmodified nNCP sample for comparison. Note that only three discrete histone bands appear in the modified samples because PARylated H3 migrates as a higher molecular weight smear. Fractions in the range of retention volumes ~150-200mL were typically collected for NMR samples.

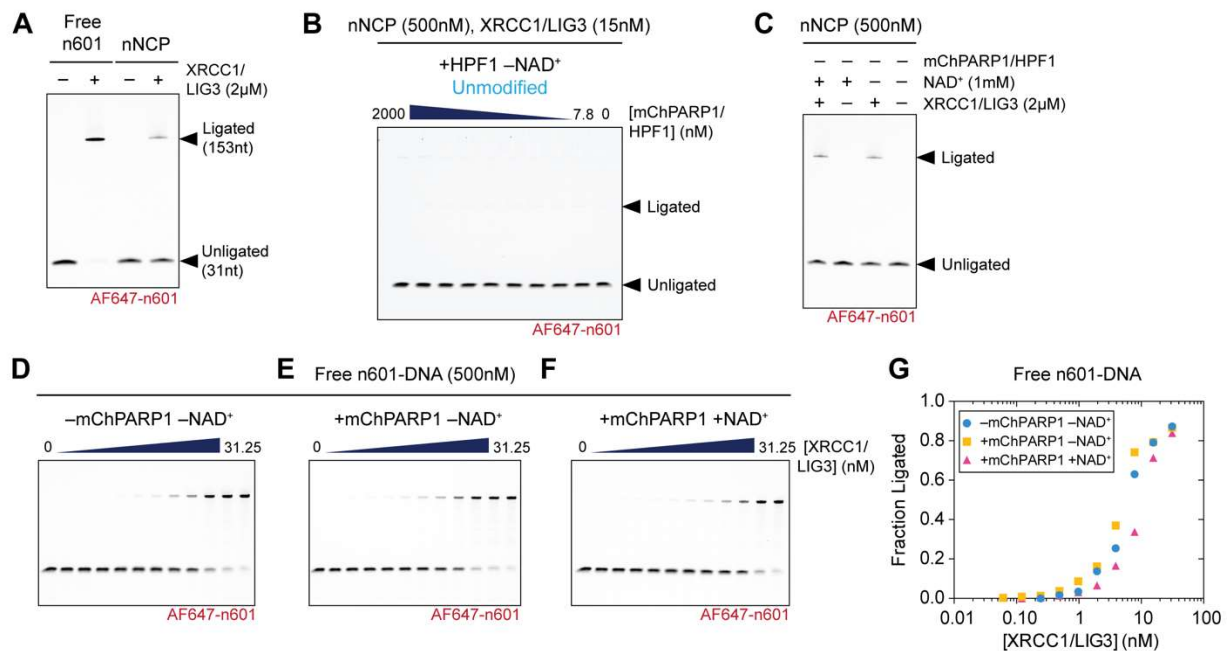


Figure S2. Supplementary ligase and micrococcal nuclease data; related to Figures 1 and 2. (A) Denaturing TBE-urea 15% polyacrylamide gel resolving the products of ligating 5mol% AF647-labelled n601-DNA ('free' n601) or nNCPs (both 500nM) with XRCC1/LIG3 (2μM). Note that at high concentrations of XRCC1/LIG3 (2μM) ligation is observed, while at lower concentrations (31nM) ligation cannot be quantified (Fig. 1C) in the absence of PARylation. (B) Products of ligating 5mol% AF647-labelled nNCPs (500nM) with XRCC1/LIG3 (15nM) in the presence of varying mChPARP1/HPF1 concentrations, but in the absence of NAD⁺. All molecules are unmodified. (C) Ligation of 5mol% AF647-labelled nNCPs (500nM) with XRCC1/LIG3 (2μM) in the presence or absence of NAD⁺ (1mM). mChPARP1/HPF1 was not present. At 2μM XRCC1/LIG3, small amounts of nNCP ligation occur without PARylation. (D) Ligation of 5mol% AF647-labelled n601-DNA (500nM) at various concentrations of XRCC/LIG3 in the absence of mChPARP1/HPF1 and NAD⁺. (E) Same as (D) with mChPARP1/HPF1 (1μM/1.5μM) present. (F) Same as (E) with mChPARP1/HPF1 and NAD⁺ (1mM) present to induce PARylation. (G) Quantification of results in (D-F).

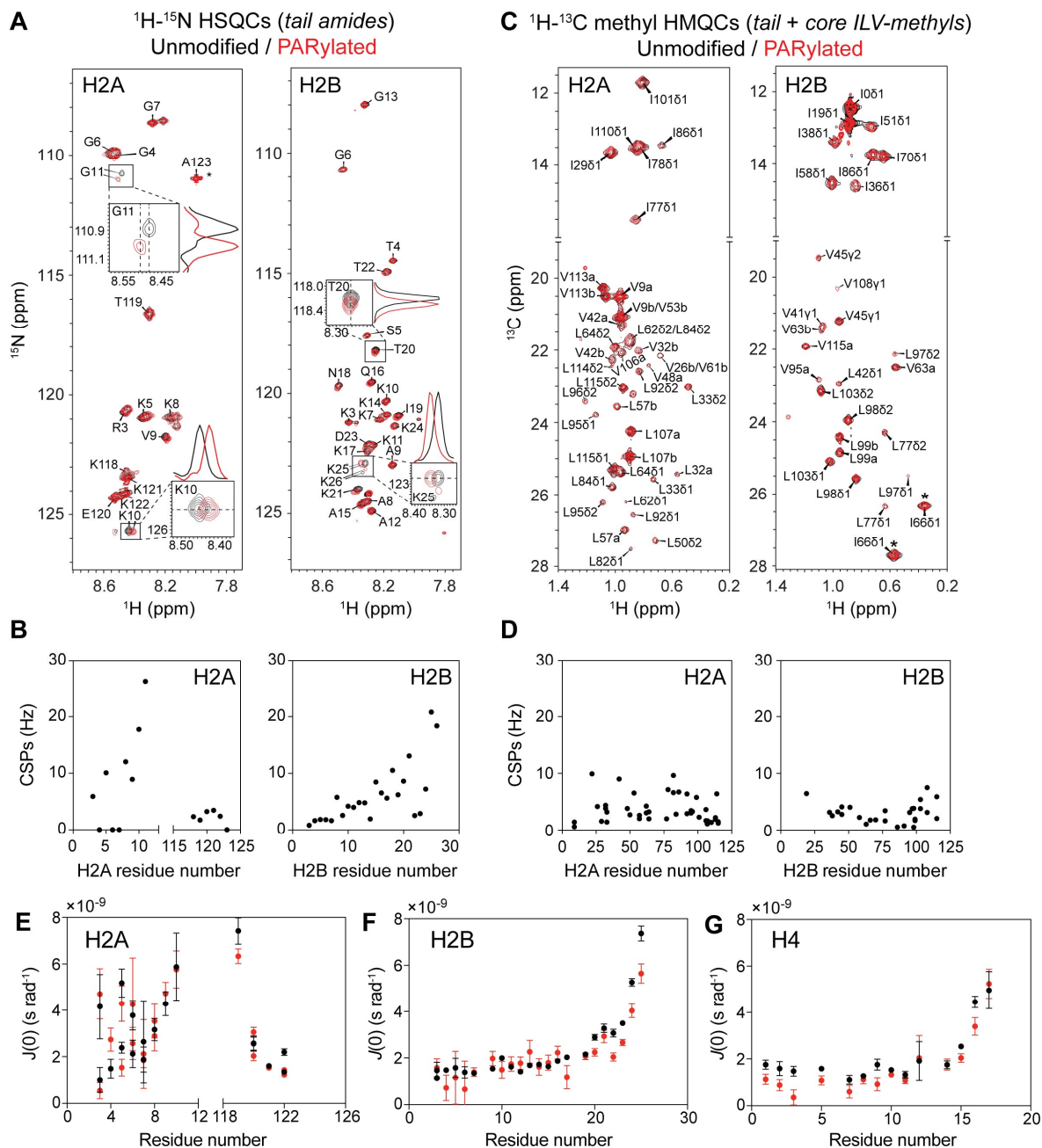


Figure S3. Supplementary NMR data, including H2A and H2B ^1H - ^{15}N and methyl spectra, and H2A, H2B and H4 $J(0)$ data; related to Figure 2. (A) Overlaid ^1H - ^{15}N heteronuclear single quantum coherence (HSQC) spectra of histones H2A and H2B in PARylated (red) and unmodified (black) nNCPs, in 20mM sodium phosphate, 100mM NaCl, 1mM EDTA, pH 6.0, 37°C, 18.8T. *Insets*, notable peak shifts are highlighted. (B) NMR chemical shift perturbations (CSPs) calculated from the spectra in (A). (C) Overlaid ^1H - ^{13}C methyl heteronuclear multiple quantum coherence (HMQC) spectra of histones H2A and H2B in PARylated (red) and unmodified (black) nNCPs, in 20mM sodium phosphate, 100mM NaCl, 1mM EDTA, pH 6.0, 37°C, 23.5T. (D) CSPs

calculated from spectra in (C). (E-G) $J(0)$ values calculated for H2A (E), H2B (F) and H4 (G) in PARylated (*red*) and unmodified (*black*) nNCPs, in 20mM sodium phosphate, 100mM NaCl, 1mM EDTA, pH 6.0.

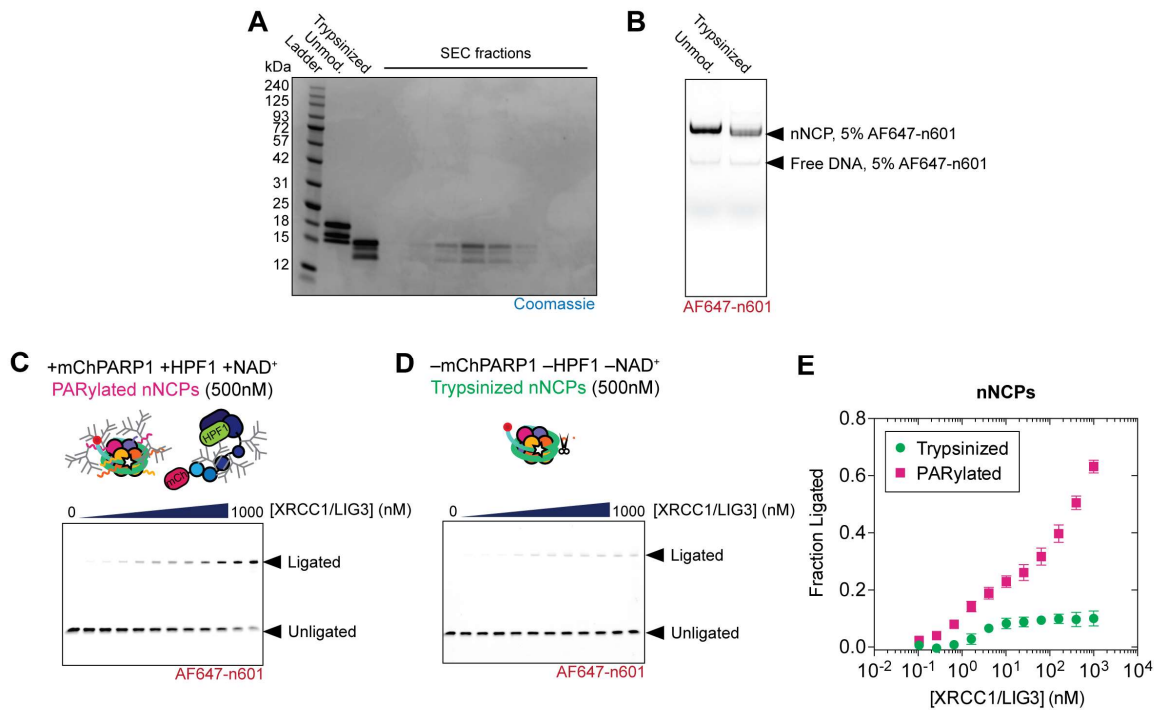


Figure S4. Preparation and ligation of trypsinized nNCPs; related to Figures 2,4 and 5. (A) Coomassie-stained SDS-polyacrylamide gel depicting fractions from size exclusion chromatography (SEC) of a trypsinized nNCP sample. ‘Unmod.’ denotes an untrypsinized sample; note how all four histone migrate more slowly compared to the trypsinized case. Trypsinized histones coelute, suggesting NCPs remain intact following tail removal. (B) Native TBE 6% polyacrylamide gel resolving unmodified (‘unmod.’) and trypsinized nNCPs containing 5mol% AF647-n601 DNA. (C) Ligation of PARylated, 5mol% AF647-labelled nNCPs (500nM) at XRCC1/LIG3 concentrations extending up to 1 μ M. (D) Ligation of trypsinized 5mol% AF647-labelled nNCPs (500nM) at various XRCC1/LIG3 concentrations and in the absence of mChPARP1/HPF1. (E) Quantification of results in (C) and (D) based on three independent replicates. Error bars represent standard deviation of the mean fraction ligated.

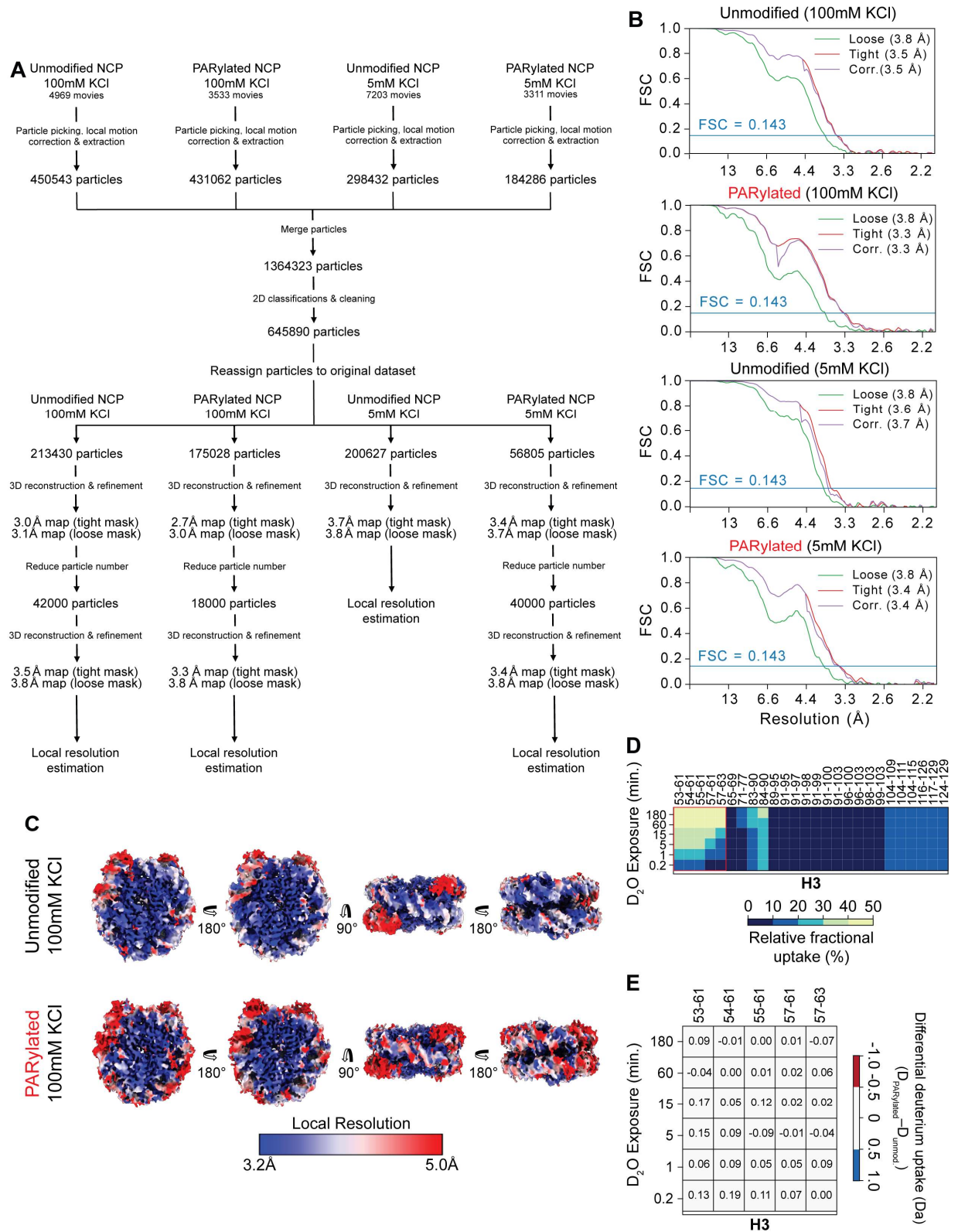


Figure S5. Characterization of DNA dynamics in unmodified and PARylated nNCPs by hydrogen-deuterium exchange mass spectrometry (HDXMS) and cryo-

EM local resolution analysis; related to Figure 3 and STAR Methods. (A) Flowchart summarizing processing and analysis workflow of cryo-EM data for local resolution analysis. Particles picked from datasets acquired from PARylated and unmodified nNCP samples at different KCl concentrations were merged for 2D classification. Following reassignment to the original datasets, particles were further analyzed by 3D reconstruction. In some datasets, the number of particles was limited to yield similar overall resolutions for the 3D density maps. (B) Plots of Fourier Shell Correlation (FSC) versus resolution (Å) for cryo-EM maps of each nNCP condition (unmodified or PARylated, 100mM or 0mM KCl). FSC curves were calculated after applying a loose mask (*green*; the density map thresholded at 50% of its maximum value and dilated 25Å with an additional 15Å cosine falloff), a tight mask (*red*), and the tight mask with the FSC corrected for the effect of masking (*corr.*, *violet*) [S1]. Using the standard CryoSPARC automatic procedure, the tight mask was tightened until FSC(0.143) was equal for the tight mask and the tight mask corrected for the effect of masking. Blue horizontal lines indicate FSC = 0.143. (C) Cryo-EM density maps of PARylated and unmodified nNCPs at 'high' salt: 20mM Tris-HCl, 100mM KCl, 0.1mM EDTA, pH 7.5. Maps are coloured by local resolution and four different views of the same map are shown: shades of blue indicate better resolution, shades of red indicate worse resolution. (D) Heatmap depicting relative fractional uptake values as a function of D₂O exposure time for peptides originating from H3 in unmodified or PARylated nNCPs. The red box highlights the set of peptides indicated in (E). (E) Differential deuterium uptake of select H3 peptides originating from unmodified and PARylated histones. Deuterium uptake for each peptide was calculated as a function of the duration of deuterium exposure, using $D(t) = \frac{m_t - m_0}{m_{100} - m_0}$, where m_t is the measured centroid mass of the peptide of interest at time t , and m_0 and m_{100} correspond to the measured centroid mass for the undeuterated control and the theoretical maximum deuteration, respectively (see Methods).

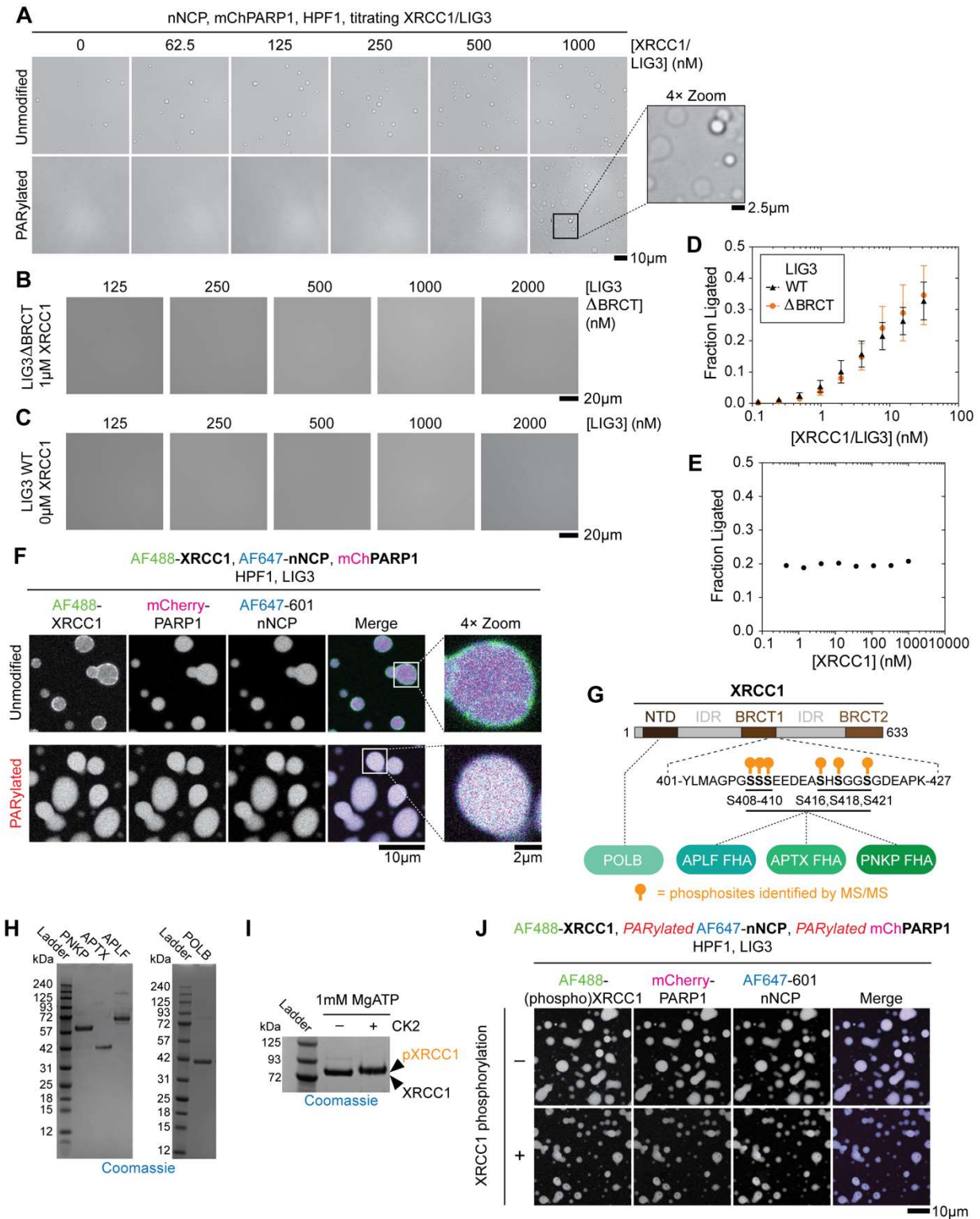


Figure S6. Supplementary condensate data, including effects of condensation on ligase activity and the effects of XRCC1 phosphorylation on condensate morphology; related to Figure 5. (A) Differential interference contrast (DIC)

micrographs of nNCP samples containing mChPARP1/HPF1 (1 μ M/1.5 μ M) and variable concentrations of XRCC1/LIG3, with or without PARylation. Micrographs including PARylation were contrast-adjusted to better highlight features. Scale bar: 10 μ m. (B) DIC micrographs of samples containing PARylated nNCPs (500nM), PARylated mChPARP1 (1 μ M), HPF1 (1.5 μ M), XRCC1 (1 μ M) and various concentrations of LIG3 Δ BRCT. Scale bar: 20 μ m. (C) DIC micrographs of samples containing PARylated nNCPs (500nM), PARylated mChPARP1 (1 μ M), no XRCC1 (0 μ M) and various concentrations of full length LIG3. Scale bar: 20 μ m. (D) Ligation of PARylated, 5mol% AF647-labelled nNCPs (500nM) in the presence of varying concentrations of XRCC1/LIG3 (black, full-length 'WT') and XRCC1/LIG3 Δ BRCT (orange). Error bars represent standard deviation of the mean from three independent replicate experiments. (E) Ligation of PARylated, 5mol% AF647-labelled nNCPs (500nM) in the presence of varying concentrations of XRCC1 and constant LIG3 (15nM). (F) Fluorescence micrographs of samples containing mChPARP1/HPF (1 μ M/1.5 μ M), partially AF488-labelled XRCC1 (1 μ M), LIG3 (1 μ M), with or without NAD⁺ (1mM) to induce PARylation. Scale bar: 10 μ m or 2 μ m (zoomed-in panels). (G) Schematic of the domain structure of XRCC1 and its interactions (hatched black lines) with DNA polymerase beta (POLB) and forkhead associated (FHA) domain-containing proteins, aprataxin- and PNK-like factor (APLF), aprataxin (APTX), and polynucleotide kinase 3'-phosphatase (PNKP). These selections were rationalized by their known interaction properties: APLF, APTX and PNKP bind PAR [S2, 3] and XRCC1 (G408-S421) especially in its CK2-phosphorylated state (see G) [S4, 5]; POLB interacts with the XRCC1 N-terminal domain (NTD) via a dedicated interface that is unaffected by CK2-phosphorylation [S6, 7]. We predicted that these proteins' interactions with PAR and/or phospho-XRCC1 would dictate the extent to which they partition into nNCP condensates. Orange marks represent *in vitro* CK2-phosphorylation sites identified by tandem mass spectrometry. A subset of the *in vitro* phosphorylation sites matched those previously identified in endogenous XRCC1 [S4]. (H) Coomassie-stained SDS-polyacrylamide gels depicting purified, recombinant APLF, APTX, PNKP (*left*) and POLB (*right*). (I) Coomassie-stained SDS-polyacrylamide gel showing diminished migration of XRCC1 following phosphorylation with casein kinase 2 (CK2) and 1mM MgATP. (J) Fluorescence micrographs of samples containing partially AF488-labelled XRCC1 (either unmodified or CK2-phosphorylated, including the dye-labelled fraction; 1 μ M), LIG3 (1 μ M), PARylated mChPARP1/HPF1 (1 μ M/1.5 μ M) and PARylated 5mol% AF647-labelled nNCPs (500nM). CK2-phosphorylation did not change the overall morphological characteristics of the droplets, nor did it affect the localization of AF488-XRCC1, mChPARP1 and AF647-nNCPs in the presence of PARylation. Scale bar: 10 μ m.

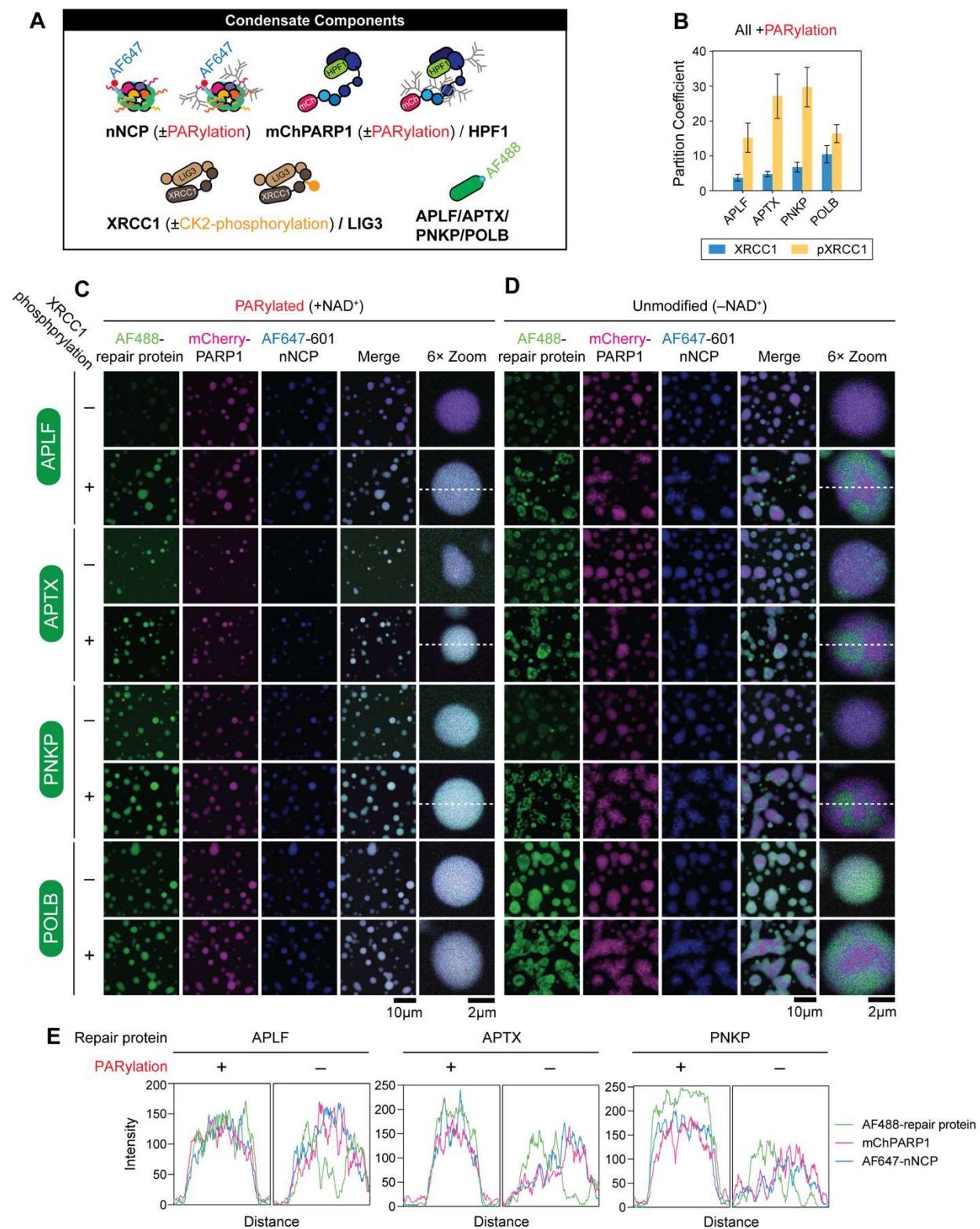


Figure S7. PARylation and XRCC1 phosphorylation regulate enrichment and localization of APLF, APTX, PNKP and POLB in nNCP condensates; related to Figure 5. (A) Graphic illustration of condensate components with potential labelling

schemes and PTMs. (B) Partition coefficients calculated from fluorescence signals measured in PARylated samples containing each indicated AF488-labelled repair protein. Overall, these proteins' partition coefficients correlated with their propensities to interact with XRCC1 in its unmodified or CK2-phosphorylated states. APLF, APTX and PNKP, which all engage in phospho-specific interactions with XRCC1, were especially enriched in condensates containing CK2-phosphorylated XRCC1 and PARylated NCPs, whereas POLB partitioned strongly into condensates containing unmodified or phosphorylated XRCC1, likely because it binds XRCC1 in a phosphorylation-independent manner. pXRCC1: CK2-phosphorylated XRCC1. Error bars represent standard deviation from three independent experiments. (C) Fluorescence micrographs of PARylated nNCP samples containing different, partially AF488-labelled DNA repair proteins. All samples contain XRCC1/LIG3 (1 μ M) and PARylated mChPARP1/HPF1 (1 μ M/1.5 μ M). XRCC1 was unmodified or CK2-phosphorylated in each sample. PARylation promoted homogenous mixing of all components into a single condensed phase. Scale bar: 10 μ m or 2 μ m (zoomed-in panels). (D) Same as (C) except in the absence of PARylation. In the presence of phosphorylated XRCC1, APLF, APTX and PNKP partitioned into condensate subcompartments that were distinct from the mChPARP1- and nNCP-enriched phase, similar to what was observed for AF488-labelled LIG3 and XRCC1 in the absence of PARylation (Fig. 5C,S6F). When both PARylation and XRCC1-phosphorylation were excluded, none of the repair proteins—except for POLB, which interacts with XRCC1 regardless—partitioned strongly into the condensates, likely due to the dual loss of interactions with PAR and XRCC1. Scale bar: 10 μ m or 2 μ m (zoomed-in panels). (E) Plots depicting fluorescence intensities measured along the hatched white lines indicated in the corresponding merged images of APLF, APTX or PNKP-containing droplets in (C) and (D).

2. SI References

- S1. Chen, S., et al. (2013) High-resolution noise substitution to measure overfitting and validate resolution in 3D structure determination by single particle electron cryomicroscopy. *Ultramicroscopy*, 2013. **135**: 24-35. 10.1016/j.ultramic.2013.06.004
- S2. Li, M., et al. (2013) The FHA and BRCT domains recognize ADP-ribosylation during DNA damage response. *Genes Dev*, 2013. **27**(16): 1752-68. 10.1101/gad.226357.113
- S3. Ahel, I., et al. (2008) Poly(ADP-ribose)-binding zinc finger motifs in DNA repair/checkpoint proteins. *Nature*, 2008. **451**(7174): 81-5. 10.1038/nature06420
- S4. Loizou, J.I., et al. (2004) The protein kinase CK2 facilitates repair of chromosomal DNA single-strand breaks. *Cell*, 2004. **117**: 17-28. 10.1016/s0092-8674(04)00206-5
- S5. Caldecott, K.W. (2019) XRCC1 protein; Form and function. *DNA Repair (Amst)*, 2019. **81**: 102664. 10.1016/j.dnarep.2019.102664
- S6. Kubota, Y., et al. (1996) Reconstitution of DNA base excision-repair with purified human proteins: interaction between DNA polymerase beta and the XRCC1 protein. *The EMBO Journal*, 1996. **15**(23): 6662-6670. 10.1002/j.1460-2075.1996.tb01056.x
- S7. Dianova, II, et al. (2004) XRCC1-DNA polymerase beta interaction is required for efficient base excision repair. *Nucleic Acids Res*, 2004. **32**(8): 2550-5. 10.1093/nar/gkh567